UC Irvine

UC Irvine Electronic Theses and Dissertations

Title

Model Selection and Parameter Estimation in Neutrino Cosmology and High Energy Astrophysics Around the Galactic Center

Permalink

https://escholarship.org/uc/item/8368n23p

Author

Canac, Nicolas

Publication Date

2016

Peer reviewed|Thesis/dissertation

UNIVERSITY OF CALIFORNIA,
IRVINE

Model Selection and Parameter Estimation in Neutrino Cosmology and High Energy
Astrophysics Around the Galactic Center

DISSERTATION

submitted in partial satisfaction of the requirements
for the degree of

DOCTOR OF PHILOSOPHY

in Physics

by

Nicolas Canac

Dissertation Committee:
Associate Professor Kevork Abazajian, Chair
Professor Manoj Kaplinghat
Professor Asantha Cooray

2016

DEDICATION

To

my parents Pierre and Virginia

and my sister Vanessa

for their unwavering support, love, and encouragement.

TABLE OF CONTENTS

LIST OF FIGURES

LIST OF TABLES

ACKNOWLEDGMENTS

First and foremost, I would like to thank my committee chair Professor Kevork Abazajian for his guidance and patience. It was only with his direction and tutelage that this dissertation was made possible. I would also like to thank my committee members, Professor Manoj Kaplinghat and Professor Asantha Cooray, and all of the professors who helped me along my academic journey. It is their love and enthusiasm for physics that inspired me to pursue an education in physics and to persevere despite all the times I felt I had no idea what I was doing.

I would also like to acknowledge and thank my collaborators Anna Kwa, Shunsaku Horiuchi, Grigor Aslanyan, Layne Price, and Richard Easther. Their efforts were instrumental in making the work that appears in this thesis a reality.

I want to thank all of my friends who joined me on this academic pilgrimage. In particular, I would like to extend a special thank you to my classmates Chase Shimmin, Mohammad Abdullah, Anthony DiFranzo, Andrew Pace, Oliver Elbert, and Jeff Botimer, who are responsible for some of my fondest memories over these past five years. I will also be forever grateful for the knowledge they imparted on me as we worked together and learned from one another and for keeping me reasonably sane throughout it all.

Of course, I would not be who I am today without my friends and experiences prior to attending the University of California, Irvine. I am especially grateful to Joshua Nguyen, Anh-Viet Tran, and Clayton Huff for helping me become the person I am today, and for motivating me to continue to become a better person every day.

I would like to thank the journals Physical Review D and the Journal of Cosmology and Astroparticle Physics, in which portions of this thesis appear.

Finally, I wish to extend my deepest thanks to my family. To Mom, Dad, and Vanessa, there are no words to accurately describe the level of gratitude I feel for your support and sacrifices all these years. Thank you.

CURRICULUM VITAE

Nicolas Canac

EDUCATION

Doctor of Philosophy in Physics   **2016**
University of California, Irvine   *Irvine, California*

Master of Science in Physics   **2015**
University of California, Irvine   *Irvine, California*

Bachelor of Science in Electrical Engineering   **2010**
University of Texas at Austin   *Austin, Texas*

RESEARCH EXPERIENCE

Graduate Research Assistant   **2011–2016**
University of California, Irvine   *Irvine, California*

TEACHING EXPERIENCE

Teaching Assistant   **2011–2016**
University of California, Irvine   *Irvine, California*

Teaching Associate   **2015**
University of California, Irvine   *Irvine, California*

REFEREED JOURNAL PUBLICATIONS

Astrophysical and Dark Matter Interpretations of Extended Gamma-Ray Emission from the Galactic Center
Physical Review D

2014

Discovery of a New Galactic Center Excess Consistent with Upscattered Starlight
Journal of Cosmology and Astroparticle Physics

2015

MANUSCRIPTS IN PREPARATION

Testing for cosmological evidence of new physics: neutrinos, the primordial power spectrum, and model dependence

2016

Observational Signatures of the Gamma-rays from Bright Blazars as Interpreted from the Wakefield Theory

2016

CONFERENCE AND WORKSHOP TALKS

Analysis of Dark Matter and Astrophysical Interpretations for Excess Extended Gamma-ray Emission in Galactic Center
TeV Particle Astrophysics 2013

Aug 2013

Dark Matter and Astrophysical Interpretations for Excess Extended Gamma Ray Emission in Galactic Center
Fermi Summer School 2014

May 2014

SOFTWARE CONTRIBUTIONS

Cosmo++   `http://cosmo.grigoraslanyan.com/`
An Object-Oriented C++ Library for Cosmology

ABSTRACT OF THE DISSERTATION

Model Selection and Parameter Estimation in Neutrino Cosmology and High Energy
Astrophysics Around the Galactic Center

By

Nicolas Canac

Doctor of Philosophy in Physics

University of California, Irvine, 2016

Associate Professor Kevork Abazajian, Chair

Understanding the particle nature of dark matter and determining the properties of neutrinos remain two of the most important questions within the physics community. Both problems lie within the intersection between astrophysics and particle physics, a fact which gives rise to a rich set of independent and complementary approaches to making progress on both fronts. This thesis presents three works that attempt to construct models and constrain the properties of these particles using empirical data from a large host of astronomical observations. The first work uses observations from the Fermi Gamma-ray Space Telescope's Large Area Telescope (Fermi LAT) to construct empirical models of the diffuse gamma-ray background in the Galactic Center (GC). A new template associated with cosmic rays interacting with molecular gas is detected with high significance. Using this new template along with other known sources of gamma-ray emission in the GC, I find that the previously detected extended gamma-ray excess is still detected for all permutations of the background model, although its properties vary significantly within the observed range of models. The second work presents a detection of a new source of gamma-ray emission in the GC that traces the morphology of infrared starlight, again using observations from the Fermi LAT. I argue that this emission is likely due to the same source of cosmic rays responsible for producing the emission associated with the molecular gas template in the previous work,

and further make the case that this population of cosmic rays could be produced by the same source responsible for the GC excess. The last work explores how derived neutrino parameter constraints depend on the assumed form of the primordial power spectrum, using constraints derived from a host of cosmological data sets, including cosmic microwave background, baryon acoustic oscillation, power spectrum, cluster counts, and hubble constant measurements. I find that for a model independent reconstruction of the primordial power spectrum, neutrino parameter constraints are robust. In addition, certain data sets suggest evidence for non-standard cosmological parameters, though this could also be attributed to systematics within the data.

Chapter 1

Introduction

From as far back as there exist written records, we have evidence that man has wondered about the origin and composition of the universe and the place and purpose that we occupy within it. For much of that time, perhaps guided by little more than our imagination and a yearning for a sense of self-importance, we concocted tales that told of the history of the universe in terms very familiar to what we knew and experienced here on Earth. From a universe born of a cosmic egg, to one made entirely of water, earth, fire, and air, to the Ptolemaic universe—perhaps the most enduring cosmological model in human history— in which the entire universe revolved around a stationary Earth, we have tended to be not especially imaginative in our cosmologies. We even envisioned systems governing the universe, which very much resembled our own systems of government here at home, headed by gods and goddesses, who, naturally, looked exactly like us. But to judge our ancestors as folly for their lack of imagination is perhaps too harsh. How could they have framed their theories of the universe in terms other than what they were familiar with? And how do we know that we are not now victims of the same limitation?

However, we have come a long way since then. As is often said, we stand on the shoulders of

giants who came before us. The incremental accumulation of thousands of years of human knowledge has led to the development of the scientific method, and with it the invention of technology, opening up new avenues through which we can come to know the universe. That knowledge has enabled us to traverse the Earth in mere hours, communicate at the speed of light, access the entirety of recorded human thought with the push of a few buttons, and look back, in both space and time, to explore the far corners of the universe. There is much we now know that our ancestors could not have ever dreamt of, but there is still much we do not know.

We have discovered that the matter of which we and the things we are familiar with are made constitutes only a very small fraction of the total matter in the universe. A detailed understanding of the rest of the matter—dark matter—continues to elude our best efforts. Perhaps even more troubling than that is the fact that the total energy density of the universe is dominated by a component we have come to call dark energy, out of which "the worst prediction in the history of theoretical physics" arose.[1] It wasn't until the end of the 20th century that we discovered via neutrino oscillation experiments that neutrinos, long thought to be massless, do indeed have mass [60]. However, obtaining a precise determination of their masses continues to remain an outstanding problem in physics. But perhaps the most worrisome issue of all is that the two greatest triumphs in physics that emerged from the 20th century, the theories of general relativity and quantum mechanics, are mutually incompatible with one another. The path forward has perhaps never been more unclear, and yet there is much to feel optimistic about.

It has been said that we are currently living in the golden age of cosmology. Historically a data starved science, cosmology has been one of the main benefactors from an explosion of ground and space-based instruments that are now providing physicists with unprecedented amounts of data, leading to some of the most extraordinarily precise measurements in the

---

[1]The measured cosmological constant is smaller than the value for the vacuum energy density predicted from quantum field theory by a factor of about 10^{120}.

history of human civilization. One could reasonably argue however that this golden age is not confined merely to cosmology, but extends far beyond to the fields of astronomy, astrophysics, and particle physics, among others. Perhaps one of the most exciting revelations has to do with the convergence of goals between astrophysicists, cosmologists, and particle physicists. Questions about the nature of dark matter or the mass of the neutrinos are being probed at the smallest of scales, many times smaller than an atomic nucleus, at instruments such as the Large Hadron Collider all the way up to the largest of scales, on the order of the the entire universe, using measurements of the Cosmic Microwave Background from the Planck satellite.

This convergence of objectives gives rise to exciting period of time in which physicists from historically disjoint fields are engaging in a massive collaborative effort to further human understanding of fundamental physics. However, with this explosion of data and manpower arise myriad new challenges. What is the best way to leverage this data and effort in order to gain meaningful insight into fundamental questions and search for hints of new physics? How do we avoid biasing our conclusions? How do the assumptions we make about our data and about our models influence our results? It is the goal of this thesis and one of the main overarching themes therein to explore these questions within the context of astroparticle physics and neutrino cosmology, as I seek to contribute to our understanding of dark matter and examine the problem of constraining neutrino masses using astronomical and cosmological data sets.

Of the three main strategies for attempting to detect dark matter, this thesis will focus on indirect detection, whereby two dark matter particles annihilate, producing a shower of standard model particles. Most notably for detection efforts are gamma-rays, which trace their source distribution by virtue of being uncharged. The Galactic Center provides a natural place to look for signals of this type as it is expected to contain a high density of dark matter, with a density profile that increases as a power-law toward the center [111]. A popular

candidate for the dark matter is a weakly interacting massive particle (WIMP), thermally produced in the early universe until freeze-out, thus establishing the expected annihilation rate today [56]. A number of groups have detected a source of extended gamma-ray emission in the direction of the Galactic Center which is consistent with the expectations for a dark matter signal in terms of spatial morphology, flux, and spectrum [66, 72, 74, 37, 10, 68, 89]. In this thesis, I will explore this previously detected signal, seeking to further characterize its properties and systematic uncertainties.

Neutrinos are second only to photons in cosmological number density among known particles, and thus can alter cosmological observables in spite of their rather diminutive nature. Cosmological observations offer a potentially stringent means of constraining the total mass of neutrinos. Large scale structure in particular is especially sensitive to neutrino mass, as massive neutrinos would produce a strong suppression in the clustering of galaxies due to neutrino free streaming. The cosmic microwave background is also sensitive to neutrino mass and effective neutrino number, although it is perhaps more important for its complementary role in removing degeneracies between standard cosmological parameters and neutrino parameters. Measurements of the cosmic microwave background from Planck have determined the standard cosmological parameters to the percent level. However, as cosmological neutrino mass constraints approach the lower bound of $\Sigma m_\nu \approx$ 60 meV required by oscillation experiments, a detailed analysis of the robustness of cosmological limits on neutrino parameters becomes essential. Specifically, modifications to the assumed form of the primordial power spectrum (PPS), motivated by non-standard inflationary models, could mimic the effect of massive neutrinos and affect the derived constraints on neutrino properties. Studying this dependence will be another one of the main goals of this thesis.

Here I focus primarily on three works. The first two, which comprise chapters 2 and 3, center around the search for signals consistent with those expected from annihilating dark matter in the Galactic Center (GC). In particular, I aim to further investigate the previous

detection of an extended gamma-ray excess in the direction of the GC. In chapter 2, I examine how systematic uncertainties related to modeling of the gamma-ray background in the GC impact the properties of the GC excess (GCE). I then discuss how this affects potential dark matter and astrophysical interpretations of the origin of the signal. Chapter 3 builds upon this investigation, detecting a new source of extended gamma-ray emission consistent with inverse Compton emission from a population of high-energy electron-positron pairs. I argue that this same population of electron-positron pairs is likely to produce previously detected emissions via Bremsstrahlung and could originate from the same source that gives rise to the GCE, thus providing a single framework to explain all three extended emissions in the GC. Chapter 4 continues with the common theme of examining how prior assumptions within a model can impact the properties of the parameters we wish to study. In particular, we study how neutrino parameter constraints vary when typical assumptions regarding the form of the primordial power spectrum (PPS) are relaxed. We also search for hints of new physics in the form of non-standard neutrino parameters or a non-trivial PPS using Bayesian model selection. Finally, I summarize my conclusions and leave some final remarks in chapter 5.

Chapter 2

Astrophysical and dark matter interpretations of extended gamma-ray emission from the Galactic Center

KEVORK N. ABAZAJIAN, NICOLAS CANAC, SHUNSAKU HORIUCHI, AND MANOJ KAPLINGHAT

Chapter Abstract

We construct empirical models of the diffuse gamma-ray background toward the Galactic Center. Including all known point sources and a template of emission associated with interactions of cosmic rays with molecular gas, we show that the extended emission observed previously in the Fermi Large Area Telescope data toward the Galactic Center is detected at high significance for all permutations of the diffuse model components. However, we find

that the fluxes and spectra of the sources in our model change significantly depending on the background model. In particular, the spectrum of the central Sgr A* source is less steep than in previous works and the recovered spectrum of the extended emission has large systematic uncertainties, especially at lower energies. If the extended emission is interpreted to be due to dark matter annihilation, we find annihilation into pure b-quark and τ-lepton channels to be statistically equivalent goodness of fits. In the case of the pure b-quark channel, we find a dark matter mass of $39.4 \left(^{+3.7}_{-2.9} \text{ stat.} \right) (\pm 7.9 \text{ sys.})$ GeV, while a pure $\tau^+\tau^-$-channel case has an estimated dark matter mass of $9.43 \left(^{+0.63}_{-0.52} \text{ stat.} \right) (\pm 1.2 \text{ sys.})$ GeV. Alternatively, if the extended emission is interpreted to be astrophysical in origin such as due to unresolved millisecond pulsars, we obtain strong bounds on dark matter annihilation, although systematic uncertainties due to the dependence on the background models are significant.

2.1   Introduction

The Milky Way's Galactic Center (GC) harbors an extremely dense astrophysical environment, with thousands of high-energy sources detected in the X-ray within the inner $0.3°$ [90], as well as numerous gamma-ray emitting point sources [93]. In addition, the GC is expected to harbor high densities of dark matter (DM) with a power-law increase in density toward the center, leading it to be among the best places in which to find signals of DM particle annihilation or decay [111]. A leading candidate for cosmological dark matter is a thermally produced weakly interacting massive particle (WIMP) that can arise in many extensions of the Standard Model of particle physics, whose annihilation is related to their production in the early Universe [56].

Several groups have found strong evidence for extended emission in the gamma ray from the GC using data from the Large Area Telescope (LAT) aboard the *Fermi Gamma-ray Space Telescope.* It has been shown that the extended emission is consistent with the spatial profile

expected in DM halo formation simulations, the flux is consistent with the annihilation rate of thermally produced WIMP DM, and the spectrum is consistent with the gamma rays produced in the annihilation of $\sim 10 - 30$ GeV DM to quarks or leptons [66, 72, 74, 37, 10, 68, 89]. This triple consistency of the gamma-ray extended-source signal in the GC with the WIMP paradigm has generated significant interest. In addition, there are claims of signals consistent with the DM origin interpretation in the "inner Galaxy" [75], and in unassociated point sources [30]. The required dark matter mass and annihilation cross section is consistent with the constraints from Milky Way dwarf galaxies [13].

Alternatively, the high density of compact objects, cosmic-ray emission, and other astrophysical activity in the GC is also expected to be a considerable source of gamma-ray emission. The massive GC Central Stellar Cluster may harbor a significant millisecond pulsar (MSP) population that can have similar gamma-ray flux and spectrum as the observed extended source in the GC [4]. There is also a significant detection of gamma-ray emission associated with molecular gas as mapped by the 20 cm radio map toward the GC [121]. In Ref. [121], the 20 cm map had the strongest statistical detection of the diffuse source templates studied, and is interpreted as bremsstrahlung emission of high-energy electrons interacting with the molecular gas (MG). In addition, the gamma-ray point source associated with Sgr A* is among the brightest sources in the gamma-ray sky. Sgr A*'s spectrum from low- to high-energy gamma rays has been modeled to originate from cosmic-ray protons transitioning from diffusive propagation at low energies to rectilinear propagation at high energies [45, 87]. Interestingly, the potential confusion between pion decay, pulsar spectra and DM annihilation was studied well before the launch of the Fermi LAT [24].

In this chapter, we perform a detailed analysis of the nature of the extended gamma-ray source from the GC region, which we designate as the GC extended (GCE) source, the point sources in the GC, as well as the diffuse emission associated with the 20 cm MG map. We focus on a region of interest (ROI) of $7° \times 7°$ centered at the GC. Since there have been
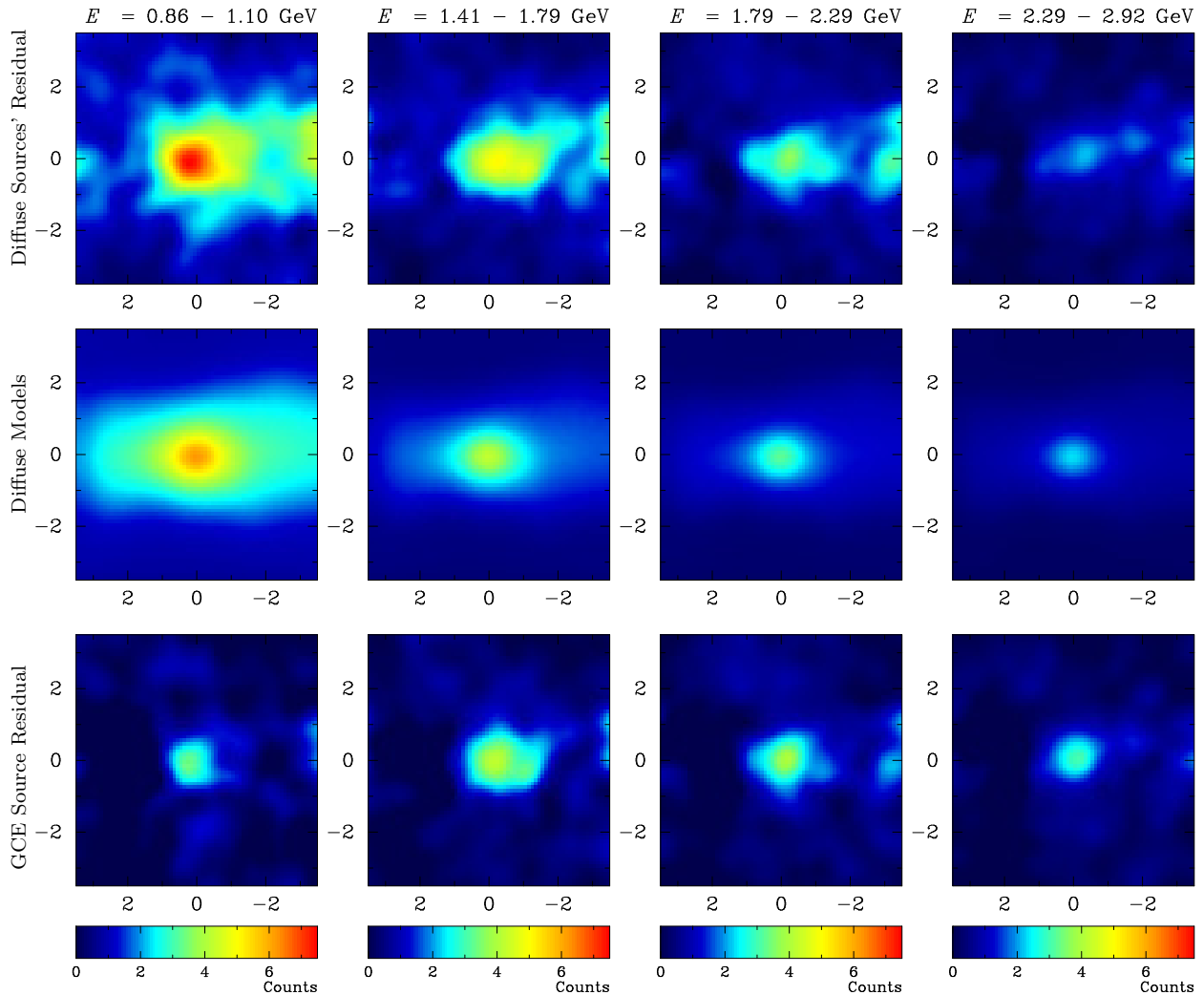
Figure 2.1: For the full model, 2FGL+2PS+I+MG+ND+GCE (see text and Table 2.1), we show here the multicomponent diffuse model (the combined I+MG+ND) residuals, i.e., the counts subtracting all model components other than the I+MG+ND components (top row), the model for the multicomponent diffuse component, I+MG+ND, (middle row), and the GCE source residuals within our ROI (bottom row), at $|b| < 3.5°$ (vertical axis) and $|\ell| < 3.5°$ (horizontal axis). The maps are shown on the same color scale to show the components' relative strength for the counts per pixel, Gaussian filtered spatially with $\sigma = 0.3°$.

detections of all of these sources independently and their spatial information overlaps, we perform a new analysis which consistently includes all of these sources—extended, point-like, and diffuse—as well as their uncertainties determined by the data. In addition, including systematic and statistical uncertainties, we determine the best fit particle masses and annihilation channels if the GCE is interpreted as DM. Conversely, in the case of interpreting

9

the GCE source as an MSP population, we discuss the number of MSPs required within our ROI and we also place strong limits on DM annihilation cross sections.

2.2 Method

We use Fermi Tools version `v9r31p1` to study Fermi LAT data from August 2008 to May 2013 (approximately 57 months of data). We use Pass 7 rather than Pass 7 Reprocessed instrument response functions since the latter have strong caveats for use with new extended sources. We include point sources from the 2FGL catalog [93] in our ROI, $7° \times 7°$ around the GC centered at $b = 0, \ell = 0$. Our procedure is similar to those described in Ref. [10]: we do two separate analyses one from 200 MeV to 300 GeV and the other including only photons with energies between 700 MeV to 7 GeV to focus in on the energy window where the new signal is found. We will use "E7" to label this analysis with photons in the 0.7 to 7 GeV range. For the $0.2 - 300$ GeV analysis, we use the `SOURCE`-class photons binned in an Aitoff projection into pixels of $0.1° \times 0.1°$ and into 30 logarthmically spaced energy bins. `SOURCE`-class events were chosen in order to maximize the effective area while at the same time keeping the cosmic-ray background contamination to below the recommended rate needed to ensure little effect on the detection and characterization of point sources and low latitude diffuse sources, as recommended by the Fermi Collaboration analysis documentation.

We choose the high-energy upper limit for this analysis to probe limits on massive ($\sim$1 TeV) dark matter (see Sec. 2.3.3). For the $0.7 - 7$ GeV analysis we use the `ULTRACLEAN`-class photons binned into pixels of $0.2° \times 0.2°$ and into 12 logarthmically spaced energy bins. In this section we describe the components of our fits.
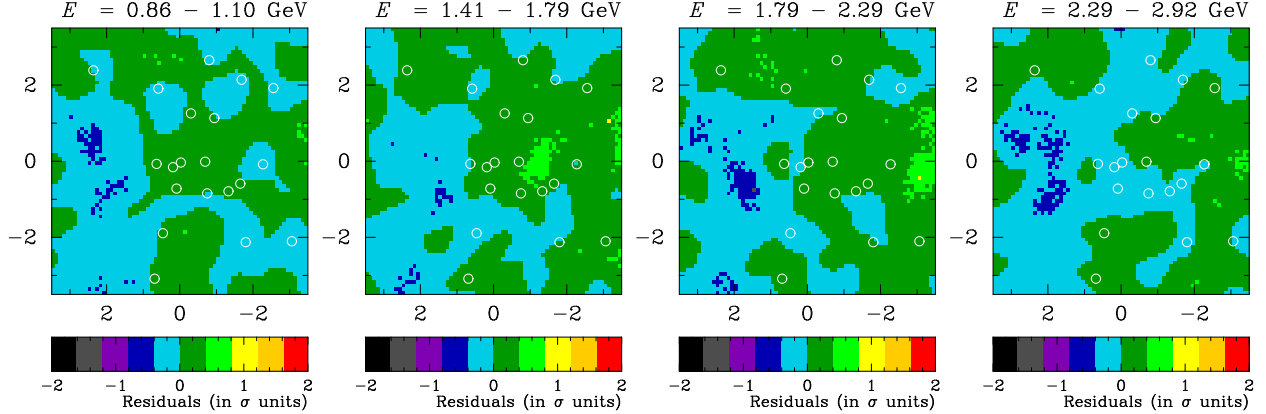
Figure 2.2: For the full model, 2FGL+2PS+I+MG+ND+GCE (see text and Table 2.1), we show the full model residuals after including all diffuse components, in units of σ. Here, $|b| < 3.5°$ (vertical axis) and $|\ell| < 3.5°$ (horizontal axis). The residual count map was Gaussian filtered spatially with $\sigma = 0.3°$. The 20 point sources modeled simultaneously with the diffuse and extended sources in the ROI are shown as circles.

2.2.1 Fit components

The most minimal fitted model is based solely on the 2FGL point sources, in addition to the recommended diffuse emission models associated with the Galactic emission (`gal_2yearp7v6_v0`) and the isotropic background emission (`iso_p7v6source`) which includes contributions from both an extragalactic component and an isotropic diffuse component.

Because the Galactic diffuse background is the dominant component in the ROI, errors in the assumptions used to derive the model could potentially have a large effect on the characterization of sources in this region, and uncertainties associated with this component should account for the largest source of systematic error. Here, we briefly describe the major components that went into this model and how they were derived. In short, the Galactic diffuse model was developed using gas column-density maps as templates for π_0 decay and bremsstrahlung emission, a model for the inverse Compton (IC) emission calculated using GALPROP, and an intensity map for emission not traced by the gas or IC model. These components were then fitted to observations taken by the LAT in order to determine the emissivities and normalization factors. Additionally, we note that an updated model for Pass

11

7 reprocessed data was released, but the Fermi Collaboration does not recommend using this model to study gamma-ray sources in the GC due to the inclusion of additional empirically fitted sources at scales with extension more than 2 degrees.

Beyond the 2FGL point sources, we include two new point sources that were detected with $\text{TS} = 2\Delta \ln(\mathscr{L}) > 25$, originally found to be significant in Ref. [121]. One is from the 1FGL catalog 1FGL J1744.0-2931c, and the other is designated "bkgA." We refer to the combined 2FGL and two additional point source model as 2FGL+2PS.

We next consider a source corresponding to emission from MG. For its spatial template, we use the Green Bank Telescope 20 cm radio map as used in Ref. [121], originally from Ref. [83]. The 20 cm template was originally adopted to explain the GCE as nonthermal bremsstrahlung emission from cosmic-ray electrons interacting with MG particles. The inclusion of the 20 cm map is warranted due to the presence of significant features that do not appear in the Fermi Galactic diffuse model. This is shown clearly in Fig. 4a from Ref. [121], which shows a residual count map after subtracting the diffuse and isotropic templates, leaving a structure that closely traces the ridge. Consequently, the MG template allows us to better account for the gamma-ray emission due to high-energy processes than would be possible with the Galactic diffuse template alone.

For the GCE source we adopt a spatial map that corresponds to a DM density-squared template as described in Sec. 2.2.2. As shown below, the DM density's inner profile is dominated by a power law increasing as $\propto r^\gamma$. When interpreted as MSP, the real-space density corresponds to $n_{\text{MSP}} \propto \rho^{2\gamma}$.

We also test the potential presence of a diffuse (or extended) source associated with the same density profile of the Central Stellar Cluster of the Milky Way. To do this, we test the significance of a source with spatial profile $n_{\text{Dif}} \propto \theta^{-\Gamma}$, where θ is the angular separation from the GC ($b = 0, \ell = 0$). We designate this new diffuse source as ND below, and we allow

Γ to vary from -1.3 to $+0.8$ when performing fits, which allows for a radially decreasing (positive Γ) and increasing (negative Γ) new diffuse component.

We find that the fitted normalization of the isotropic background emission, `iso_p7v6source`, is significantly higher than unity for all model cases. Therefore, we perform fits with the isotropic background emission model `iso_p7v6source` fixed to unity but with an added new isotropic component (denoted "I" in the model names) over the ROI with a free power-law spectrum. The reason we fix the isotropic background model is because it is meant to account for extragalactic diffuse gamma rays and misclassified cosmic rays, and so should not depend strongly on the chosen ROI. We emphasize that all other parameters for model components within the ROI, including diffuse and point sources, were varied during the fitting procedure.

We refer to the new isotropic diffuse model, I, together with the new MG and the ND components, as the "multicomponent diffuse model". In the top row of Fig. 2.1 we show the residual for the new diffuse models, i.e., the raw counts minus a model that includes all components except the multicomponent diffuse model. With inclusion of all components, no significant major residuals are found, as shown in Fig. 2.2. One region of negative residual is seen at $b = -1°$, $\ell = +2°$ that is associated with a feature at that position in the `gal_2yearp7v6_v0` Galactic diffuse model.

The combination 2FGL+2PS+I+MG+ND+GCE defines our *full model* (bottom row of Table 2.1). When fitted, the new isotropic diffuse component (I) is found with high statistical significance with a flux that is 1.4 times that of the two-year Fermi isotropic background model `iso_p7v6source` within our ROI. The spectrum is similar to that of `iso_p7v6source` with a power law index of 1.980 ± 0.082. For the E7 (0.7 to 7 GeV) analysis we did not include a new power-law isotropic source but instead let the normalization of `iso_p7v6clean` vary since the two are so similar to each other.

In addition to these sources, we also ran the Fermi tool `gttsmap` with a coarse binning of

0.4°. Given the high counts with the ROI we expected to pick up a lot of structure so we restricted our search to within the inner $4° \times 4°$. The map of TS values does indeed have many pixels with TS > 25 but most of them are likely not point sources. We picked the pixels with TS > 45 and added them as point sources to the E7-2FGL+2PS+MG+GCE. The fit constrained six of these putative point sources and the total fit improved by $\Delta \ln \mathscr{L} = 110$ due to the addition of these point sources. We urge caution in interpreting these six new sources as bona fide point sources since that requires a more detailed analysis with finer binning. Our main aim here is to construct an empirical model of the emission and adding these sources definitely helps. We have not added these sources to the > 200 MeV analysis since they were found in the more restricted energy window. There were also no significant changes to the GCE spectrum with the addition of these sources. We will refer to these sources (added as point sources) as nPS.

Since the GC region is bright, we have redone the analysis and modeling using only Fermi LAT front-converting photons (`P7SOURCE_V6::FRONT`), and find very similar results to the full data set. The TS of the GCE source goes from 170.7 for the full data to 156.7 with `FRONT` converting data alone, and the other diffuse and point sources are not significantly affected. The normalization and spectrum of the GCE source does change, with the full data set giving the GCE a flux of $(3.1 \pm 0.3) \times 10^{-7}$ ph cm^{-2} s^{-1} and log-parabola parameters of $\alpha = -4.28 \pm 0.18$, and $\beta = 0.959 \pm 0.026$, while the `FRONT` data set gives the softer spectrum $\alpha = -1.15 \pm 0.10$, and $\beta = 0.507 \pm 0.017$ with a higher flux of $(7.1 \pm 0.8) \times 10^{-7}$ ph cm^{-2} s^{-1}, mostly attributable to more low-energy photons in the softer spectrum. We show the `FRONT` converting photon residual GCE spectrum in Fig. 2.4. The systematic shift for the `FRONT` analysis is indicative of the systematic uncertainty in determining the GCE spectrum which is strongly degenerate with the other diffuse and point sources, and which also depends on the assumed spectrum (Fig. 2.10) and the nature of the MG model (Fig. 2.4).

Several point sources as well as the diffuse and extended sources associated with the MG

Table 2.1: Models' renormalized log likelihood values, as reported by the Fermi Science Tools, $-\ln[\mathscr{L} \times (\sum_i k_i!)]$, where k_i is the photon count in bin i, for the various models and the $\Delta \ln(\mathscr{L})$ as compared to the 2FGL-only model for the analysis where photons in the energy range 0.2 to 300 GeV were included. The model in the last row, 2FGL+2PS+I+MG+ND+GCE, defines our full model.

Model	$-\ln[\mathscr{L} \times (\sum_i k_i!)]$	$\Delta \ln \mathscr{L}$
2FGL[1]	-1080408.3	–
2FGL+2PS[2]	-1080510.3	102.0
2FGL+2PS+I[3]	-1080685.7	277.4
2FGL+2PS+I+MG[4]	-1080931.1	522.8
2FGL+2PS+I+MG+ND[5] $\Gamma = -0.5$	-1081012.9	604.7
2FGL+2PS+I+MG+GCE[6] $\gamma = 1.1$	-1081061.5	653.2
2FGL+2PS+I+MG+GCE $\gamma = 1.1$		
$\quad$ + ND $\Gamma = -0.5$	-1081098.3	690.0

and GCE source emission are fit with "log-parabola" spectra of the form

$$\frac{dN}{dE} = N_0 \left(\frac{E}{E_b} \right)^{-(\alpha + \beta \ln(E/E_b))}, \tag{2.1}$$

keeping E_b fixed, yet source dependent, and fitting the other parameters α, β, and N_0.

2.2.2 Dark matter models

For the GCE source, we employ spatial templates derived from "$\alpha\beta\gamma$" profiles fashioned after the Navarro-Frenk-White (NFW) profiles [91, 80],

$$\rho(r) = \frac{\rho_s}{(r/r_s)^\gamma \left(1 + (r/r_s)^\alpha\right)^{(\beta-\gamma)/\alpha}} \tag{2.2}$$

with fixed halo parameters $\alpha = 1$, $\beta = 3$, $r_s = 23.1$ kpc, and a varied γ inner profile. The canonical NFW profile has $\gamma \equiv 1$. Note, the parameters α and β here are never varied.

The differential flux for a dark matter candidate with cross section $\langle \sigma_A v \rangle$ toward Galactic
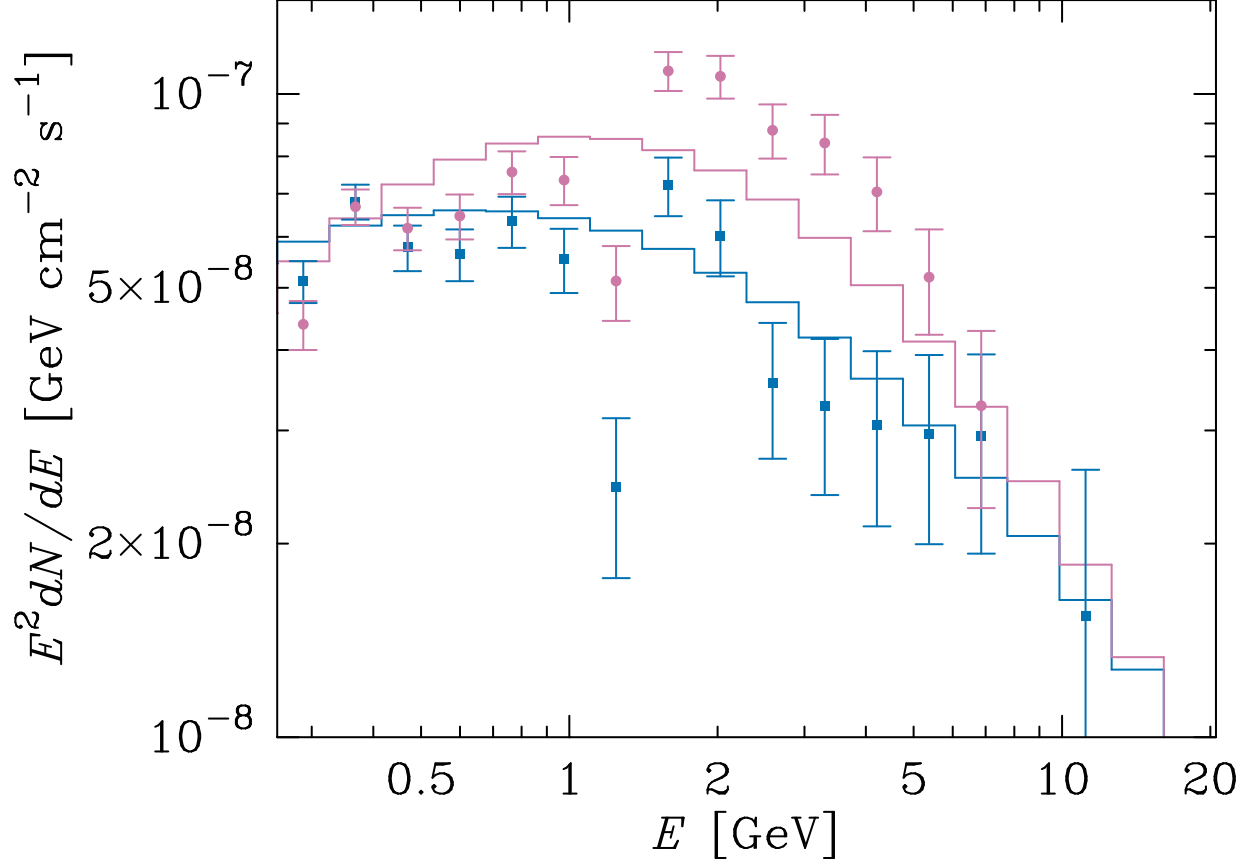
Figure 2.3: Shown are two cases of our determination of the Sgr A* source spectrum. The 2FGL+2PS+I binned spectrum is in pink circles, with best fit binned log-parabola spectrum in pink. The full model 2FGL+2PS+I+MG+ND+GCE spectrum is in blue squares, with best fit binned log-parabola spectrum in blue. The presence of GCE associated photons at 1 to 3 GeV in the Sgr A* spectrum is evident in the case of the 2FGL+2PS+I modeling. The errors shown are solely the Poisson errors within the energy band and do not reflect covariances or systematic uncertainties.

coordinates (b, ℓ) is

$$\frac{d\Phi(b, \ell)}{dE} = \frac{\langle \sigma_A v \rangle}{2} \frac{J(b, \ell)}{J_0} \frac{1}{4\pi m_\chi^2} \frac{dN_\gamma}{dE} \ , \tag{2.3}$$

where dN_γ/dE is the gamma-ray spectrum per annihilation and m_χ is the dark matter particle mass. The quantity J is the integrated mass density squared along line of sight, x,

$$J(b, \ell) = J_0 \int dx \ \rho^2(r_{\text{gal}}(b, \ell, x)) \ , \tag{2.4}$$

16
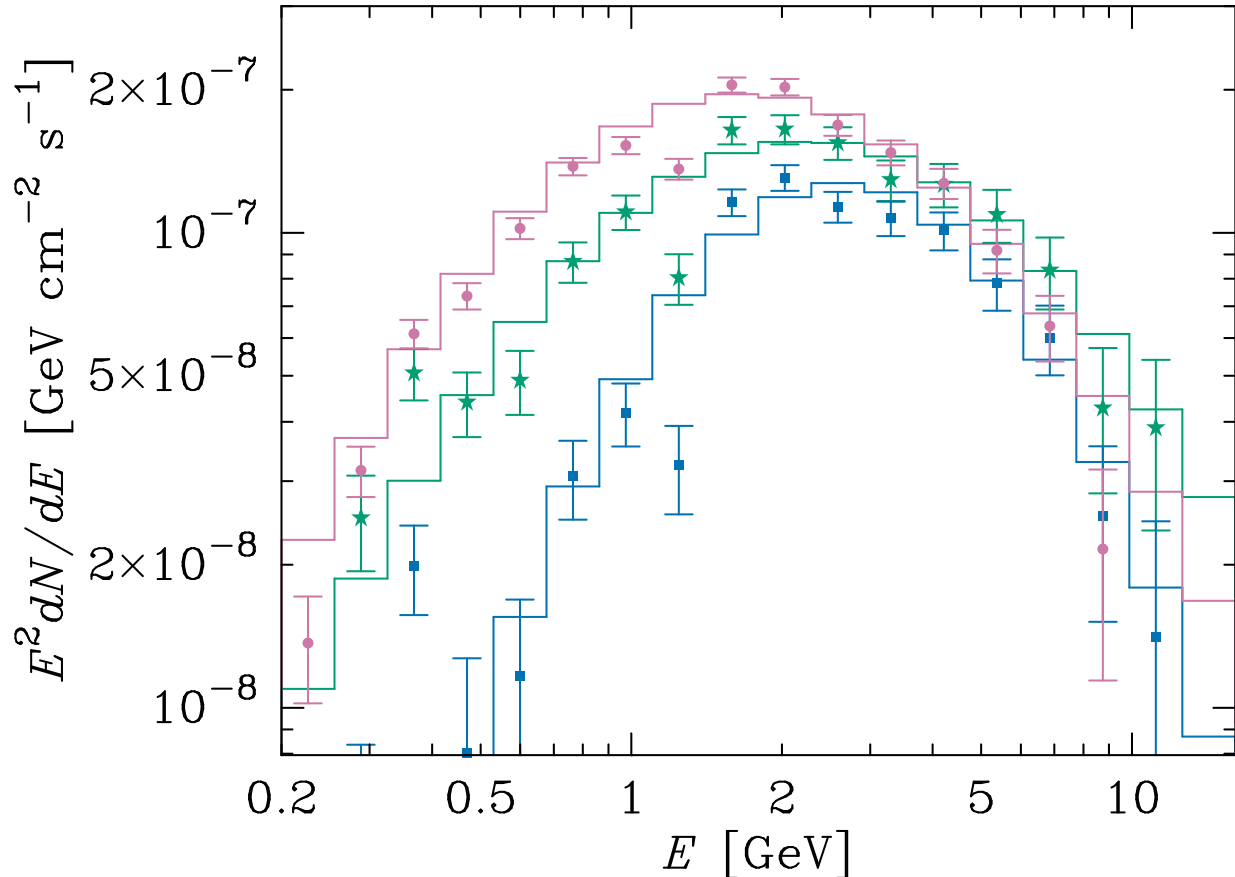
Figure 2.4: Shown are two cases of our determination of the GCE source spectrum. The 2FGL+2PS+I+GCE binned spectrum is in pink circles, with best fit binned log-parabola spectrum shown in pink. The spectrum for the full model 2FGL+2PS+I+MG+ND+GCE is in blue squares, with best fit binned log-parabola spectrum also in blue. We also show the spectrum using `FRONT` converting only photons in green stars, with its best fit binned log-parabola spectrum in green. The errors shown are solely the Poisson errors within the energy band and do not reflect covariances or systematic uncertainties.

where distance from the GC is given by

$$r_{\text{gal}}(b, \ell, x) = \sqrt{R_\odot^2 - 2xR_\odot \cos(\ell)\cos(b) + x^2} \ . \tag{2.5}$$

Here, $J_0 \equiv 1/[8.5 \text{ kpc}(0.3 \text{ GeV cm}^{-3})^2]$ is a normalization that makes J unitless and cancels in final expressions for observables. The value for the solar distance is taken to be $R_\odot = 8.25$ kpc [43]. The density ρ_s for the $\alpha\beta\gamma$ profile is a normalization constant determined uniquely by the local dark matter density, $\rho_\odot$.

17

2.2.3 Method

In order to find the best fit models, and quantify the systematic error inherent in the model-choice dependence in the analyses, we found fits to a very large number of diffuse and extended source model combinations. Our 2FGL+2PS+I model consists of all the 2FGL sources plus the two additional point sources, 1FGL J1744.0-2931c and bkgA, and the new isotropic component. We add to this the MG template and the GCE template individually and then together to test the significance of their detection. Then, we include the ND model and simultaneously vary the density squared γ and 2D projected Γ to find the best fit morphologies for these sources.

For each of the model combination cases, we scan the dark matter particle mass for WIMPs annihilating into $b\bar{b}$, $\tau^+\tau^-$, and a mixture of both channels to find the best fit particle masses. To do this, we add to each model a dark matter source with a ρ^2 spatial template, Eq. (2.2), and spectrum generated via PYTHIA as in Refs. [5, 9]. For finer mass binning, we use gamma-ray spectra generated with DarkSUSY [65] and micrOmegas [27]. Due to the finite intervals between particle masses, we determine the best fit masses and errors for the various mass cases with a fourth order spline interpolation. As can be seen in Fig. 2.9, this method is sufficiently accurate. For each particle mass, we vary all of the model parameters for the Galactic diffuse model, all new added diffuse sources, and all point sources with TS > 25. We repeat this procedure for several different models: for 2FGL+2PS+I+GCE (only point sources and diffuse backgrounds), 2FGL+2PS+I+MG+GCE (with the MG template included), and 2FGL+2PS+I+MG+ND+GCE (the full model, adding both the MG and new diffuse components).

Note that the prompt spectrum produced by the particle annihilation into both b quarks and τ leptons can be significantly modified by bremsstrahlung of the annihilation cascade particles on the dense gas in the GC region [47]. The precise nature and magnitude of

the bremsstrahlung modification of the gamma-ray spectra have a high astrophysical model dependence. In Sec. 2.3.2 below, we describe a test of the bremsstrahlung effects on the observed spectra and their impact on our results.

To illustrate the nature of the sources nearest the GC, we calculate the spectrum of the source associated with Sgr A*. We compute the spectra by creating residual maps for the point source or extended source of interest summing the pixel-based flux (counts divided by exposure) in each energy bin in the residual map of the particular source, using the inner $3° \times 3°$ of the ROI in order to exclude residuals in the outer regions of the ROI. The spectrum for Sgr A* and the GCE source are shown in Figs. 2.3 and 2.4.

2.3   Results & Discussion

Due to the high density of sources—point, extended, and diffuse backgrounds—in the GC region, the inferred nature of cataloged point sources, new point sources, and extended sources depend significantly on the assumed point, extended, and diffuse models. Below, we focus on implications for astrophysical sources, and on the GCE source as interpreted as DM annihilation.

2.3.1   Diffuse sources and Sgr A*

We included a number of new diffuse and extended sources in this analysis, which were detected at high significance. First, the 20 cm MG map was included. The MG component was detected at a TS of 245.4 relative to the model with just the 2FGL+2PS+I sources. Second, we added a ρ^2 GCE template and a two-dimensional projected density profile (ND) and then scanned the morphological parameter space of these components in γ and Γ for each case separately and in combination, with $\Delta\gamma$ and $\Delta\Gamma$ scan step sizes of 0.1, leading to over
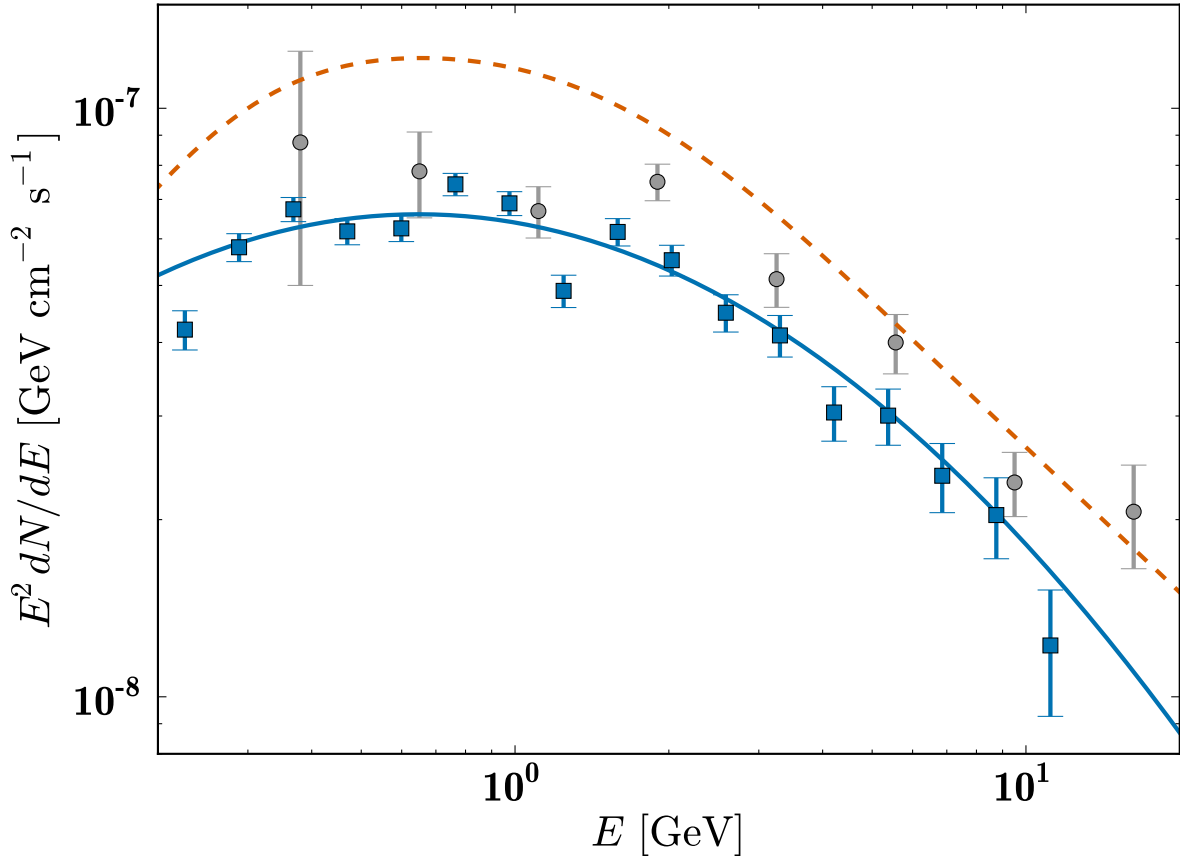
Figure 2.5: Here we show the SED of the source associated with Sgr A* for the full model, 2FGL+2PS+I+MG+ND+GCE (blue squares), as well as its best fit log-parabola spectrum (solid line). For comparison, we show the Sgr A* spectrum determined by Chernyakova *et al.* [45] (gray circles) and the 3 pc diffusion emission model from Linden *et al.* [87] (dashed line). The errors represent the SED-normalization statistical uncertainty within an energy band.

four dozen morphological model tests. The likelihood is shallow in $\Delta\Gamma$ near its minimum: $\Delta\ln\mathscr{L} \approx 0.2$ for $\Delta\Gamma = \pm 0.1$ from their best fit values. The change for $\Delta\gamma = \pm 0.1$ is larger. Fitting a polynomial to the profile likelihood on the variation of γ, we find $\gamma = 1.12 \pm 0.05$ (statistical errors only).

When both the ND and GCE sources are included, i.e., 2FGL+2PS+I+MG+ND+GCE, and their respective indices varied, we found that the best fit values were for $\gamma = 1.1$ and $\Gamma = -0.5$, which resulted in a $2\Delta\ln(\mathscr{L})$ of 334.4 over the model that included neither source,
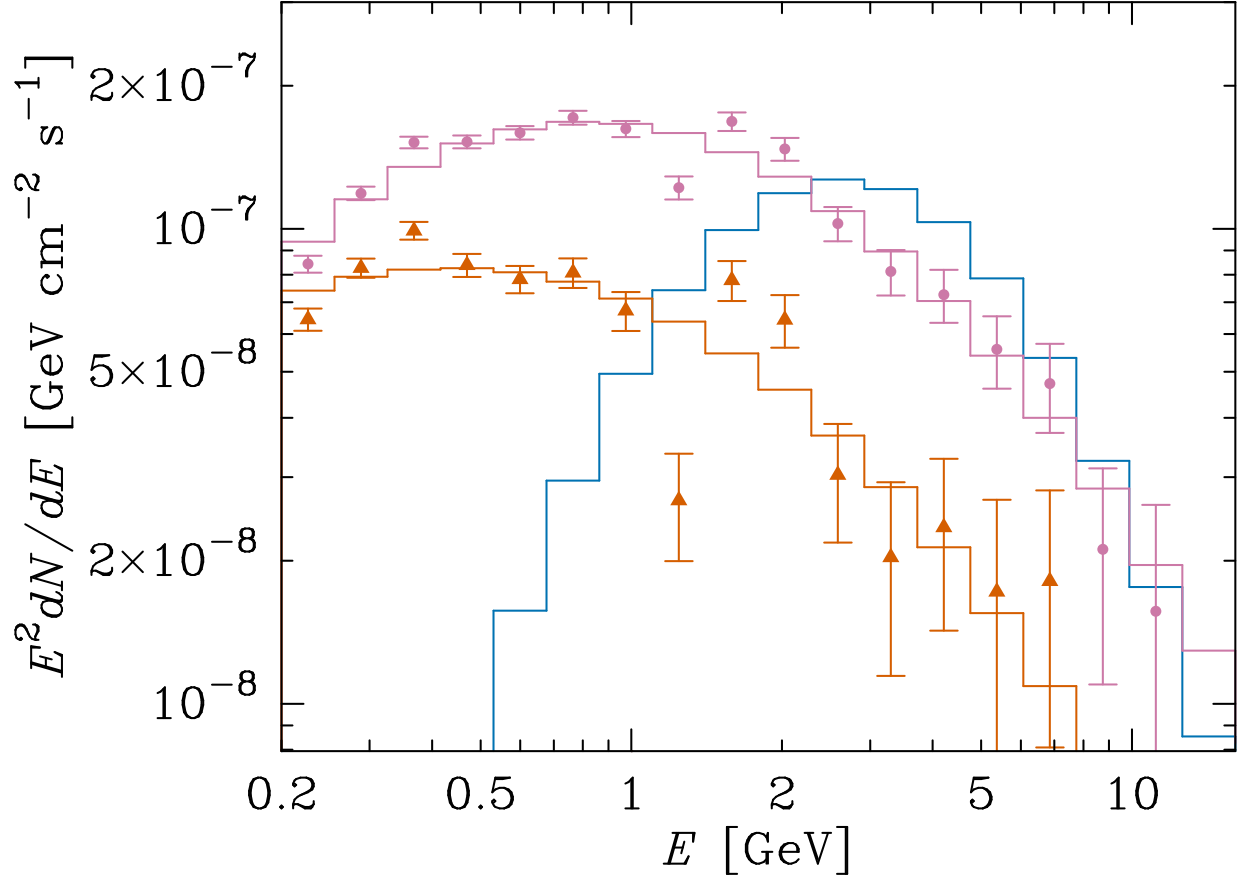
Figure 2.6: Here we show the spectrum for the MG and ND components for the full model 2FGL+2PS+I+MG+ND+GCE. The MG spectrum is in pink circles, with the best fit log-parabola spectrum in pink. The ND spectrum is in orange triangles, with the best fit log-parabola spectrum in orange. For reference, we show the best fit GCE spectrum for the same full model, which shows how the GCE is detected at above ∼2 GeV. The errors shown are solely the Poisson errors within the energy band and do not reflect covariances or systematic uncertainties.

which indicates a strong preference for both of these components in combination. Note that the negative Γ indicates a radially increasing new diffuse (ND) component. Table 2.1 shows the $\ln(\mathscr{L})$ for the various models as well as the $\Delta \ln(\mathscr{L})$ as compared to the 2FGL only model. Table 2.2 shows the flux and TS for the main extended sources and four point sources nearest to the Galactic Center.

Including the ND source without the MG or GCE sources is a significantly poorer fit overall since it is not as centrally concentrated as the MG and GCE templates. Therefore, we do
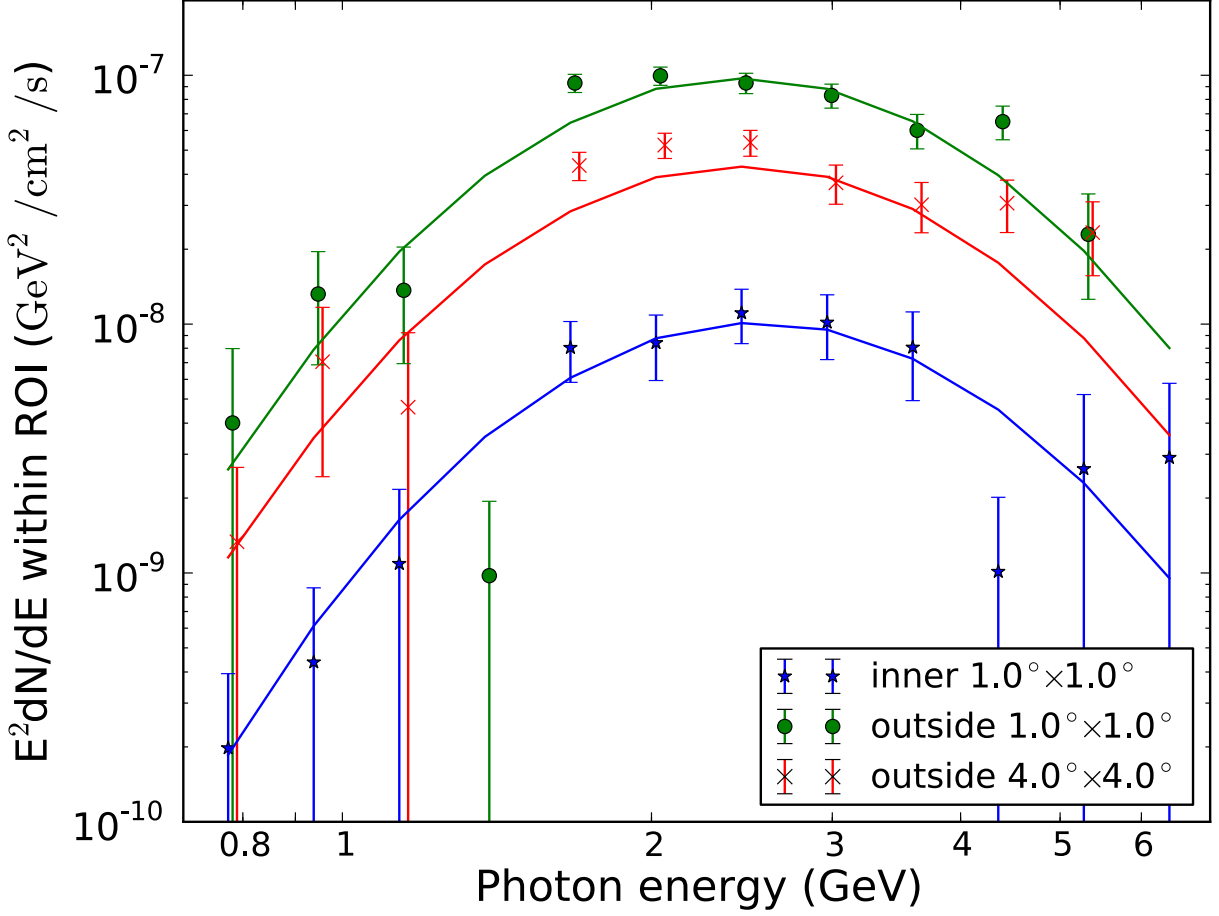
Figure 2.7: Here we show the residual flux for the GCE for different spatial regions within the ROI for the 2FGL+2PS+MG+GCE model as well as the flux from the model counts for $\gamma = 1.1$. It is clear that all the different regions are being well fit by the NFW-like density profile. The errors shown are solely the Poisson errors within the energy band and do not reflect covariances or systematic uncertainties.

not consider this model case further.

Very significantly, the presence of the GCE, MG, and ND diffuse sources affects the inferred properties of the central point sources, particularly Sgr A*, as shown in Fig. 2.3. In the 2FGL+2PS model, Sgr A* has a total flux of $(3.13 \pm 0.16) \times 10^{-7}$ ph cm^{-2} s^{-1}, and a curved spectrum that is consistent with the features seen in previous work by Chernyakova et al. [45], with a log-parabola spectrum of $N_0 = (3.112 \pm 0.068) \times 10^{-11}$ MeV^{-1} cm^{-2} s^{-1}, $\alpha = 2.242 \pm 0.025$, $\beta = 0.273 \pm 0.018$. However, with the inclusion of the detected GCE

source as well as MG and ND sources, Sgr A* is less peaked. The GCE shows a peaked spectrum (Fig. 2.4) which suggests that photons that were previously associated with Sgr A* are now being associated to the GCE source. With the new diffuse and extended sources, Sgr A* becomes nearly a power law with a log-parabola spectrum of $N_0 = (2.181 \pm 0.082) \times 10^{-11}$ MeV^{-1} cm^{-2} s^{-1}, $\alpha = 2.32 \pm 0.032$, $\beta = 0.173 \pm 0.020$, and a commensurate reduction in flux to $(2.89 \pm 0.18) \times 10^{-7}$ ph cm^{-2} s^{-1}.

In Fig. 2.5 we also show results of a banded SED fit for Sgr A*'s spectrum in the full 2FGL+2PS+I+MG+ND+GCE by independently fitting the normalization of the Sgr A* flux while fixing other sources within that energy band. This is similar to the residual flux spectrum and provides a useful cross-check (see Appendix for more details).

Note that our spectra for Sgr A* and the GCE source have a spectral feature downturn and upturn at $E_\gamma \approx 1.3$ GeV. We find this feature in the full photon counts in the ROI, and it is possible that this is an artifact of energy identification in the Fermi tools at this energy.

Our best fit model for Sgr A* has implications for interpretations of its gamma-ray emission. In the hadronic scenario, the ∼GeV peak is associated with emission from diffusively trapped protons. As the protons transition to rectilinear motion at higher energies, they reproduce the flatter spectrum observed at $\mathscr{O}$(TeV) energies [45, 87]. In the context of this scenario, the newly determined flatter spectrum near ∼1 GeV implies changes to the diffusion parameters. For example, reasonable reductions to the diffusion coefficient energy dependency and/or diffusion coefficient normalization can generate such flatter spectra [45]. Alternatively, reducing the Sgr A* activity duration, or reducing the proton diffusion region to smaller than the saturation level of 3 pc as described in Ref. [87], reduces the ∼GeV intensity and generates a flatter spectrum.

When fitting in our full model with extended sources and the new diffuse component, the 2FGL+2PS+I+MG+ND+GCE model, the emission associated with the MG has a spectrum

best fit with $N_0 = (1.68 \pm 0.14) \times 10^{-9}$ MeV^{-1} cm^{-2} s^{-1} sr^{-1}, $\alpha = 1.487 \pm 0.075$, $\beta = 0.297 \pm 0.031$ for $E_b = 300$ GeV. The best fit spectra for the MG and ND components are shown in Fig. 2.6, along with the GCE spectrum for reference.

Reference [121] interpreted the gamma-ray emission from the 20 cm correlated MG to be from bremsstrahlung of a high-energy population of electrons on the molecular gas. However, our new model xfits with additional sources reveal an intensity peaked at energies of $\sim$1 GeV, which is slightly high. In bremsstrahlung, typically half the $e^\pm$ energy is emitted; thus, the gamma-ray spectrum follows the cosmic-ray $e^\pm$ spectrum. The electron spectrum in turn is set by the dominant cooling or escape processes. The bremsstrahlung energy loss time as $e^\pm$ traverse pure hydrogen of number density n is $t_{\rm brems} \approx 40 \, (n/{\rm cm}^{-3})^{-1}$Myr, but since the ionization loss time $t_{\rm ion} \approx 1380 \, E_{\rm GeV}(n/{\rm cm}^{-3})^{-1}[\ln E_{\rm GeV} + 14.4]^{-1}$ dominates at low energies, the $e^\pm$ and gamma-ray spectra soften, yielding a peak at ~ 400 MeV, independent of the target density. On the other hand, the break could result from a break in the cosmic ray (CR) electron spectrum. As argued in Ref. [121], such an interpretation is consistent with the observed radio emission in the GC region.

Based on the bremsstrahlung interpretation, information of the molecular gas density can be obtained. The MG and ND spectra above the peak imply a CR electron spectrum $dN/dE \propto E^{-p}$ with $p \sim 3$. The same CR electron population will synchrotron radiate in the radio with a spectrum $F_\nu \propto \nu^{-\alpha}$ and $\alpha = (p-1)/2 \sim 1$. For a power-law CR electron population, the synchrotron radio and bremsstrahlung gamma emissions are related by, e.g., Eq. (12) of Ref. [121]. We adopt a magnetic field of $10 \, \mu$G in the GC region, which is within a factor of 2 of the range estimated from the CR ionization rate [121], and implies an electron of energy E_e radiates $\sim 5(B/10\mu{\rm G})(E_e/6{\rm GeV})^2$ GHz radio and emits $\sim 3(E_e/6{\rm GeV})$ GeV gamma rays. Requiring that the observed radio at 5 GHz towards the GC ($S_{\rm 5GHz} \sim 10^3$ Jy [121]) is not overpredicted, the MG and ND estimates imply a lower limit on the molecular gas density of $n_H \gtrsim 4 \, {\rm cm}^{-3}(S_{\rm 5GHz}/1000{\rm Jy})^{-1}$.

The emission associated with the new diffuse source for the full model, the best fit log-parabola spectrum is $N_0 = (1.69 \pm 0.39) \times 10^{-5}$ MeV^{-1} cm^{-2} s-1 sr^{-1}, $\alpha = 0.95 \pm 0.17$, $\beta = 0.308 \pm 0.047$ for $E_b = 100$ MeV. This is essentially the same as the MG spectrum and this result likely indicates the presence of molecular gas not captured by the Galactic diffuse model and the MG template.

For the analysis with photons in the restricted $0.7 - 7$ GeV energy range, we did not detect the $\Gamma = -0.5$ ND source. Hence, we only show results for the E7 analysis without including the ND source, $i.e.$, E7-2FGL+2PS+nPS+MG+GCE. The MG spectrum in the E7 energy window has an index of almost -2.0 (with no significant variations), which is different from the fit using the full model. This is not altogether surprising given the weight from lower energy photons in constraining the MG spectrum in the full model. The differences may also be due to degeneracies between GCE and MG in this restricted energy window given the similarity in their spectra at energies above about a GeV (see Fig. 2.6).

In the full model, 2FGL+2PS+I+MG+ND+GCE, the emission associated with the GCE source is best fit by log-parabola spectrum with $N_0 = (1.20 \pm 0.46) \times 10^{-12}$ MeV^{-1} cm^{-2} s-1 sr^{-1}, $\alpha = -4.28 \pm 0.18$, $\beta = 0.959 \pm 0.026$ for $E_b = 100$ MeV. The GCE emission is almost equally well fit by a power law with an exponential cutoff $dN/dE = N_0(E/E_0)^{-\gamma_c} \exp(-E/E_c)$ and the best fit spectral parameters are $\gamma_c = 0.45 \pm 0.21$, $E_c = 1.65 \pm 0.20$ GeV and $N_0 = (1.03 \pm 0.56) \times 10^{-9}$ MeV^{-1}cm^{-2} s^{-1} sr^{-1} for $E_0 = 100$ MeV.

One of the key features of the GCE excess is the striking similarity to the ρ^2 spatial profile expected of annihilation signals. To investigate this further we did two tests with the E7 data. First, for the E7-2FGL+2PS+nPS+MG+GCE, we plotted the residual flux spectra in different spatial regions and that is shown in Fig. 2.7. It is clear that the excess is present throughout the ROI and not just concentrated at the center. This is partly why the GCE is robustly found in different analyses. We take this one step further with a new model E7-2FGL+2PS+nPS+MG+GCE(a)+GCE(b) where GCE(a) is GCE with pixels outside a

radius of 2.5° zeroed out and GCE(b) = GCE - GCE(a) is the complementary region with $\gamma = 1.1$ in all cases. We found that there are fits that are statistically almost as good as the E7-2FGL+2PS+nPS+MG+GCE ($\gamma = 1.1$) case but have different spectra for the inner and outer parts. In particular, the best fit peak in intensity for the outer part seems to be at somewhat larger energy (but still between 2 and 3 GeV) . The $\Delta \ln \mathscr{L}$ is around 10 for these models compared to the E7-2FGL+2PS+nPS+MG+GCE ($\gamma = 1.1$) case and that is not significant enough to claim deviations from our baseline model with GCE.

What the above does bring up is the possibility that the fit can accommodate more than one diffuse component as part of the GCE—perhaps due to MSPs and dark matter. This exciting possibility deserves further study and we suggest that it should be considered equally as likely as the pure dark matter hypothesis since the best fit spectrum from dark matter annihilation is very similar to the MSP spectrum [4]. To illustrate this point, we show a plot of the GCE spectra from our full model compared to the spectra of eight globular clusters that were observed with Fermi LAT. We have focused in on the region around a GeV and higher since that is where we are (comparatively) more confident in our background modeling. We have also normalized all the spectra by their fluxes for $E > 2$ GeV to make the comparison easier. The similarity of the GCE excess with the spectra from globular clusters is readily apparent.

2.3.2 Dark matter interpretation

When interpreting the GCE source as originating in dark matter annihilation, we found that the best fit mass for annihilation into $b\bar{b}$ was $31.4^{+1.4}_{-1.3}$, $35.3^{+2.4}_{-2.2}$, and $39.4^{+3.7}_{-2.9}$ GeV for the 2FGL+2PS+GCE, 2FGL+2PS+I+MG+GCE, and 2FGL+2PS+I+MG+ND+GCE models, respectively. The amplitude for annihilation rate $\langle \sigma v \rangle_{b\bar{b}}$ for the full model 2FGL+2PS+I+ MG+ND+GCE is $(5.1 \pm 2.4) \times 10^{-26}$ cm^3 s^{-1}. For annihilation into $\tau^+\tau^-$, the best fit masses were $8.21^{+0.30}_{-0.24}$, $8.79^{+0.44}_{-0.42}$ and $9.43^{+0.63}_{-0.52}$ GeV for the 2FGL+2PS+GCE, 2FGL+2PS+I+MG+
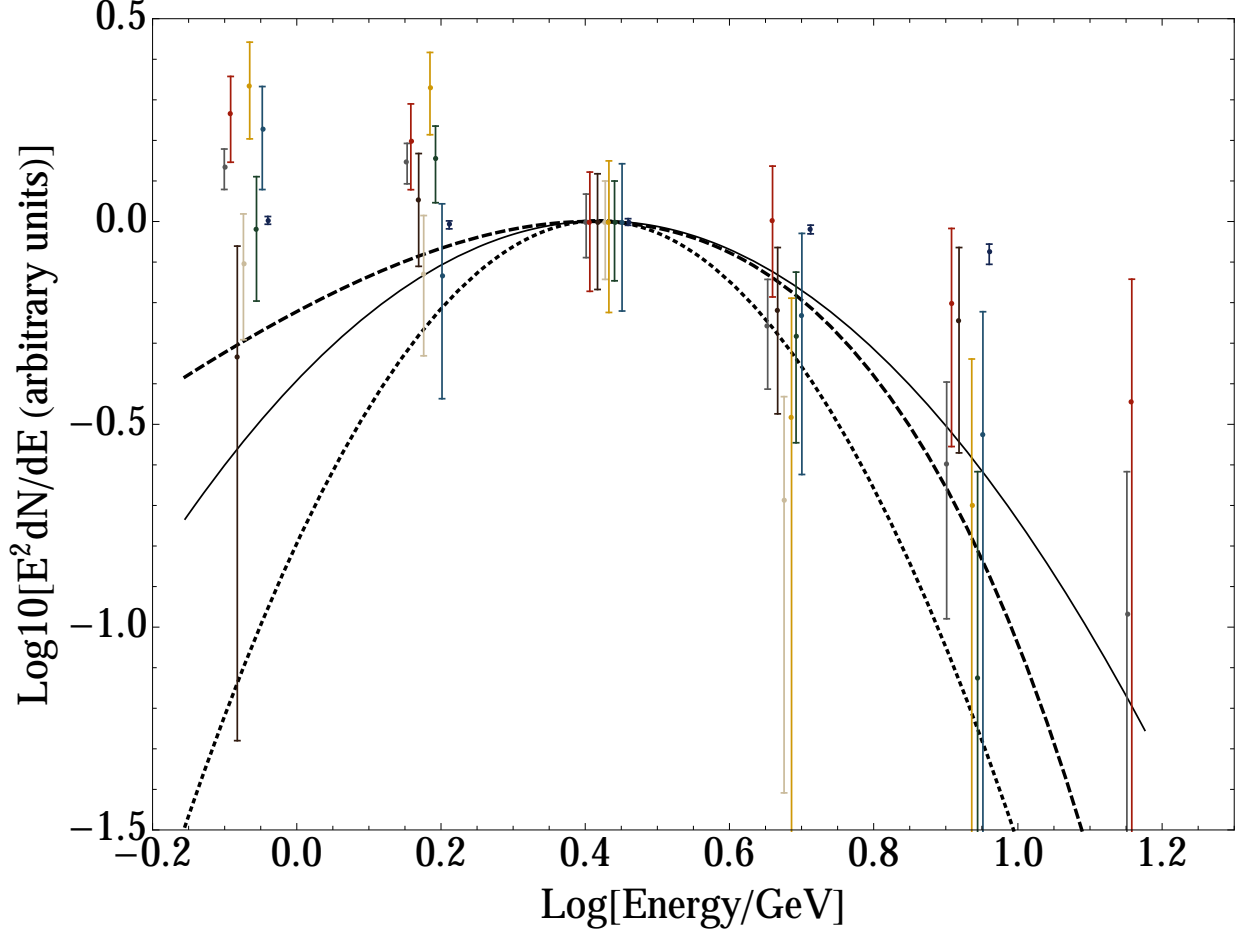
Figure 2.8: Here we compare the flux spectra of the best fit GCE source with the flux spectra from eight globular clusters detected by Fermi LAT (47 Tuc, ω Cen, M62, NGC 6388, Terzan 5, NGC 6440, M28, NGC 6652). The three best fit GCE spectra shown are from the full model with a power-law exponential cutoff spectrum (solid), from the full model with a log-parabola spectrum (dashed) and from the 0.7–7 GeV analysis with a log-parabola spectrum (dotted). All the spectra are normalized by their fluxes for energies greater than 2 GeV.

GCE, and 2FGL+2PS+I+MG+ND+GCE models, respectively. The amplitude for annihilation rate $\langle \sigma v \rangle_{\tau^+ \tau^-}$ for the full case 2FGL+2PS+I+MG+ND+GCE is $(0.51 \pm 0.24) \times 10^{-26}$ cm^3 s^{-1}.[1] These mass fit $2\Delta \ln(\mathscr{L})$ curves are shown in Fig. 2.9.

When using the 2FGL+2PS+I+MG model, the b-quark channel is preferred over τ leptons by a $\Delta \ln(\mathscr{L}) \approx 17.9$. This is consistent with recent results applying the 20 cm radio map as well as Galactic ridge template models to dark matter annihilation models [89], which

---

[1]The errors on $\langle \sigma v \rangle$ are dominated by the uncertainty in the local dark matter density, which we adopt as $\rho_\odot = 0.3 \pm 0.1$ GeV cm^{-3} [122].

Table 2.2: Flux, in units of 10^{-7} ph cm^{-2} s^{-1} within 0.2 - 300 GeV, in the $7° \times 7°$ ROI and TS $= 2\Delta\ln(\mathscr{L})$ values for several sources in the GC region for our full 2FGL+2PS+I+MG+ND model. The TS values are determined with reoptimization of the respective models with the same morphological parameters γ and Γ. We leave the TS value for the Galactic diffuse case as an approximation due to its very high significance.

Source Name	Flux	TS
2FGL J1745.6-2858 (Sgr A*)	2.89 ± 0.18	789.6
2FGL J1747.3-2825c (Sgr B)	0.573 ± 0.098	179.8
2FGL J1746.6-2851c (the Arc)	0.773 ± 0.182	67.1
2FGL J1748.6-2913	0.361 ± 0.082	90.3
MG	7.29 ± 0.52	185.7
GCE $\gamma = 1.1$	1.08 ± 0.10	170.7
ND $\Gamma = -0.5$	2.99 ± 0.38	73.5
Galactic diffuse	34.8 ± 0.46	$\gtrsim 10^4$

find a preference for the b-quark annihilation channel. As can be seen in Figs. 2.4 and 2.10, the steepness of the rise of the spectrum is highly diffuse-emission model and GCE-spectral model dependent, and it is therefore problematic to draw conclusions on the nature of the emission from the residual spectra and rise shapes of SED spectra alone, as is done, e.g., in Refs. [72, 74]. These large variations in best fit spectra (specifically below about GeV) are indicative of degeneracies that can only be accounted for in a full likelihood spatial and spectral analysis of the type performed here and in Ref. [89].

In the case of mixed channels (arbitrary branching ratio into $b\bar{b}$ and $\tau^+\tau^-$) in the full model, 2FGL+2PS+I+MG+ND+GCE, we find no preference for mixed channels, with the likelihood profile having a minimum at full b-quark channel annihilation at higher $m_\chi \approx 30 - 40$ GeV and annihilation into τ leptons at lower masses $m_\chi \approx 10$ GeV, with these two minima separated only by $\Delta\ln(\mathscr{L}) = 0.8$. If we do not include the molecular gas contribution, then the preferred dark matter masses shift to lower values.

Importantly, bremsstrahlung effects of the annihilation products can appreciably modify the gamma-ray spectra [47]. In particular, the work in Ref. [47] found that the $\tau^+\tau^-$ channel is softened, or, less steep at low energies, under standard assumptions for the gas density and
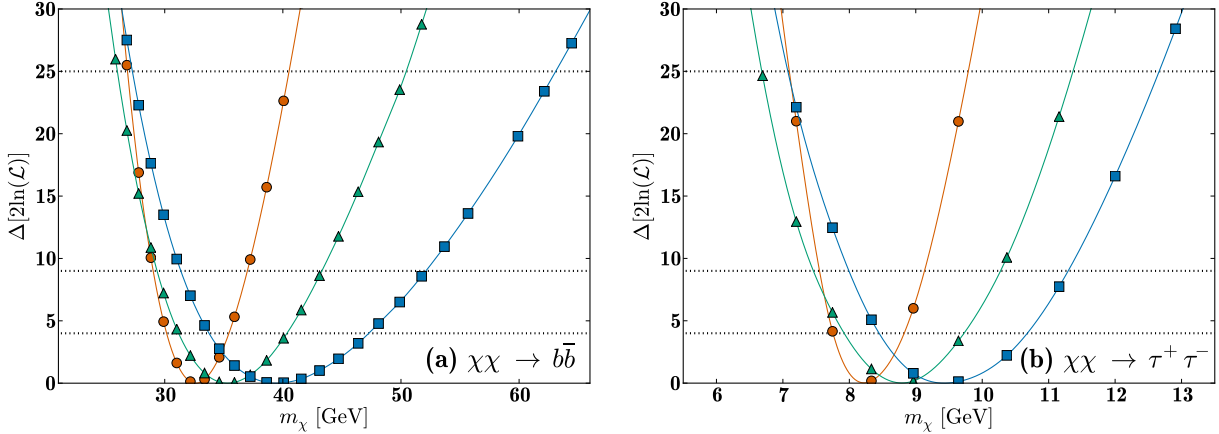
Figure 2.9: Shown are the $2\Delta \ln(\mathcal{L})$ for the best fit dark matter particle masses for (a) pure $b\bar{b}$ and (b) pure $\tau^+\tau^-$ annihilation channels, for several astrophysical model cases studied when varying all sources on the GC ROI. In both panels, the cases for 2FGL+2PS+GCE show the exact particle mass runs in orange circles, 2FGL+2PS+I+MG+GCE case in green triangles and the full best fit model 2FGL+2PS+I+MG+ND+GCE case in blue squares. Fourth order spline interpolations are shown as lines for each case, which are used to find the minima and limits. For the full 2FGL+2PS+I+MG+ND+GCE model, the $b\bar{b}$ and $\tau^+\tau^-$ are equivalent in their goodness of fit, and there is no evidence for a mixed channel. The horizontal lines are for $2, 3$ and 5σ limits.

magnetic fields in the GC.

To test the magnitude of the effects of bremsstrahlung of final state particles in the astro-physical environment of the GC, we utilize the following approximation of the effects. We apply the bremsstrahlung spectra for the "realistic gas density" for the $m_\chi = 25$ GeV $b\bar{b}$-channel and $m_\chi = 20$ GeV $\tau^+\tau^-$-channel cases in Fig. 4 of Ref. [47] as the magnitude of the effect for all particle masses of interest. We scale the bremsstrahlung photon spectra energies with the particle masses proportionally with the prompt spectra over our particle mass range. We then rederive the best fit particle mass determinations. This method is an approximation of the bremsstrahlung effects, but provides an order-of-magnitude estimate of the modification of gamma-ray spectra due to particle bremsstrahlung in the annihila-tion cascade. When adding the bremsstrahlung photons in the manner described, we find that the best fit particle masses are, for the $b\bar{b}$ channel, $m_\chi = 40.9^{+3.6}_{-3.4}$ GeV, and for the

$\tau^+\tau^-$-channel, $m_\chi = 10.17^{+0.54}_{-0.59}$ GeV. The larger best fit masses reflect the softening of the spectra that allows more massive particles to fit the observed photon spectrum. Because the effect is relatively small, this shift is subsumed in the systematic errors in Eqs. (2.6) and (2.7) below, which are dominated by diffuse model uncertainties. However, it is notable that with the bremsstrahlung spectral modification, we find that the $\tau^+\tau^-$ channel is preferred by $\Delta\ln(\mathscr{L}) = 4.5$, which is statistically significant at approximately $\sim 3\sigma$. More detailed work on the particle bremsstrahlung is warranted, but beyond the scope of this chapter.

The statistical error on the dark matter particle mass producing the signal is quite small in these cases, at better than 10% in all cases. However, the systematic error associated with uncertainties in the astrophysical diffuse models, present in particular with true fractional MG contribution along the line of sight, render the systematic uncertainty relatively large, at about 20%. Therefore, our determination of the dark matter particle mass and annihilation rate in the pure $b\bar{b}$ channel is

$$
\begin{aligned}
m_\chi &= 39.4 \left(^{+3.7}_{-2.9} \text{ stat.}\right) \left(\pm 7.9 \text{ sys.}\right) \text{ GeV} \\
\langle\sigma v\rangle_{b\bar{b}} &= (5.1 \pm 2.4) \times 10^{-26} \text{ cm}^3 \text{ s}^{-1},
\end{aligned}
\tag{2.6}
$$

where the best fit value is determined by the full model, 2FGL+2PS+I+MG+ND+GCE. The annihilation rate is below the most stringent constraint on this region, from the four year combined dwarf analysis, with an upper limit requiring $\langle\sigma v\rangle_{b\bar{b}} \lesssim 6.5 \times 10^{-26}$ cm^3 s^{-1} (95% C.L.) [13].

Note that there are significant constraints on the annihilation through specific interaction operators at comparable rates from dark matter searches at the Large Hadron Collider [44, 2, 67]. In particular, annihilation into quarks at our best-fit m_χ is constrained by ATLAS [2] to be $\langle\sigma v\rangle_{\tau^+\tau^-} \lesssim 2(40) \times 10^{-26}$ cm^3 s^{-1} (95% CL) for axial-vector (vector) interaction

couplings.

In the case of a pure $\tau^+\tau^-$ channel we find

$$
\begin{aligned}
m_\chi &= 9.43 \left(^{+0.63}_{-0.52} \text{ stat.}\right) (\pm 1.2 \text{ sys.}) \text{ GeV} \\
\langle \sigma v \rangle_{\tau^+\tau^-} &= (0.51 \pm 0.24) \times 10^{-26} \text{ cm}^3 \text{ s}^{-1},
\end{aligned}
\tag{2.7}
$$

where the best-fit value is again determined by the full model, 2FGL+2PS+I+MG+ND+ GCE. The annihilation rate in this channel is also below the most stringent constraint on this region, from the 4 year combined dwarf analysis, with an upper limit requiring $\langle \sigma v \rangle_{\tau^+\tau^-} \lesssim 2.3 \times 10^{-26}$ cm^3 s^{-1} (95% CL) [13]. As discussed above, our determined uncertainties in $\langle \sigma v \rangle$ are dominated by the local dark matter density uncertainty. There are systematic uncertainties on the annihilation rates in Eqs. (2.6) and (2.7) due to the diffuse model and dark matter profile γ uncertainties, but they are smaller than the uncertainties due to the local dark matter density.

Interpreting the GCE emission in dark matter models beyond the single channel cases we present here requires significant care. The nature of the GCE source and photons associated with the source depends on the underlying assumption of the spectrum and morphology of the dark matter GCE source, as well as the modeling of the other diffuse and point sources in the region, as discussed above and shown in Fig. 2.4. To illustrate, we show the GCE spectra for our full model for several spectral model cases in Fig. 2.10. Here, we fit the spectral energy distribution (SED) of the GCE source independently in energy bins across the energy range of interest, while keeping the other sources fixed in that energy bin. This provides an estimate of the statistical uncertainty of the GCE source spectrum including covariance with other source fluxes. We refit the SED with this method for the log-parabola, power law with exponential cutoff, as well as the b-quark and τ-annihilation channels. It is

clear from Fig. 2.10 that the derived nature of the source spectrum depends on the assumed spectrum. Though still approximate, the best estimate of the GCE spectrum, including its overall statistical and systematic uncertainty, would be the full range of errors between the upper-most and lower-most points' errors in Fig. 2.10.
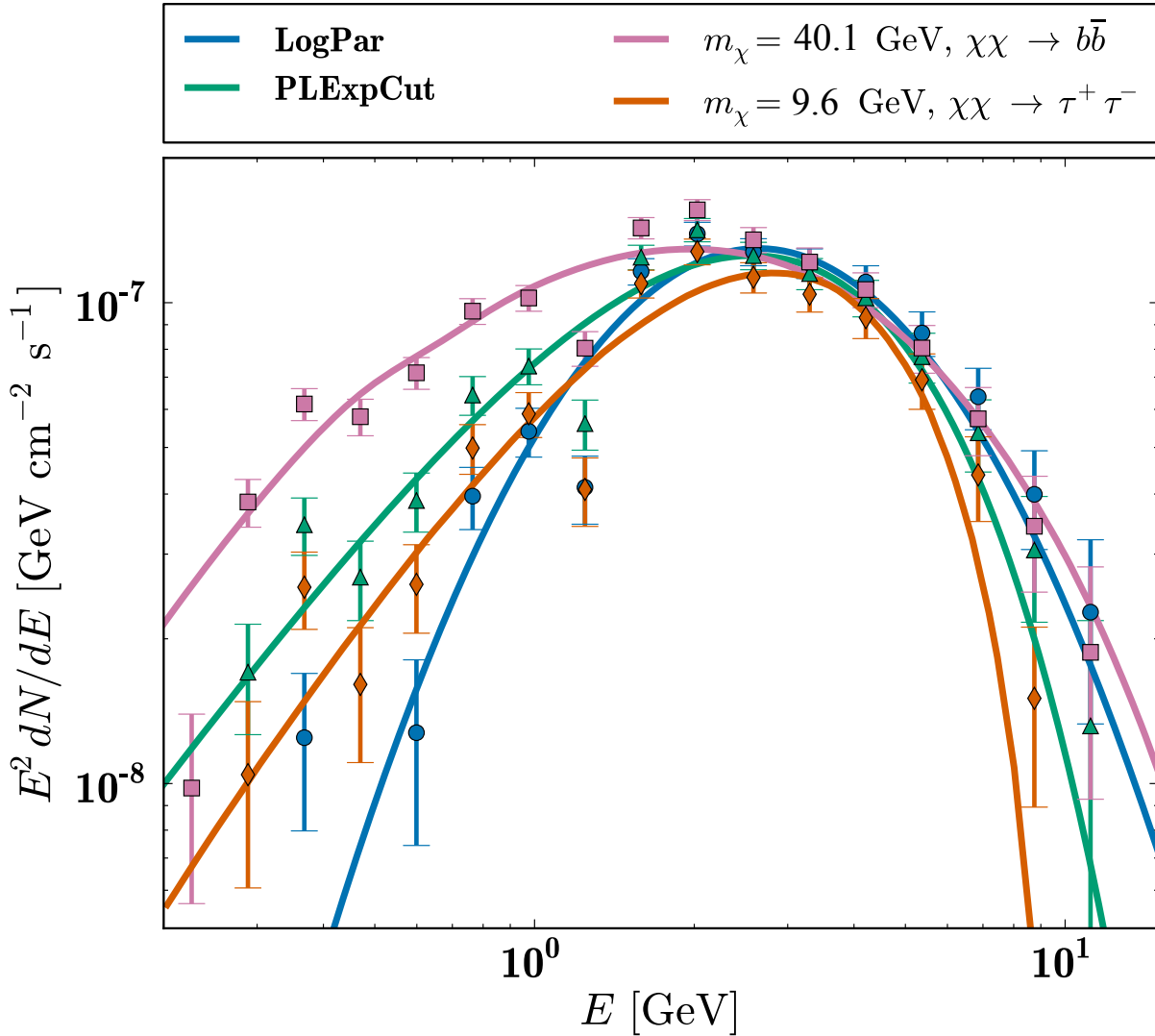
Figure 2.10: Shown are the systematic and statistical uncertainties in determining the GCE source spectrum. The errors represent the SED-normalization statistical uncertainty within an energy band, while the several cases represent the inherent systematic uncertainty present in the adoption the GCE source's spectral form.

2.3.3 Astrophysical interpretations & limits on dark matter contribution

There were significant detections of an extended source consistent with a dark matter interpretation into the quark channel in all of our models. However, as discussed in the introduction and in previous studies, this emission is also consistent with a population of MSPs as shown by the comparison of the spectra in Fig. 2.8. To estimate the required MSP population within the ROI, we use 47 Tuc as a reference. As we have seen previously, the flux estimates of the GCE source have large systematic uncertainties below about 2 GeV. The spectrum of the GCE is also more consistent with those of globular clusters (including 47 Tuc) above this energy. So we choose to compare the fluxes at $E > 2$ GeV. If 47 Tuc were at the GC its flux above 2 GeV would be 3×10^{-10} cm^{-2}s^{-1}. The current estimate for the number of MSPs in 47 Tuc is around 30. We use this to estimate the flux per MSP contributing to the GCE to be 10^{-11}cm^{-2}s^{-1}. The total flux for the best power law with exponential cutoff spectrum is 4.8×10^{-8} cm^{-2}s^{-1}, which implies about 4800 MSPs are required within the ROI, while the same calculation for the log-parabola spectrum from the full model yields 3700 MSPs within the ROI.

Consistent with previous work, when we included a dark matter source in addition to the MSP source, there was no significant dark matter detection, because we assumed the spatial morphologies to be the same [10] and since the log-parabola spectrum is sufficiently flexible. If we assume that all of the GCE emission is astrophysical (e.g., unresolved MSPs), we can place limits on the annihilation cross section for a potential WIMP contribution. We find that this limit is highly dependent on which model components we include. The various limits for annihilation into $b\bar{b}$ and their dependence on three different models can be seen in Fig. 2.11.

We derive the 95% C.L. limits on the dark matter annihilation cross section given each of
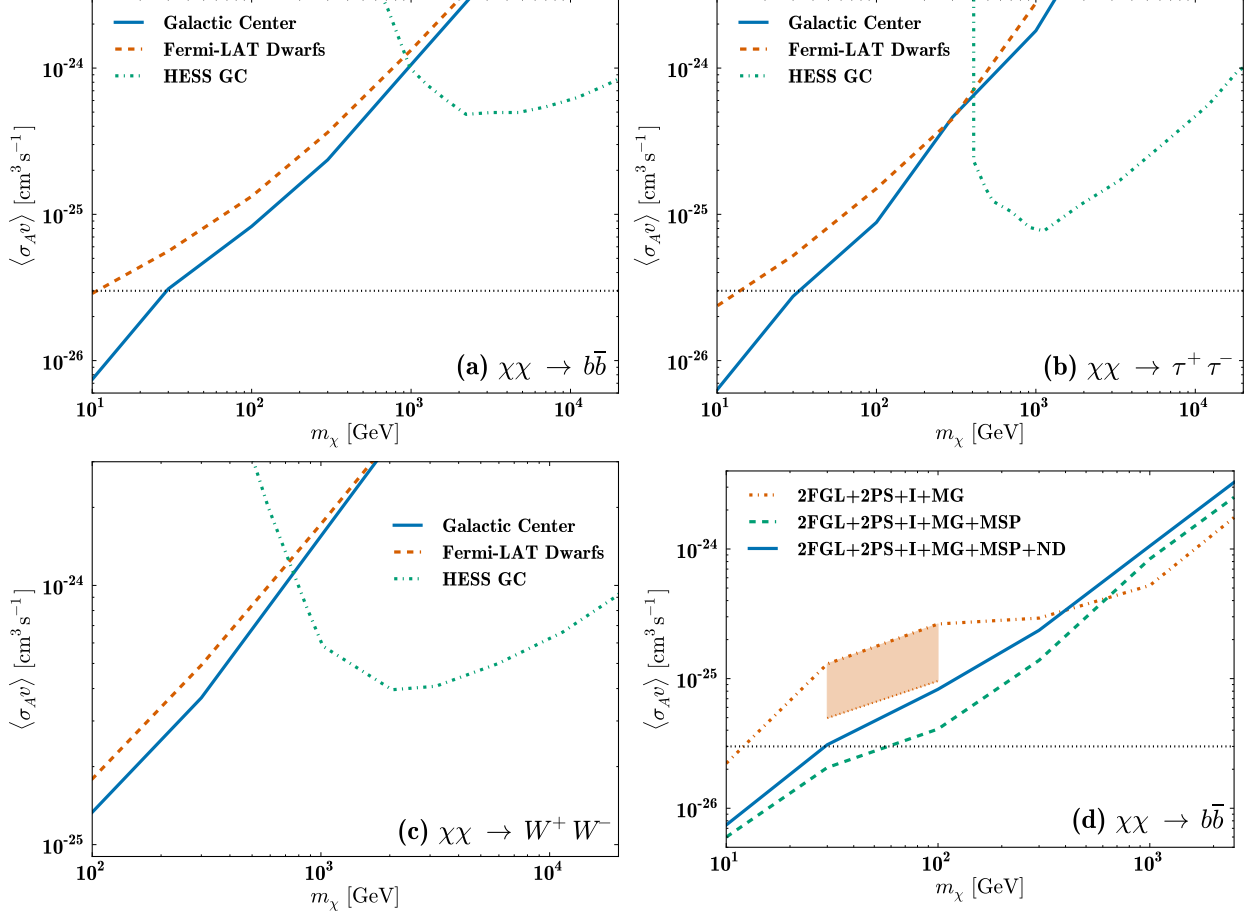
Figure 2.11: Shown are limits on several channels when assuming that the new extended source is associated with MSP or other astrophysical emission in the models we study, for (a) the $b\bar{b}$, (b) $\tau^+\tau^-$, and (c) W^+W^-, in comparison with combined dwarf galaxy limits [13] and limits from HESS observations toward the Milky Way GC [9]. In (d) we show the strong model dependence of the limits, with the adopted full model limits being 2FGL+2PS+I+MG+MSP+ND solid (blue). The shaded box is for the case of 2FGL+2PS+MG, where there is the detection.

these astrophysical models by increasing the flux from the best fit value for the dark matter source and then refitting all significantly detected parameters in the ROI until $2\Delta\ln(\mathscr{L}) = 2.71$ for the one-sided confidence level. This is done for the $b\bar{b}$ and $\tau^+\tau^-$ channels for masses 10, 30, 100, 300, 1000, and 2500 GeV, and for the W^+W^- channel for masses 100, 300, 1000, and 2500 GeV. We use only photons from 700 MeV to 300 GeV as this range was found to provide a more stringent limit.

For our adopted shown limits, we use our full 2FGL+2PS+I+MG+ND+GCE model, i.e., including the two additional point sources, the new isotropic component, the MG template, $\gamma = 1.1$ MSP template, a $\gamma = 1.0$ DM template, and the new diffuse component with $\Gamma = -0.5$. These limits are shown in Figs. 2.11(a)-2.11(c) for annihilation in $b\bar{b}$, $\tau^+\tau^-$, and W^+W^-, and are slightly more stringent than the four year Fermi stacked dwarf limits [13]. We also show, for comparison, the limits from High Energy Stereoscopic System (HESS) observations toward the Milky Way GC [12, 9]. Note, however, the GC limits are highly dependent on the adopted diffuse-emission models, as shown in Fig. 2.11(d). Therefore, though the GC DM limits are stringent, they are not robust to underlying model assumptions, contrary to some previous claims [73].

2.4   Conclusions

We have presented the results of a large set of analyses of the nature of point source, diffuse and extended source gamma-ray emission toward the Milky Way's Galactic Center as observed by the Fermi LAT. We have included all known point sources toward the GC as well as a template of the molecular gas based on radio emission. In all cases, we find a highly statistically significant robust detection of an extended source consistent with dark matter annihilation and/or a population of millisecond pulsars in the GC. However, the detailed spectrum of this extended source depends strongly on the background (diffuse source) models.

The spectrum of the source associated with Sgr A* is less steep than in previous work, owing to the new extended and diffuse sources. In the case of a dark matter annihilation interpretation of the GC extended source, the particle mass is very precisely determined given an annihilation channel, though systematic uncertainties in the diffuse emission introduce significant systematic uncertainties. The b-quark or τ-lepton channels are almost equally

preferred, but with different particle masses. For annihilation into b quarks we find $m_\chi = 39.4 \left(^{+3.7}_{-2.9} \text{ stat.} \right) (\pm 7.9 \text{ sys.})$ GeV, $\langle \sigma v \rangle_{bb} = (5.1 \pm 2.4) \times 10^{-26}$ cm^3 s^{-1}. For the $\tau^+ \tau^-$ channel we find $m_\chi = 9.43 \left(^{+0.63}_{-0.52} \text{ stat.} \right) (\pm 1.2 \text{ sys.})$ GeV, $\langle \sigma v \rangle_{\tau^+ \tau^-} = (0.51 \pm 0.24) \times 10^{-26}$ cm^3 s^{-1}. These annihilation rates are lower than, but close to the annihilation rates that are excluded by combined dwarf galaxy analyses [13] and collider searches [2]. Future combined dwarf galaxy analyses may be sensitive to this parameter space [81, 54, 70]. Once confirmed, measurements of the isotropic extragalactic background can yield further information on, e.g., the smallest halo mass [92].

It has been pointed out that bremsstrahlung will modify the gamma-ray spectra appreciably [47], and our tests find that they increase the inferred particle masses in the $b\bar{b}$ or $\tau^+ \tau^-$ channels. While the extended source is robustly detected, we caution that the shape of the rise and fall of the spectrum ($E^2 dN/dE$), as shown in Figs. 2.4 and 2.10, is highly model dependent.

When interpreting all of the GCE emission as astrophysical, we find stringent limits on dark matter annihilation, but they are highly model dependent. In this sense, the combined dwarf limits are still the most robust.

To explain the diffuse GCE emission with unresolved MSPs, we estimated (using the gamma rays from 47 Tuc as a reference) that there need to be about 3000 to 5000 MSPs within the ROI (1 kpc by 1 kpc box towards the GC). This is a large number compared to the typical number of MSPs in globular clusters but the total stellar content is also much larger in this region. We have also highlighted the possibility that multiple sources may contribute to the GCE.

While we have characterized some of the systematic uncertainty associated with modeling of the diffuse background, we emphasize that our treatment is far from exhaustive. Further multiwavelength study of the Milky Way's Galactic Center is essential to understanding

the nature of the numerous sources in this highly dense astrophysical region. Even so, the detection of the GCE source is fairly robust to differences in the background modeling, and though the extended emission in gamma rays studied here is consistent with a pure astrophysics interpretation, the extended emission's consistency in morphology, spectrum and flux with a dark matter annihilation interpretation remains extremely intriguing.

Chapter Acknowledgements

Chapter 3

Discovery of a New Galactic Center Excess Consistent with Upscattered Starlight

Kevork N. Abazajian, Nicolas Canac, Shunsaku Horiuchi, Manoj Kaplinghat, and Anna Kwa

Chapter Abstract

We present a new extended gamma ray excess detected with the Fermi Satellite Large Area Telescope toward the Galactic Center that traces the morphology of infrared starlight emission. Combined with its measured spectrum, this new extended source is approximately consistent with inverse Compton emission from a high-energy electron-positron population with energies up to about 10 GeV. Previously detected emissions tracing the 20 cm radio, interpreted as bremsstrahlung radiation, and the Galactic Center Extended emission tracing a spherical distribution and peaking at 2 GeV, are also detected. We show that the inverse

Compton and bremsstrahlung emissions are likely due to the same source of electrons and positrons. All three extended emissions may be explained within the framework of a model where the dark matter annihilates to leptons or a model with unresolved millisecond pulsars in the Galactic Center.

3.1   Introduction

The Fermi Gamma Ray Space Telescope Large Area Telescope (Fermi LAT) has observed with unprecedented detail the "heart of darkness" of our Galaxy: its gravitational center. The past few years have revealed that there are a large number of new point sources [93] as well as new diffuse emission [121]. In addition, a large extended source, the Galactic Center Extended (GCE), has been detected by a number of groups [66, 72, 74, 10, 50] and is robust to uncertainties in the diffuse emission foregrounds in the region [68, 7, 123, 41]. The high-energy radiative processes that produce gamma rays are often commensurate with production or acceleration of related relativistic charged particle cosmic rays. Astrophysical processes include diffusive shock acceleration, magnetic reconnection, "one-shot" acceleration across high-voltage electric fields, and many other possibilities. Another source that can produce both cosmic rays and gamma rays are the products from candidate dark matter particle annihilation or decay. The significance of the Galactic center as a bright source for dark matter annihilation photons and cosmic rays has been known for some time [29].

High-energy charged particles, deposited either from astrophysical sources or dark matter annihilation, experience various propagation and energy-loss processes in the Galactic Center region. There has been recent work discussing how bremsstrahlung and inverse Compton (IC) effects could alter the prompt spectra coming from dark matter annihilation [47, 82]. What we show here, for the first time, is that these separate components—prompt, bremsstrahlung and IC—can be separated with morphological as well as spectral information. In particular,

we report the discovery of a new extended component of the gamma-ray emission toward the Milky Way Galactic Center that is spectrally and morphologically consistent with a population of electron-positron ($e^{\pm}$) cosmic rays producing gamma rays by upscattering starlight through the IC process. Secondly, we confirm the presence of an emission consistent with bremsstrahlung radiation, and find that this emission can be produced by the same population of $e^{\pm}$ impinging on the high-density gas in the Galactic Center. Lastly, we confirm the presence of a GCE source (peaking around 2 GeV) that has a centrally-peaked morphology consistent with dark matter annihilation. We show that the IC, bremsstrahlung and GCE components could all have originated from the products of dark matter annihilation. This explanation is not unique in that an unresolved population of millisecond pulsars or two independent astrophysical sources could produce these signals.

3.2   Methods and Results

We use Fermi Tools version `v9r33` to study Fermi LAT data from August 2008 to June 2014 (approximately 70 months of data). We use Pass 7 rather than Pass 7 Reprocessed instrument response functions since the diffuse map associated with the latter have strong caveats for use with new extended sources. Our procedure is similar to those described in Ref. [7]. We simultaneously fit the amplitude and spectrum of point sources from the 2FGL catalog [93], plus four other point sources in the ROI, as described below, in our region of interest (ROI) $7° \times 7°$ around the GC centered at $b = 0, \ell = 0$. We use $0.2 - 100$ GeV photons in 30 logarithmically-spaced energy bins. To enhance spatial resolution, we use `ULTRACLEAN`-class photons binned in an Aitoff projection into pixels of $0.1° \times 0.1°$.

We include the 20 cm radio template as a tracer of gas to account for the bremsstrahlung emission as has been done previously [121, 89, 7]. To test the possibility of IC emission from starlight due to this same population of $e^{\pm}$, we use the 3.4 μm template for stellar light

from the WISE mission [119]. Among the templates tested, this had the least obscuration of stellar light in the ROI; the results from other templates studied are discussed later. Our goal in using the 3.4 μm template is to test whether the IC component's morphology might be approximated by it; we do not presume that this template is an exact morphological description of the putative IC emission. As an example, if the diffusion length of $e^{\pm}$ is significantly less than the ROI dimensions, then the IC emission will track the morphology of the $e^{\pm}$ source more.

We use a $14° \times 14°$ template because of the broad PSF of Fermi-LAT producing contributions outside of the ROI, particularly at low energies consistent with the IC photons. As in Ref. [7], we also include the New Diffuse (ND) map whose intensity increases with angle away from the GC, which was interpreted as accounting for additional gas not captured in the 20 cm map. We have optimized the morphology of the GCE excess and ND templates to their best-fit profiles, as in Ref. [7]. To optimize the GCE excess, we used templates of $\rho(r)^2$ projected along the line-of-sight with $\rho(r) \propto r^{-\gamma}(r+r_s)^{-(3-\gamma)}$ and found that $\gamma = 1$ provided the best-fit. The best-fit new diffuse template increases with projected distance from the Galactic Center, θ, as $\theta^{0.3}$. It is worth noting that our GCE template is somewhat less steep than found previously, $1.1 - 1.4$ for the inner slope of the density profile [7, 68, 50].

In our analysis, we include two previously dicovered point sources, 1FGL J1744.0-2931c and "bkgA" [121], and furthermore discover two new point sources, PS1 and PS2, at ℓ, b of $356.616°, 1.009°$ and $356.829°, -0.174°$ with large test statistic (TS) values of 168 and 140, respectively[1]. PS1 has a spectrum consistent with a Log-Parabola, is near numerous X-ray and radio sources including, e.g., 1RXS J173331.6-311522, and could be in the plane of the Galaxy or extragalactic. PS2 has a spectrum consistent with a power law, and is near the supernova remnant G356.8-00 and compact radio source G356.9+0.1 [105]. They are at the edge of our ROI, and our conclusions regarding the IC, bremsstrahlung and GCE sources

---

[1]TS $\equiv 2\Delta \ln \mathscr{L}$, where $\Delta \mathscr{L}$ is the difference of the best fit likelihood with and without the source. For point sources, a value of TS = 25 is detected at a significance of just over 4σ [93].

are not qualitatively affected by their inclusion. We choose to keep them in our models.

All the 4 extended sources (GCE, ND, IC, Bremsstrahlung) were given generic log-parabola spectral forms with four free parameters each. We detect the WISE 3.4 μm template at very high significance of TS = 197.0. The previously studied sources were also detected at high significance. The GCE was detected with TS = 207.5, bremsstrahlung was detected with TS = 97.2. These sources and best fit models are shown in Fig. 3.1, and the resulting residual spectra and best-fit log-parabola models are shown in Fig. 3.2.

In addition to the IC and Bremsstrahlung signatures of a population of high energy $e^\pm$, the 20 cm radio emission is also consistent with the synchrotron emission from the same population of electrons with correlated implications for the ionization and temperature of the molecular gas [121]. The fact that the bremsstrahlung emission traces the 20 cm (synchrotron) map indicates that the magnetic field is frozen into the gas. When we replaced the 20 cm map with a CO map, which contains dense molecular structures along the plane, the bremsstrahlung excess was not detected.

We again emphasize that we do not expect the WISE template to be an exact morphological description for the proposed IC emission from GCE-associated electrons. However, the WISE template's high TS value does indicate that it is indeed a reasonable approximation for the IC component. We tested two other templates for the IC component. With a 100 μm dust template map [108], we were able to detect essentially the same IC spectrum with almost the same TS value. This indicates that the IC emission traces a disky template (thicker than the bremsstrahlung emission) but that there are considerable uncertainties in determining the correct morphology due to the poor angular resolution at energies below 500 MeV. With a 2MASS J-band (1.2 μm) template [110], the significance of the IC detection was much lower (TS = 98.4); this is likely due to the large variable dust attentuation evident in the J-band map. For both , we observe the notable feature of the IC spectral cutoff at $\sim$1 GeV. This is a distinctive spectral feature of the IC excess that distinguishes it from the
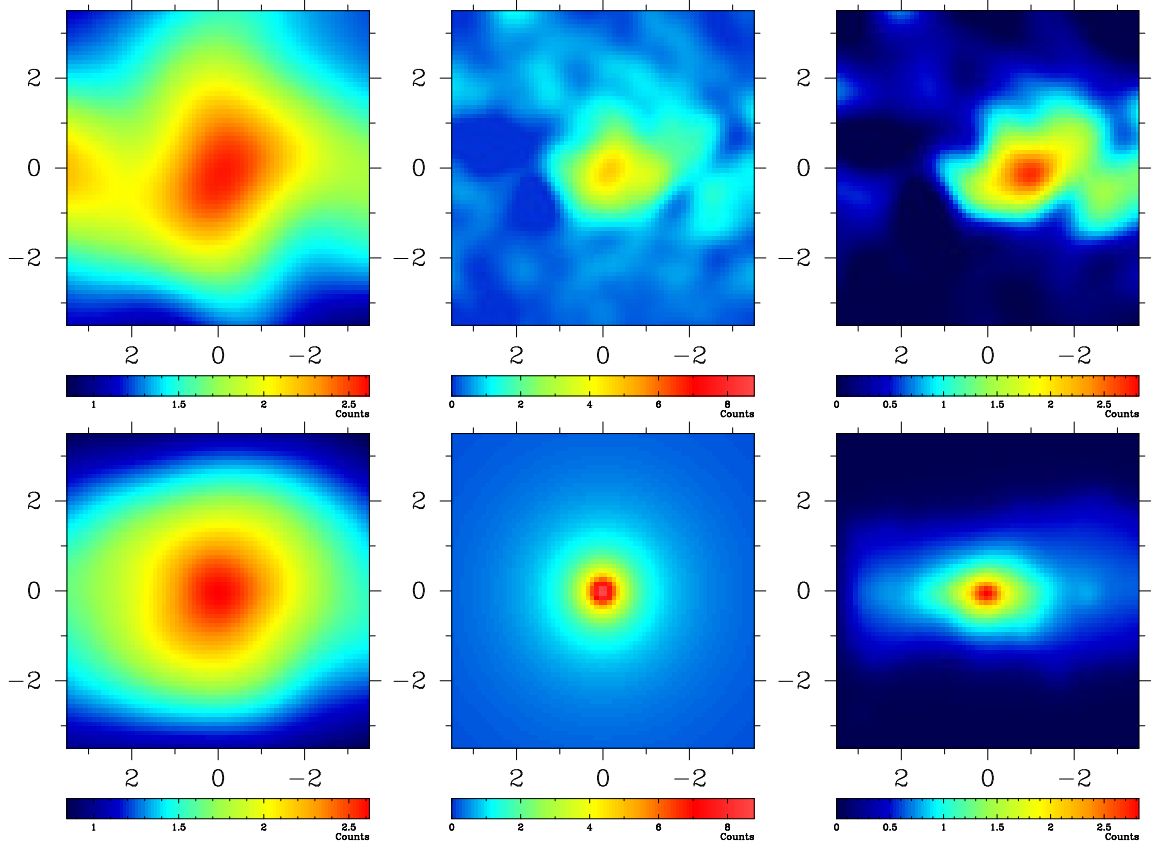
Figure 3.1: Shown in the left column are the residual photons (top) and best fit model (bottom) associated with the projected interstellar radiation field template in its peak intensity bin, 0.303 GeV $< E_\gamma <$ 0.372 GeV, where the residual map has been smoothed with a Gaussian of $\sigma = 0.9°$ (to roughly account for the point-spread function). The middle column shows the residual photons (top) and best fit model (bottom) associated with the projected dark matter density squared template in its peak intensity bin, 1.59 GeV $< E_\gamma <$ 1.95 GeV, where the residual map has been smoothed with a Gaussian of $\sigma = 0.4°$. The right column shows the residual photons (top) and best fit model (bottom) associated with the 20 cm radio map in the same energy bin and with the same smoothing as the middle row. Residual and model maps have the same color scale for each row. This analysis used `ULTRACLEAN`-class photons.

GALPROP-calculated IC emission contained within the diffuse background model.

To test the robustness of our results, we repeat our analysis using different diffuse backgrounds generated using the GALPROP code [1]. We tested two models in the extreme case where parameters were chosen with the intent to increase the IC emission predicted in the diffuse background, thus increasing the possibilty that some or all of the excess might be

43
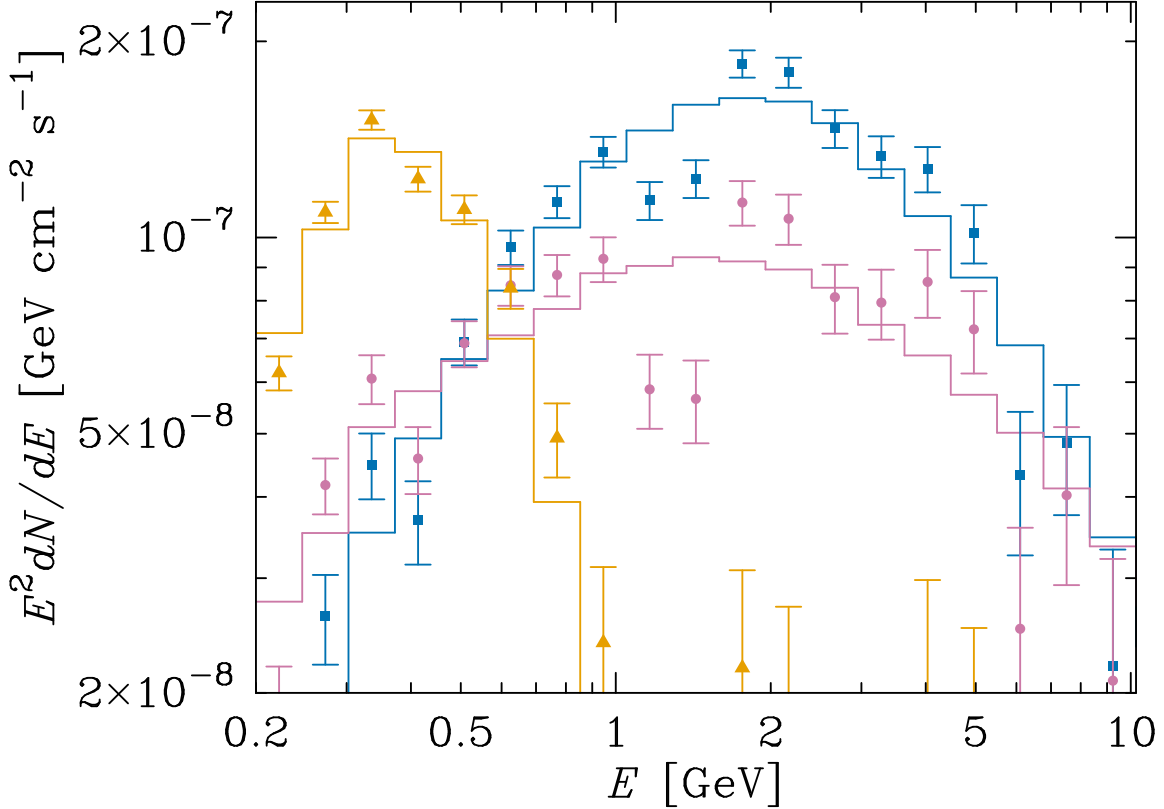
Figure 3.2: The residual spectra (points with errors) and best-fit model spectra for the projected interstellar radiation field (golden triangle), gas (pink circle), and dark matter density squared (blue square) templates. `ULTRACLEAN` class photons are used for this analysis.

absorbed into the background. For the first of these extreme cases, we chose a model with a very low diffusion parameter, which results in increased IC emission at lower energies. For the second extreme case we tested a model with a factor of 1.5 increase in optical and IR ISRF normalizations. We also tested two models with more standard parameters that were found by [41] to be good fits to the data in the inner galaxy. In all tests, the IC and GCE components were recovered with very similar spectra and uncertainties as when the Pass 7 model background was employed. The bremsstrahlung component was similar in most test cases; the only notable difference was that when employing a background model with extremely low diffusion coefficient, the bremsstrahlung spectrum did not show a cut-off as in Fig. 3.2, but it still had the same flux at GeV energies. These findings support our claim that the excesses are robust, and not an artifact of using the Pass 7 diffuse model. Inter-

ested readers may find the details of these diffuse background model checks in the following appendix.

We also test the dependence of our main results on the extended source templates included when modelling the data. We confirm that the spectra of the IC and GCE components remain more or less unchanged when the data is fit without the MG and ND components. We also substitute the HESS collaboration's $\sim$TeV residual map of the Galactic Ridge [19] in place of the 20 cm map used as the bremsstrahlung template, and find that the GCE and IC spectra again remain very consistent with the results shown in Fig. 3.2, while the HESS map spectrum has a slightly lower energy cutoff (around 1 GeV) than the 20 cm map spectrum (around 2–4 GeV) but with similar peak normalization. Details of these checks may also be found in the appendix.

3.3 Interpretation and Discussion

We discuss here how the detected IC emission is consistent with arising from the same population of $e^\pm$ as that producing the bremsstrahlung emission. In addition, we show that the GCE, IC, and bremsstrahlung emission can all arise from dark matter annihilation to leptons.

Apart from the dark matter interpretation [74], the GCE has been proposed to be emission from millisecond pulsars (MSPs) [4, 10], episodic hadronic [42], or episodic leptonic cosmic ray injection [97]. Pulsars have the right conditions to produce energetic $e^\pm$ cosmic rays [64] and hence, in principle, MSPs could explain all three excesses: the GCE excess due to the gamma-ray emission from their outer magnetosphere, and the IC and bremsstrahlung resulting from the $e^\pm$ that are produced along with gamma-rays in cascades [69]. Hadronic emission is less promising because it has trouble with the observed symmetry of the GCE .

The IC emission must arise from a leptonic channel, perhaps secondary $e^\pm$ produced due to hadronic interactions or a separate channel such as leptonic cosmic ray emission from star formation activity.

The fact that bremsstrahlung and the GCE spectrum could originate from a broken spectrum of $e^\pm$ resulting from dark matter annihilation has been discussed previously [86, 121]. Below we argue that the bremsstrahlung and IC spectra may naturally be related to the same $e^\pm$ population, which in turn could be connected to the origin of the GCE excess.

Let us consider a population of $e^\pm$ with energy E_c. The resulting IC photons have typical energies of $(E_c/m_e)^2 hc/(1~\mu\mathrm{m})$, where we have used the fact that the spectral energy distribution of the interstellar radiation field peaks around a micron. Assuming $E_c = 10$ GeV results in an IC spectrum that cuts off rapidly by 1-2 GeV. The bremsstrahlung spectrum for the same population is broader in energy and extends up to E_c. Both these predictions are qualitatively consistent with the spectra shown in Fig. 3.2. To test the consistency of the spectra with this simple picture further, we build a simplified model of diffusion and energy loss in the Galactic Center.

The $e^\pm$ in the products created by dark matter annihilation lose energy through three distinct process [48]: (1) IC, which leads to upscattering of the interstellar radiation field (ISRF) photons, (2) bremsstrahlung (Br) radiation off the gas, and (3) synchrotron radiation in the Galactic magnetic field. We focus on the first two components in this chapter. The differential flux of photons for these two components may be written as,

$$E\frac{dN_{\mathrm{IC,Br}}}{dE} = \int_{\mathrm{FOV}} \frac{d\Omega}{4\pi} \int_{\mathrm{LOS}} d\ell \int_{E_{\min}}^{m} dE_e \frac{dn_e}{dE_e} \frac{dP_{\mathrm{IC,Br}}}{dE} \tag{3.1}$$

where FOV and LOS indicate integration over the field-of-view and line-of-sight respectively, dP_{IC}/dE and dP_{Br}/dE are the differential power emitted per electron due to IC and bremsstrahlung processes. For bremsstrahlung, we include energy losses from atomic H and
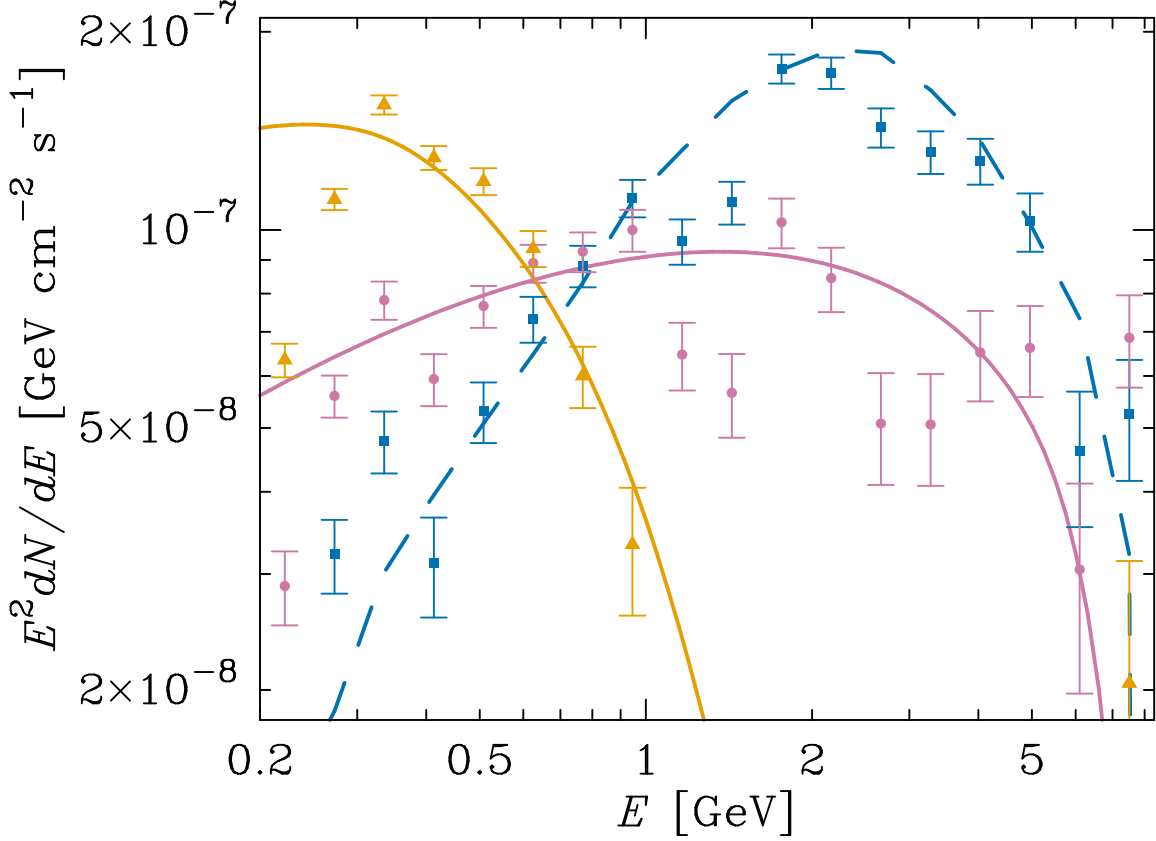
Figure 3.3: Shown here is an example 8 GeV dark matter annihilation model with equal branching to all charged leptons, $e^{\pm}, \mu^{\pm}, \tau^{\pm}$, with the residual spectra of the prompt GCE (blue square), IC (golden triangle), and bremsstrahlung (pink circle) sources. The blue (dashed) GCE spectrum is is determined by the particle mass and annihilation rate fit to the observations. The solid *predicted* resultant spectra for this annihilation channel's IC (golden) and bremsstrahlung (pink) cases are in solid lines. `ULTRACLEAN` class photons are used for this analysis.

He. To get the source energy distribution of electrons, positrons and gamma rays, we use the software PPPC4DMID [46]. The number density of electrons and positrons per unit energy, dn_e/dE_e, is computed after including diffusion and energy losses according to the prescriptions in Refs. [52, 47].

To propagate the $e^{\pm}$, we assume a spatially constant diffusion coefficient $K(E) = K_0 E^{\delta}$, with K_0 and δ set to the "MED" model [52] (often used for diffusion in the local neighboorhood). The diffusion process is largely unconstrained in the Galactic Center and variations away from the assumed parameters have significant effects on the magnitude and spatial profile of

the IC and Br signals. Also, the analytic description for diffusion does not allow for spatially-varying energy loss terms and we have assumed average values for the ISRF energy density and the gas density to create the model spectra for comparison. These choices, however, serve to illustrate our two main points that (a) the IC and bremsstrahlung spectrum could be due to the same lepton population, and (b) a single mechanism could explain the morphologies, strengths and spectra of the three distinct Galactic Center extended excesses.

For the average gas density and magnetic field strength, we assume $3\,\mathrm{cm}^{-3}$ and $3\,\mu\mathrm{G}$, which are reasonable given the large uncertainties at the Galactic Center [82]. We use the radiation density of ISRF photons included with GALPROP v50 [1, 98]. Since our FOV is ± 0.5 kpc of the Galactic Center, we use the value of the ISRF energy spectrum tabulated for $R = 0, Z = 0.25$ kpc in GALPROP v50 as the average over the region contributing to the IC flux.

Our final estimates for the IC and bremsstrahlung excesses are,

$$E\frac{dN_{\mathrm{IC,Br}}}{dE} = \frac{\mathrm{FOV}}{4\pi}\ell_{\mathrm{IC,Br}} \int_{E_{\mathrm{min}}}^{m} dE_e \left\langle \frac{dn_e}{dE_e} \right\rangle \left\langle \frac{dP_{\mathrm{IC,Br}}}{dE} \right\rangle$$

where $\langle dP_{\mathrm{IC,Br}}/dE \rangle$ are computed using the average ISRF and gas densities and $\langle dn_e/dE_e \rangle$ is averaged over the inner 0.5 kpc (in keeping with the small FOV). The factors ℓ_{IC} and ℓ_{Br} depend on the details of the deprojected ISRF and gas densities. For a consistent solution we expect them to be $O(\mathrm{kpc})$.

The GCE, IC and bremsstrahlung spectra in the case of a minimal "democratic" $e^{\pm} : \mu^{\pm} :$ $\tau^{\pm} = 1 : 1 : 1$ annihilation channel is shown in Fig. 3.3 for particle mass $m_\chi = 8$ GeV and annihilation cross section $\langle \sigma v \rangle = 3.6 \times 10^{-26}\,\mathrm{cm}^3\mathrm{s}^{-1}$. The best-fit dark matter mass when fitting to the GCE excess is closer to 7 GeV. In this model, the gamma rays from the $\tau^{\pm}$ dominate the prompt flux and explain the GCE excess. In Fig. 3.3, we have shown IC and

bremsstrahlung model spectra using $\ell_{\mathrm{Br}} = \ell_{\mathrm{IC}} = 1.3\,\mathrm{kpc}$. We caution the reader that no attempt has been made to fit to all three components simultaneously.

The value of the cross section used to create the spectra in Fig. 3.3 is ruled out by AMS-02 constraints on WIMP annihilation to leptonic channels [28]. However, the required cross section depends sensitively on the assumed density profile. For example, if we assume a scale radius (r_s) of 10 kpc and $\gamma = 1.2$ (keeping the local density unchanged at $0.3\,\mathrm{GeV/cm^3}$), the required cross section is a factor of 10 smaller. We have checked that such a profile is consistent with the expectation that the dark matter halo undergoes adiabatic contraction [36] due to the formation of the disk and bulge of stars. On the particle physics side, some of this tension may be relieved by considering annihilation through a vector mediator, which softens the final $e^{\pm}$ spectrum.

3.4   Conclusions

We have detected a new excess in gamma rays toward the Galactic Center that spatially traces starlight intensity. The spectrum of this new source is consistent with that produced by high energy electrons and positrons with energies up to about 10 GeV, upscattering starlight. The population of electrons and positrons required to produce such an inverse Compton emission would also produce bremsstrahlung radiation due to interactions with the dense gas at the Galactic Center. Further studies are required to examine the physical implications of this high energy electron population and perform more detailed modeling of the predicted IC excess morphology and spectrum. We detect a gamma-ray excess tracing 20 cm radio map and show that its flux spectrum is consistent in both shape and amplitude with bremsstrahlung radiation from the same population of electrons and positrons. We show that the Galactic Center extended excess that peaks around 2 GeV is also detected at high significance and that a dark matter model with annihilation to leptons may provide a

consistent explanation for all three excesses.

While this consistency with three excesses in terms of signal strengths, spectra and morphologies is remarkable, other astrophysical explanations exist that deserve detailed investigations. Infrared, radio and gamma ray data as incorporated in this work has allowed complicated high-energy emissions seen toward the Milky Way's Galactic Center to be disentangled, and this multiwavelength approach may help us to further elucidate the true origin of these excesses.

Chapter Acknowledgements

Chapter 4

Testing for cosmological evidence of new physics: neutrinos, the primordial power spectrum, and model dependence

Nicolas Canac, Grigor Aslanyan, Kevork N. Abazajian, Layne C. Price, and Richard Easther

Chapter Abstract

We test how neutrino parameter constraints and signals from combinations of CMB and LSS data sets depend on the assumed form of the primordial power spectrum (PPS) using Bayesian model selection. Significantly, all combinations tested, including recent high-precision local measurements of H_0 and cluster abundances, do not indicate a signal for massive neutrinos or extra relativistic degrees of freedom. For flexible PPS models with a

large, but fixed number of degrees of freedom, we find that limits on neutrino parameter constraints are robust when the location of features in the PPS are allowed to vary with scale, although the neutrino constraints are more sensitive to PPS features if they are known *a priori* to exist at fixed intervals in $\log k$. Although there is no preference for solely new neutrino physics from the data, in either neutrino mass or relativistic energy density, we find surprisingly strong evidence for the presence of features in the PPS when data from *Planck* 2015, SZ cluster counts, and recent high-precision local measurements of H_0 are used. This conclusion is significantly weakened when *Planck* is combined with matter power spectrum and BAO measurements. Due to the lack of consistency between inferences drawn from the different data combinations, instead of new physics in the PPS or neutrino sector, the tension between SZ cluster counts, *Planck* and H_0 measurements is likely an indication of unmodeled systematic bias that mimics PPS features.

4.1 Introduction

Cosmological observations have emerged as a stringent constraint on the total mass of neutrinos. Neutrino mass affects the cosmic microwave background (CMB) anisotropies in ΛCDM and even more greatly modifies the late time matter power spectrum measured in clustering observations. The CMB is sensitive to neutrino mass and effective neutrino number via the alteration of matter-radiation equality leading up to the decoupling of the CMB, and the alteration of the evolution of the neutrino anisotropic stress-energy tensor. Extra relativistic energy density modifies the acoustic peak scale to the photon-damping scale, making the CMB a sensitive measure of relativistic energy density above the photon density, often parameterized as $N_{\rm eff} \equiv (\rho_{\rm rad} - \rho_\gamma)/\rho_\nu$, where $\rho_{\rm rad}$, ρ_γ, and ρ_ν are the total energy density in relativistic species, photons, and active neutrinos, respectively.

Cosmological large scale structure (LSS) is also sensitive to the presence of massive neutrinos

and effective neutrino number N_{eff}. Baryon acoustic oscillations (BAO) are affected by the change of matter-radiation equality and commensurate change in expansion history. Measurements of LSS clustering, such as the power spectrum of galaxies, is a sensitive probe of neutrino properties, where clustering is suppressed below the neutrino free streaming scale due to a combination of the relativistic behavior of neutrinos at early times and their free-streaming suppression of late time growth. The sensitivity of galaxy clustering was highlighted some time ago (*e.g.*, [77]), and future probes can achieve very high precision (For a recent review, see Ref. [11]).

When combined with LSS observables, the complementary role of the CMB arises in removing degeneracies with other cosmological parameters through high-precision determination of their values. For example, the scalar perturbation amplitude A_s, tilt n_s and matter density Ω_m are each, to different degrees, degenerate with $\sum m_\nu$, but are determined to percent-level precision from Planck's 2015 CMB analysis [16]. In single-parameter extensions of ΛCDM where the sum of neutrino masses is left as a free parameter, the constraints on massive neutrinos are more than one order of magnitude tighter than from current kinematic laboratory constraints: $\sum m_\nu < 0.23$ eV (95%) from Planck 2015 (TT, lowP, lensing, BAO, JLA, H_0) [16], versus $\sum m_\nu \lesssim 6$ eV from ^{3}H β decay plus oscillations [94]. The latest Planck data (TT, TE, EE, SimLow, lensing) [18] has the tighter constraint of $\sum m_\nu < 0.14\text{eV}(95\%)$, but the HFI likelihood codes are not yet public. Here the sum of neutrino masses is defined as the sum of the individual mass eigenstates $\Sigma m_\nu \equiv m_1 + m_2 + m_3$ and does not depend on their hierarchical ordering near or above the mass degeneracy scale where $m_1 \approx m_2 \approx m_3$.

In the past several years, there have been indications that there is a tension between local measures of cosmological structure and expansion with that from the CMB at high redshift. One of the first strong indicators was from combinations of CMB and H_0 data with SPT SZ clusters from Hou et al. [76]. Combinations of cosmic shear lensing data from CFHTLenS also indicated a nonzero neutrino mass [26], as well as data from the Baryon Oscillation

Spectroscopic Survey (BOSS) constant mass (CMASS) luminous red galaxy sample [32]. With combinations of data sets between local and high redshift cosmology measures, there were a number of combinations that indicated degenerate neutrino masses or extra relativistic energy density could relieve this tension [120, 117, 25, 62, 103, 100]. Whether the evidence for strong tension and new neutrino physics from the low redshift measures is definitive has been called into question by several papers [115, 84, 16]. For example, weak lensing systematics has been shown to alleviate tension in that data set [88]. Generally, the low redshift data indicates a lower amplitude of fluctuations on relatively small scales, parameterized as σ_8, the rms over-density of fluctuations smoothed with a spherical window function of $8h^{-1}$ Mpc. Although there exist several different cluster abundance samples that indicate tension with the CMB [107, 15, 118, 106], we employ, as a representative measure, constraints on σ_8 vs Ω_m from Planck SZ Clusters, as described below [15, 25]. Additional tension is indicated in recent high-precision measures of the local expansion rate H_0, which has been proposed to potentially indicate extra relativistic energy density ($N_{\mathrm{eff}} > 3$) [102].

Future cosmological neutrino mass sensitivity will approach the minimum $\sum m_\nu \approx 60$ meV required by oscillations. Approaching high sensitivity in neutrino physics requires a careful analysis of the assumptions and model dependencies behind cosmological constraints, especially when cosmological constraints are becoming comparable with laboratory methods that have fewer model dependencies. Several model dependencies within cosmology are discussed in, *e.g.* Ref. [3]. In particular, the effects of massive neutrinos in large scale structure can be degenerate with deviations in the primordial power spectrum (PPS) arising from inflation. As a proof-of-concept, it has been shown that fine-tuning an arbitrary PPS could allow the CMB to mimic a zero neutrino mass universe despite it having a large neutrino density, when arbitrarily complicated PPS are allowed [79]. It is therefore natural to test the dependence of neutrino parameter constraints on the assumed shape of the PPS. Testing PPS freedom was previously done in Refs. [51, 61, 53]. Those works fixed positions for features in the primordial power spectrum, placing prior information on the positions where features would

be expected. In this paper, we further test this methodology by relaxing the assumption for fixed features, employing the Bayesian model selection methods of Ref [22, 6], where the location of possible PPS features is not imposed *a priori*—given that there is no such prior information. This gives a complementary test for the preferred amount of structure in the PPS explicitly allowed by the data.

In addition, we go beyond previous work in exploring local universe tension data sets from SZ cluster abundances and recent high-precision measures of H_0. In our analysis, we employ CMB data from the 2015 Planck results [16]. We employ the most recent large-volume galaxy survey LSS data from the clustering of Luminous Red Galaxies from the Sloan Digital Sky Survey [101], as well as the WiggleZ Dark Energy Survey [95]. We also use the most recent measures of the Baryon Acoustic Oscillation (BAO) scale from the six-degree-Field Galaxy Survey (6dFGS) [31], from the SDSS Main Galaxy Sample (SDSS-MGS) [104], and from the Baryon Oscillation Spectroscopic Survey data release 11 (BOSS DR11), from both the LOWZ and CMASS samples [20], which provide robust complementary constraints on the cosmological parameters, including neutrinos. In order to claim strong evidence for new physics from the combined analysis of these tension data sets, it is necessary that different probes of the same cosmological signals, *e.g.*, expansion history or growth rate, provide comparable statistical evidences for the same extensions to ΛCDM. In contrast, if different models are favored with wildly variable confidences, then this provides some evidence for unmodeled bias in the probes themselves. In light of this, here we aim to test for the evidence of novel signals in the neutrino sector or the primordial spectrum.

4.2 Method

In this section, we describe the cosmological models analyzed, with a particular focus on our method for reconstructing the PPS. We also give the priors we choose for the parameters in

our models and discuss the use of Bayesian evidence and posterior probabilities for performing model selection and parameter estimation.

In the following analysis, the likelihood calculations and PPS reconstruction are performed using the publicly available code COSMO++ [21]. The CMB power spectra and matter power spectrum are calculated using the CLASS package [85, 35]. The parameter space sampling and Bayesian evidence calculation is implemented with the publicly available multimodal nested sampling code MULTINEST [57, 58, 59]. Finally, the resulting chains are analyzed and plotted using the GETDIST Python package.

4.2.1   Non-power-law primordial power spectrum

Our goal is to examine how measures of neutrino parameters change when we relax the assumption that the PPS adheres to a simple power-law form. In particular, we want to test how sensitive the neutrino parameters are to the prior that is chosen for the shape of the PPS. The approach that we adopt for reconstructing the PPS is a variation of the "knot-spline" method as described in [113, 22, 6]. Similar methods have been used to study a free-form primordial spectrum in Refs. [109, 39, 40, 116, 38, 96, 33, 114, 51, 17, 53, 99].

The algorithm for generating the spectrum is summarized as follows:

1. Fix $k_{\mathrm{min}} = 10^{-6}\,\mathrm{Mpc}^{-1}$ and $k_{\mathrm{max}} = 10.0\,\mathrm{Mpc}^{-1}$, but allow their amplitudes A_{min} and A_{max} to vary.

2. Add n knots with uniform priors on $\log k$, in the range $\log k_{\mathrm{min}} < \log k_i < \log k_{\mathrm{max}}$ and a uniform prior on A_i, in the range $-2 < A_i < 4$, where $A_i \equiv \log(10^{10}\Delta_\zeta^2(k_i))$, where Δ_ζ^2 is the dimensionless PPS of curvature perturbations and $i = 1, 2, ..., n$. We ensure that the knots are ordered so that $k_{i-1} \leq k_i$, and the number of knots n is varied between 1 and 5.
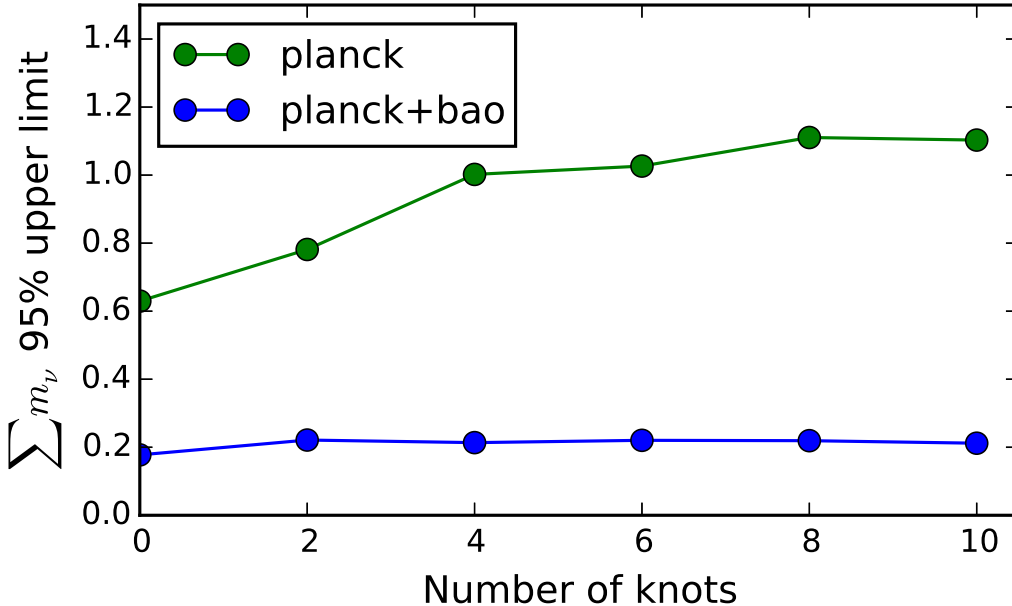
Figure 4.1: Shown are the 95% CI upper limits on $\sum m_\nu$ for fixed knot locations when only Planck15 data is included and when Planck15+BAO are included.

3. Interpolate between the endpoints and the n ordered knots using a linear spline. The interpolation is performed in logarithmic space for both k and Δ_ζ^2.

We use uniform priors on the locations of knots in $\log k$ and their amplitudes. Knots with arbitrary locations in k-space are able to capture both local features, such as a step-like feature, and more gradual changes like a large-scale exponential suppression, as well as shapes like a cut-off spectrum. With no knots, the PPS is specified by two parameters, the amplitudes of the endpoints k_{min} and k_{max}. In this case, the PPS is equivalent to the standard power-law PPS in ΛCDM, providing for an easy comparison between the two models. Each additional knot yields two degrees of freedom corresponding to the location of the knot k_i and its amplitude A_i. In total, there are $2n + 2$ free parameters associated with our PPS model, where n is the number of knots. An advantage of allowing the knot location to vary is that it provides some basic protection against the look-elsewhere effect or multiple comparisons problem, since the knot is free to move over the global range of k, unlike in reconstructions
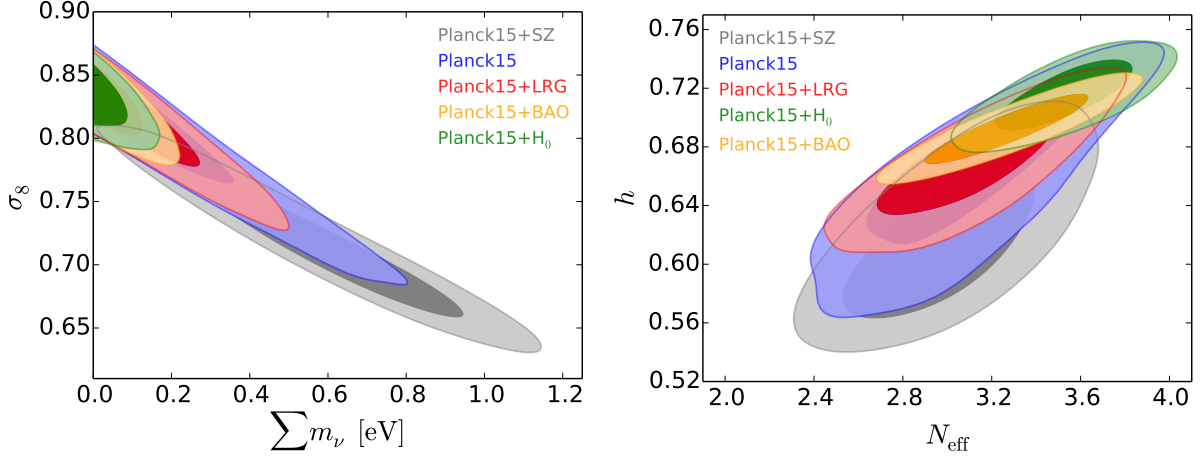
Figure 4.2: *(Left)* The two-dimensional posterior distribution showing the 68% and 95% CI allowed regions in the $\sigma_8 - \sum m_\nu$ plane for 0 knots and $\sum m_\nu$ free for various combinations of data. *(Right)* The same but for $N_{\rm eff}$ in the $h - N_{\rm eff}$ plane.

in which the knot locations are fixed. The broad ranges used for $k_{\rm knot}$ and $A_{\rm knot}$ allow for possible features at any measurable scale.

4.2.2 Model, priors, and Bayesian evidence

We choose uniform priors for all of our cosmological parameters, including the standard parameters $\Omega_b h^2$, $\Omega_c h^2$, h, and τ, as well as the sum of the neutrino masses $\sum m_\nu$ and the effective number of relativistic degrees of freedom $N_{\rm eff}$. In addition, for our knot-spline reconstruction of the PPS there are two parameters associated with each knot, $\log_{10} k_{\rm knot}$ and $\log(10^{10} \Delta^2_{\rm knot})$, and two additional parameters associated with the amplitudes of the fixed endpoints. The ranges for these priors are shown in Table 4.1.

To evaluate the statistical significance of a model $\mathscr{M}$, we use the posterior probability $P(\mathscr{M} \,|\, \text{Data})$. For two models $\mathscr{M}_i$ and $\mathscr{M}_j$ with the same prior probability, the evidence ratio or Bayes factor is given by

$$B_{ij} = \frac{P(\text{Data} \,|\, \mathscr{M}_i)}{P(\text{Data} \,|\, \mathscr{M}_j)},\tag{4.1}$$
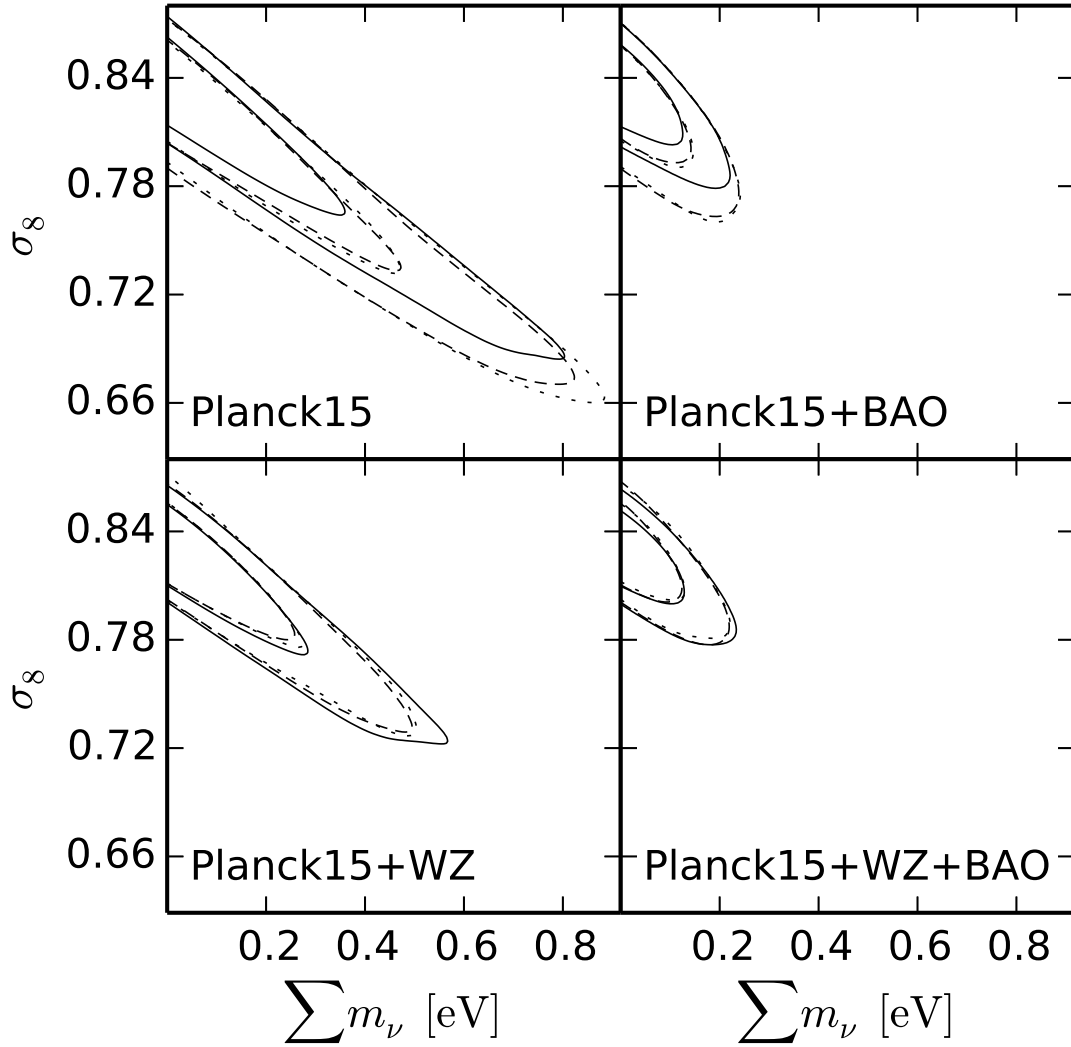
Figure 4.3: Two-dimensional posterior distributions in the $\sigma_8 - \sum m_\nu$ plane for 0 knots (solid line), 1 knot (dashed line), and 2 knots (dotted line) for various combinations of data sets. Numbers of knots beyond 2 do not result in any significant change and so are not shown.

Parameter	Prior	Parameter	Prior
$\Omega_b h^2$	$[0.020, 0.025]$	$\sum m_\nu$	$[0.001, 3.0]$
$\Omega_c h^2$	$[0.10, 0.14]$	N_{eff}	$[2.0, 5.0]$
h	$[0.55, 0.80]$	$\log_{10} k_{\text{knot}}$	$[-6, 1]$
τ	$[0.04, 0.12]$	$\log(10^{10} \Delta^2_{\text{knot}})$	$[-2, 4]$

Table 4.1: Ranges for uniform priors for cosmological parameters.

where the Bayesian evidence or marginalized likelihood is

$$Z_i(D) \equiv P(\text{Data} \,|\, \mathscr{M}_i) = \int P(\theta \,|\, \mathscr{M}_i) \, \mathscr{L}(\text{Data} \,|\, \theta) d\theta \tag{4.2}$$

for the model parameters θ. Here, $\mathscr{L}(\text{Data} \,|\, \theta)$ is the data-likelihood and $P(\theta \,|\, \mathscr{M}_i)$ is the parameter prior probability. When the prior probability for the models is assumed to be equal as is common convention, the Bayes' factor directly measures the posterior model odds. Given the absence of a well-motivated model predicting features at a particular scale, we allow for a wide range of values when specifying potential features in the PPS at fixed number of degrees of freedom in our parameterization. In general, the integral in equation (4.2) is numerically challenging but can be computed using multimodal nested sampling, for example.

Evidence ratios can be interpreted qualitatively using the Jeffreys' scale [78] or a more conservative "cosmology scale" [71], summarized in Table 4.2. Bayesian model selection is a generally conservative approach, as it integrates over the entirety of parameter space and yields a global estimate of how well a model fits the data. The Bayes factor therefore penalizes those complex models with many free parameters that yield a high value for the likelihood only within some small sub-region of the overall parameter space. A model with more parameters must yield a significant improvement in likelihood over a sufficiently large volume of parameter space in order to yield posterior odds that support the more complex model.
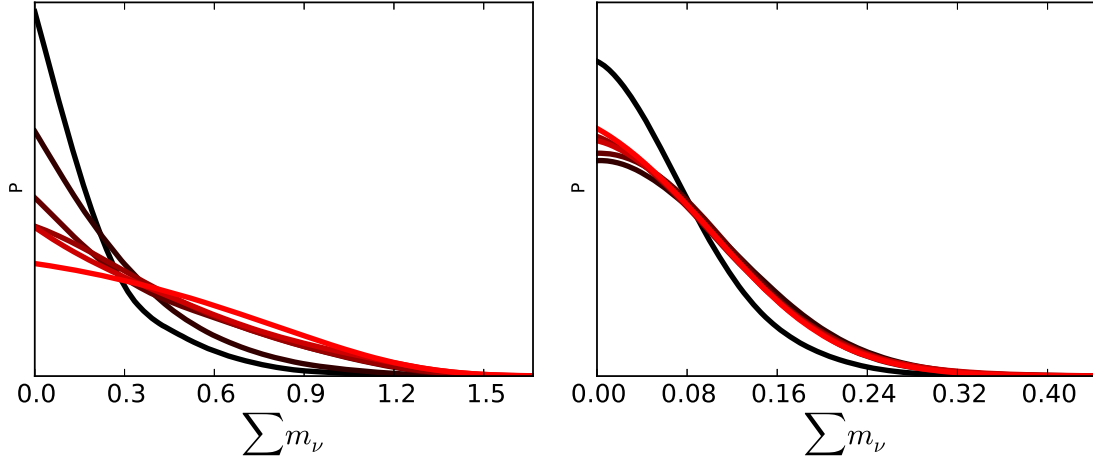
Figure 4.4: One-dimensional posterior distributions for $\sum m_\nu$ for (*left*) Planck15 only and (*right*) Planck15+BAO for the case of fixed knots. The color of line from dark to light represents increasing numbers of knots from 0 to 10 in intervals of 2.

log (*Posterior Odds*)	Jeffreys Scale	Cosmology Scale
0.0 to 1.0	Not worth more than a bare mention	
1.0 to 2.5	Substantial	Weak
2.5 to 5.0	Strong	Significant
> 5	Decisive	Strong

Table 4.2: Rough guideline for Bayesian evidence interpretation with the Jeffreys scale [78] and the more conservative "cosmology scale" from Ref. [71].
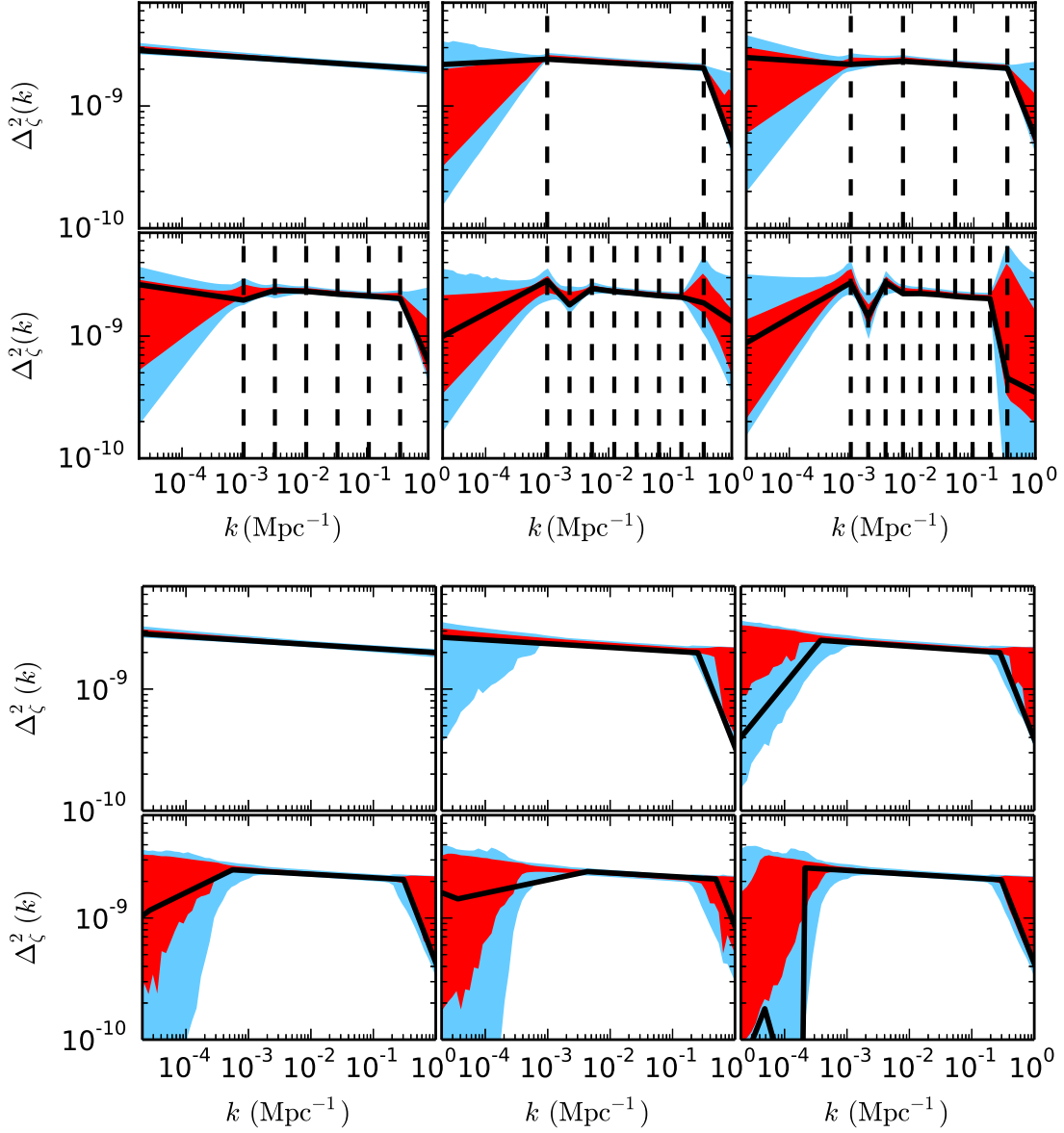
Figure 4.5: Shown *(top)* are the PPS for the case where the knot locations are fixed and only the amplitudes are allowed to vary using Planck15 and allowing $\sum m_\nu$ to vary. The black line shows the best fit PPS, and the red and blue regions correspond to the 68% and 95% CI regions. We see similar reconstructed power spectra when BAO is included *(not shown)*. For comparison, we show *(bottom)* the same case but now allowing the knot location to vary for 0 to 5 knots, so that the number of degrees of freedom between corresponding panels in the top and bottom figure are equal.

	Planck15			Planck15+BAO	
DOF	$\Delta \ln(Z)$ Free	$\Delta \ln(Z)$ Fixed	DOF	$\Delta \ln(Z)$ Free	$\Delta \ln(Z)$ Fixed
2	1.26	1.15	2	1.25	1.24
4	1.15	-5.79	4	1.2	-6.52
6	1.48	-13.03	6	1.42	-13.5
8	0.81	-20.33	8	1.07	-18.74
10	0.47	-21.59	10	1.21	-22.47

Table 4.3: Comparison of $\Delta \ln(Z)$ values relative to the 0 knot case (ΛCDM) for free-form PPS models with knot position in $\log_{10} k$ either free or fixed. For all cases, $\sum m_\nu$ is also free. The number of knots for each case is such that the number of additional degrees of freedom is equal in each row. For example, two additional degrees of freedom in the PPS corresponds to one knot in the free case (location and amplitude) and two knots in the fixed case (amplitude of each knot).

Data	No knots	1 knot	2 knots	3 knots	4 knots	5 knots
Planck15	0.63	0.66	0.71	0.64	0.71	0.67
Planck15+BAO	0.18	0.19	0.19	0.18	0.20	0.24
Planck15+WZ	0.44	0.40	0.40	0.39	0.43	0.37
Planck15+LRG	0.40	0.40	0.43	0.39	0.39	0.38
Planck15+H_0	0.13	0.15	0.15	0.18	0.15	0.18
Planck15+WZ+BAO	0.18	0.18	0.18	0.17	0.17	0.17
Planck15+LRG+BAO	0.17	0.16	0.17	0.17	0.16	0.22
P15+LRG+BAO+H_0	0.14	0.13	0.13	0.16	0.17	0.13
Planck15+SZ+H_0	0.23	0.23	0.23	0.24	0.23	0.24
Planck15+SZ	$0.60^{+0.22}_{-0.23}$	$0.52^{+0.22}_{-0.24}$	$0.52^{+0.22}_{-0.23}$	$0.53^{+0.21}_{-0.23}$	$0.49^{+0.20}_{-0.23}$	$0.49^{+0.20}_{-0.22}$

Table 4.4: 95% CI upper limits on $\sum m_\nu$ in eV for various combinations of data and numbers of knots for the model cases where $\sum m_\nu$ is allowed to vary in addition to the standard cosmological parameters and knots with k and amplitude freedom in position. The 68% CI constraints are also shown in the bottom row for the tension data set.

4.2.3   Data sets

We use measurements of the CMB, the matter power spectrum, BAO, SZ cluster counts, and Hubble constant H_0, which we describe in detail below. Likelihood modules for each of these data sets have been written for use with COSMO++.

Cosmic Microwave Background.—   For all the runs performed in this analysis, we use the CMB measurements from the Planck 2015 data release [14]. Although better constraints are provided by the latest intermediate results from Planck using low-ℓ HFI polarization [18], the data is not currently public. We use the interface provided by COSMO++ to include the Planck 2015 likelihood code and use the full Planck CMB temperature power spectrum at multipoles $2 \leq \ell \leq 2500$ along with the Planck low-ℓ polarization likelihood in the range $2 \leq \ell \leq 29$. This combination of data is generally referred to as Planck TT+lowP. In this paper, we will refer to this combination of data as "Planck15."

Matter Power Spectrum.—   In addition to CMB data, we also include power spectra measurements using two different data sets. The first data set comes from the SDSS Data Release 7 [8]. We use the most recent measure of the power spectrum of the reconstructed halo density field derived from a sample of $110,576$ LRGs in Reid et al. [101]. As in the original analysis, we include modes up to an upper bound of $k_{\mathrm{max}} = 0.2\,h\,\mathrm{Mpc}^{-1}$, above which uncertainties in nonlinear corrections to the matter power spectrum become significant, and down to a lower bound of $k_{\mathrm{min}} = 0.02\,h\,\mathrm{Mpc}^{-1}$, which is limited by the survey volume. We have rewritten the original Reid et al. likelihood code in C++ in order to interface with COSMO++. As in the original code, we include the effects on the linear power spectrum due to BAO damping, non-linear structure formation, and halo bias. We model each of these corrections identically as in the original code, with the one difference being that we are using an updated version of HALOFIT [112, 34]. The fiducial model files have also been updated

to include the effects of this new version of HALOFIT. We will use the shorthand "LRG" to refer to this set of data.

The second data set that we use for the matter power spectrum comes from the WiggleZ Dark Energy Survey, which provides a measurement of the matter power spectrum at redshifts $z = 0.22$, $z = 0.41$, $z = 0.60$, and $z = 0.78$ [95]. In our analysis, we include only modes that satisfy $0.02\,h\,\mathrm{Mpc}^{-1} < k < 0.2\,h\,\mathrm{Mpc}^{-1}$, as is done for the LRG data. Again, we have rewritten the WiggleZ likelihood code in C++ for use with COSMO++ and compared the sampling results to those obtained with MONTEPYTHON [23] to verify its accuracy. In this paper, we will use "WZ" to refer to this data set.

Baryon Acoustic Oscillations.— We have also included BAO data from the 6dFGS [31], from SDSS-MGS [104], and from BOSS Data Release 11, from both the LOWZ and CMASS samples [20]. We note that in cases where we use both LRG and BAO data, we omit the SDSS-MGS BAO data set in order to avoid double counting of information. For cases which do not include LRG, all four data sets are used when incorporating BAO measurements. From here on, we will refer to this data set simply as "BAO."

SZ Cluster Counts.— In addition, we include information from the detection of 189 clusters by *Planck* via the Sunyaev-Zeldovich effect [15]. Cosmological constraints were deduced in the $\sigma_8 - \Omega_m$ plane, which was found to be $\sigma_8(\Omega_M/0.27)^{0.3} = 0.764 \pm 0.025$ for the case where the hydrostatic bias $1 - b$ was allowed to vary in the range $[0.7, 1.0]$. The inclusion of this data will be referred to as "SZ."

Hubble Constant.— Finally, we include recent high-precision measures of the local Hubble expansion from the Hubble Space Telescope observations of Cepheid variables. This data was used to measure the local value of the Hubble Constant to 2.4%, as $H_0 = 73.02 \pm$
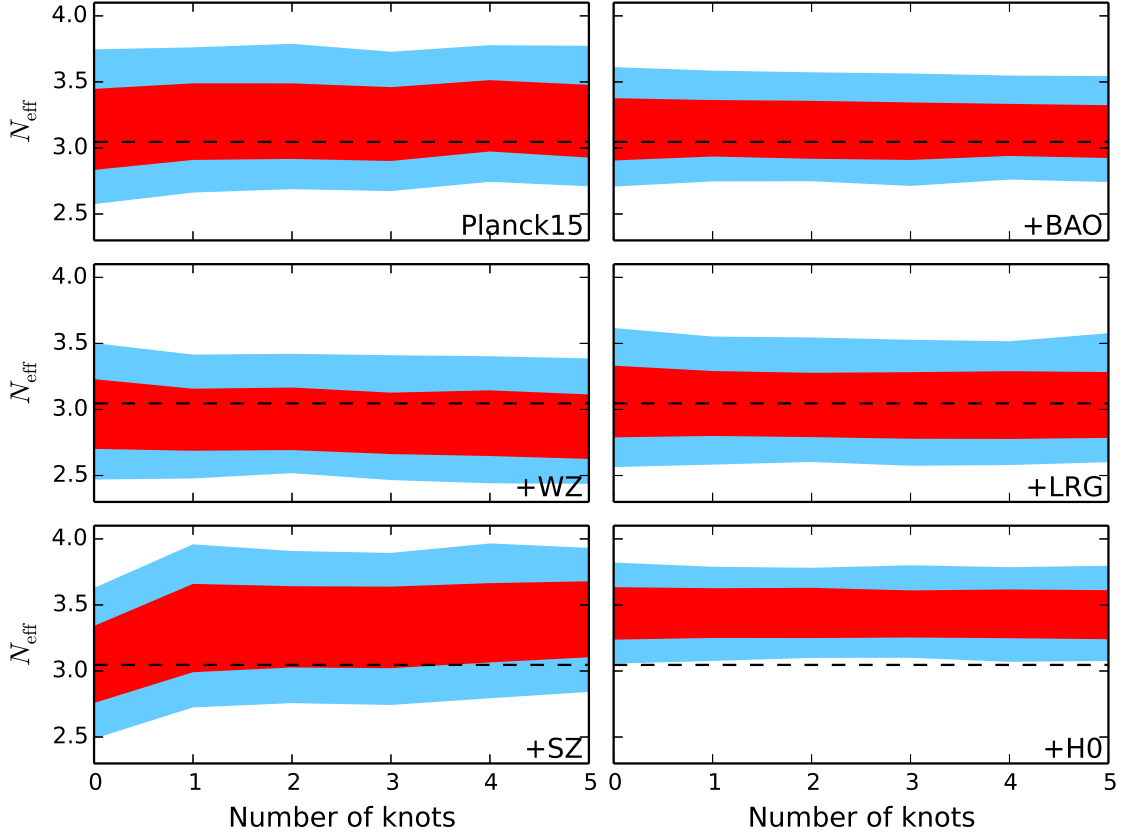
Figure 4.6: 68% and 95% CI constraints on N_{eff} for models with N_{eff} allowed to vary and PPS reconstruction with knot location free. The data sets used are indicated in each panel (Planck15 is implicitly included in each panel).

$1.79 \, \text{km} \, \text{s}^{-1} \, \text{Mpc}^{-1}$ [102]. This measurement will be referred to as "H_0." There are previous assessments of the local Hubble expansion that prefer lower values of H_0 [55]. We choose the determination from Reiss et al. [102] because it addresses much of the issues raised in Efstathiou [55], and is the highest precision measure of H_0 thus far. This measure is also of interest since it indicates tension at low redshift, potentially commensurately with the cluster samples. We include the measure of H_0 to test what it indicates for ΛCDM in combination with Planck and cluster data.
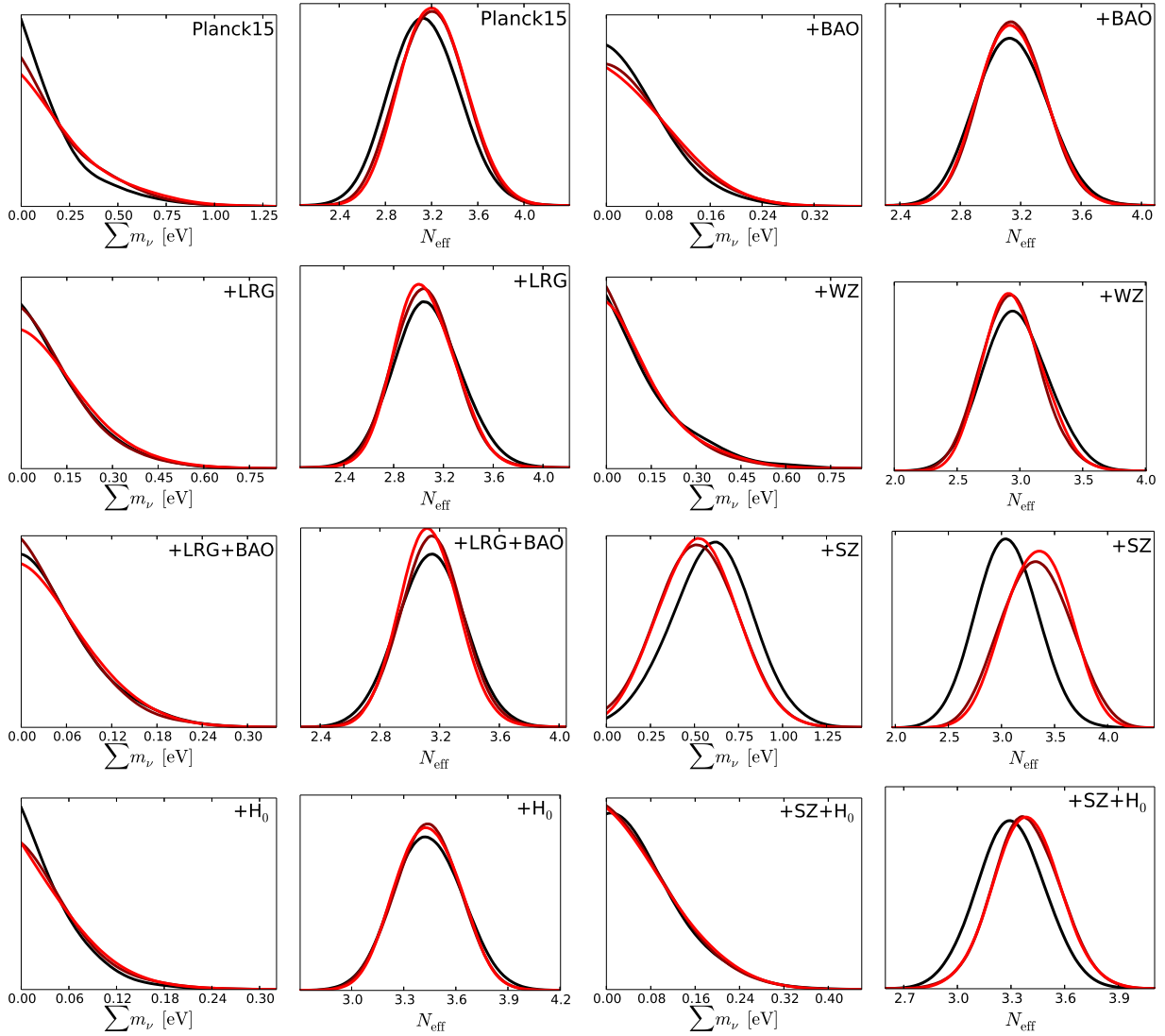
Figure 4.7: One-dimensional posterior distributions for $\sum m_\nu$ and N_{eff}. The colors of the contours from darkest to lightest indicate increasing number of knots in the PPS from 0 to 2 knots. Higher numbers of knots do not lead to significant changes. All cases shown are for models where the knot location in k is a free parameter.

4.3   Results and Discussion

Neutrino masses and N_{eff} with movable-knot PPS.—   In Table 4.4, we report the 95%
credible interval (CI) upper limits on the sum of the neutrino masses for zero to five knots for
various combinations of data sets. The limits for the case with zero knots are consistent with
previous work examining cosmological neutrino mass limits [49]. The last row of Table 4.4
shows the 68% CI constraints on $\sum m_\nu$ when SZ is included along with Planck15. This
shows a preference for non-zero $\sum m_\nu$, indicating some tension with the other data sets in
this analysis. For each of these cases, $\sum m_\nu$ is allowed to vary in addition to the other
standard cosmological parameters, along with the knot locations and amplitudes. When the
knot location is allowed to vary freely, the constraints on $\sum m_\nu$ show no dependence on the
number of knots in our Monte Carlo analysis. Therefore, for reconstructions of this form,
constraints on $\sum m_\nu$ appear to be robust to changes in the shape of the PPS.

Furthermore, our most stringent limit achieved using the combination of data sets Planck15+
LRG+BAO+H$_0$ of $\sum m_\nu \lesssim 0.13\,\text{eV}$ with one interior knot is comparable to the constraint
obtained with the ΛCDM spectrum (matching the same analysis in Ref. [63]). This is be-
ginning to approach the minimum allowed value for the inverted neutrino mass hierarchy
of $\sum m_\nu \sim 0.1\,\text{eV}$ and suggests that future precision measurements could distinguish be-
tween the two possibilities for the neutrino mass hierarchy. Joint constraints on σ_8, h, N_{eff},
and $\sum m_\nu$ shown in Fig. 4.2, illustrating how neutrino constraints become tighter with the
inclusion of additional data sets and which data most significantly impact the constraints.
We find that inclusion of the BAO data provides the most significant improvement in the
limit on the sum of neutrino masses due to the complementarity of BAO in constraining
Ω_m, which is highly degenerate with $\sum m_\nu$. The change in the posterior distributions for
varying numbers of knots and combinations of data sets are shown in Fig. 4.3, demonstrating
again the fact that allowing for additional freedom in the PPS does not significantly impact
neutrino parameter constraints. Knots beyond two are not shown as they do not change the

posterior distribution in a noticeable manner.

Table 4.5 shows the derived constraints on N_{eff} for zero to five knots for various combinations of data sets. In these cases, N_{eff} is allowed to vary along with the other standard cosmological parameters, along with the PPS knot locations and amplitudes. As with $\sum m_\nu$, constraints on N_{eff} also appear to be robust to a relaxation of the assumption that the PPS adheres to a power-law shape. In all cases in which H_0 is included, the best fit value for N_{eff} is observed to shift up, such that the standard value of 3.046 lies just outside the 95% allowed region for the majority of cases. Limits on N_{eff} are shown in Fig. 4.6. The dependence of the one-dimensional posterior distributions for $\sum m_\nu$ and N_{eff} are shown in Fig. 4.7. As mentioned, very little change is present when going from 0 to 2 knots. Beyond two knots, there is no discernible change, and so only cases up to 2 knots are shown.

Comparing fixed and movable-knot PPS.— To test how differences in methods for reconstructing the PPS affect derived neutrino parameter constraints, we perform several runs in which we fix the position of the knots, in a similar manner to the method used in Ref. [53]. Fig. 4.4 shows how the posterior distribution of $\sum m_\nu$ changes in the case where the position of knots are fixed and only the amplitudes are allowed to vary. For these cases, we follow a similar procedure to that described above for our "knot-spline" reconstruction, with the exception that the position of the knots are fixed in k-space. We perform runs with 0, 2, 4, 6, 8, and 10 knots, with locations indicated by the vertical dotted lines in Fig. 4.5.

For the case where only Planck15 is included, the posterior distribution of $\sum m_\nu$ varies considerably. This contrasts with our reconstruction in which the knot location is allowed to vary, indicating that the neutrino parameter constraints are sensitive to the prior on the allowed shape of the PPS. However, when information from LSS is included, in this case in the form of BAO data, the degree of change is significantly less. This is not surprising given the fact that LSS is expected to be a much more sensitive probe of neutrino mass than CMB

measurements alone. The 95% upper limits on $\sum m_\nu$ are shown in Fig. 4.1, illustrating this difference. The PPS for our fixed-location knots are shown in Fig. 4.5. These figures indicate more of a preference for features in the PPS relative to the reconstruction method in which the knot locations are allowed to vary freely.

In Fig. 4.9, we show the reconstructed PPS for cosmological models with different number of knots for Planck15 combined with various combinations of LRG, BAO, SZ, and H_0 data sets. We find no significant features in the PPS using Planck15 with any combination of LRG, WZ, and BAO data. There may be some evidence for features when using the tension data sets, SZ and H_0. We discuss this in more detail later in this paper. The black lines represent the most likely power spectra. These all tend to recover the standard power-law form for the PPS at small scales $k \gtrsim 10^{-3} \, \mathrm{Mpc}^{-1}$. At larger scales $k \lesssim 10^{-3} \, \mathrm{Mpc}^{-1}$, the best fit power spectra for models with non-zero numbers of knots tend to indicate a suppression of power at large scales due to the well-known low C_ℓ at low ℓ in the CMB (see, *e.g.* Ref. [22]). Note that when allowing the knots to freely vary, they accumulate in the cosmic variance dominated region, so that functions with a fixed amount of variability will prefer to fit large scale features preferably than small scale ones. Since we do not have *a priori* knowledge of the position of features in the PPS, we allow the knot location to vary. Furthermore, relaxing the position of the features protects against the look-elsewhere effect or multiple comparisons problem, since the knot is free to move over the global range of k.

Table 4.3 shows the $\Delta \ln(Z)$ values for the free and fixed-knot location PPS reconstructions described above with $\sum m_\nu$ free. In most cases, particularly for DOF ≥ 4, Bayesian evidence strongly prefers the reconstruction in which the knot location is free over models with knots fixed at the positions shown in Fig. 4.5. This indicates that a simple power-law fit over the approximate range $10^{-3} \, \mathrm{Mpc}^{-1} < k < 1 \, \mathrm{Mpc}^{-1}$ provides a significantly better fit than the hint of features seen in the PPS for fixed knot positions.

Data	No knots	1 knot	2 knots	3 knots	4 knots	5 knots
Planck15	$3.14^{+0.31}_{-0.31}$	$3.20^{+0.29}_{-0.29}$	$3.22^{+0.27}_{-0.30}$	$3.19^{+0.27}_{-0.29}$	$3.25^{+0.26}_{-0.28}$	$3.22^{+0.26}_{-0.29}$
Planck15+BAO	$3.14^{+0.24}_{-0.24}$	$3.15^{+0.21}_{-0.21}$	$3.15^{+0.21}_{-0.23}$	$3.14^{+0.21}_{-0.23}$	$3.14^{+0.20}_{-0.20}$	$3.14^{+0.19}_{-0.21}$
Planck15+WZ	$2.97^{+0.26}_{-0.27}$	$2.93^{+0.23}_{-0.24}$	$2.95^{+0.22}_{-0.25}$	$2.91^{+0.22}_{-0.25}$	$2.91^{+0.23}_{-0.27}$	$2.90^{+0.22}_{-0.27}$
Planck15+LRG	$3.07^{+0.26}_{-0.28}$	$3.05^{+0.24}_{-0.25}$	$3.05^{+0.23}_{-0.26}$	$3.04^{+0.24}_{-0.26}$	$3.04^{+0.25}_{-0.26}$	$3.05^{+0.23}_{-0.27}$
Planck15+H_0	$3.44^{+0.19}_{-0.20}$	$3.44^{+0.19}_{-0.19}$	$3.44^{+0.19}_{-0.19}$	$3.44^{+0.17}_{-0.19}$	$3.43^{+0.19}_{-0.18}$	$3.43^{+0.19}_{-0.18}$
Planck15+WZ+BAO	$3.01^{+0.21}_{-0.20}$	$3.02^{+0.19}_{-0.22}$	$3.01^{+0.18}_{-0.19}$	$3.00^{+0.19}_{-0.19}$	$3.01^{+0.18}_{-0.18}$	$3.01^{+0.19}_{-0.19}$
Planck15+LRG+BAO	$3.14^{+0.23}_{-0.23}$	$3.15^{+0.20}_{-0.21}$	$3.13^{+0.20}_{-0.20}$	$3.15^{+0.21}_{-0.22}$	$3.13^{+0.20}_{-0.19}$	$3.14^{+0.21}_{-0.22}$
P15+LRG+BAO+H_0	$3.36^{+0.19}_{-0.19}$	$3.36^{+0.17}_{-0.17}$	$3.36^{+0.17}_{-0.17}$	$3.36^{+0.17}_{-0.17}$	$3.36^{+0.16}_{-0.18}$	$3.36^{+0.17}_{-0.16}$
Planck15+SZ	$3.05^{+0.29}_{-0.29}$	$3.33^{+0.33}_{-0.34}$	$3.34^{+0.31}_{-0.31}$	$3.33^{+0.31}_{-0.31}$	$3.36^{+0.30}_{-0.30}$	$3.39^{+0.29}_{-0.29}$
Planck15+SZ+H_0	$3.30^{+0.19}_{-0.18}$	$3.39^{+0.19}_{-0.18}$	$3.39^{+0.18}_{-0.18}$	$3.38^{+0.19}_{-0.19}$	$3.38^{+0.19}_{-0.18}$	$3.39^{+0.19}_{-0.19}$

Table 4.5: 68% CI constraints on N_{eff} for various combinations of data and numbers of knots for the model cases where N_{eff} is allowed to vary in addition to the standard cosmological parameters and knots with k and amplitude freedom in position.

Model comparison.— The change in Bayesian evidence relative to the six-parameter ΛCDM model is shown in Table 4.6 for the data sets Planck15+LRG+BAO($+H_0$). Importantly, there is no significant preference for any model that includes $\sum m_\nu$, N_{eff}, or knots over a simple ΛCDM model. The six-parameter ΛCDM model is also preferred with Planck15 data alone.

However, with the inclusion of the recent measurement of H_0, there is a significant preference for the combination of additional parameters N_{eff} and knots. The cases with 2, 4, and 5 knots all satisfy $\Delta \ln(Z) > 2.5$, which can be interpreted as "strong" or "significant" odds against ΛCDM. The Bayes factor for all models with positive $\Delta \ln(Z)$ are shown in Table 4.7.

Similarly, when the SZ data set is included with Planck15, there is a significant preference for the combination of a nonzero number of knots along with a nonzero value for the sum of the neutrino masses (see Table 4.4 for Planck15+SZ). When H_0 is also included, we see evidence for knots and N_{eff}. Table 4.8 shows the Bayes factor for both of these cases, Planck15+SZ

Planck15+LRG+BAO		Planck15+LRG+BAO+H_0	
Model	$\Delta \ln(Z)$	Model	$\Delta \ln(Z)$
ΛCDM	—	ΛCDM	—
+1 knot	0.99	+1 knot	1.60
+2 knots	1.07	+2 knots	1.15
+3 knots	0.75	+3 knots	1.40
+4 knots	0.61	+4 knots	1.31
+5 knots	0.59	+5 knots	0.78
—	—	+N_{eff}+1 knot	1.13
+N_{eff}+2 knots	0.10	+N_{eff}+2 knots	1.43
—	—	+N_{eff}+3 knots	0.74
—	—	+N_{eff}+4 knots	1.25
—	—	+N_{eff}+5 knots	0.89

Table 4.6: $\Delta \ln(Z)$ values relative to the six parameter ΛCDM model for various cosmological models for the combination of data sets Planck15+LRG+BAO and when H_0 is added. Only models for which $\Delta \ln(Z)$ is positive relative to ΛCDM are shown.

and Planck15+SZ+H_0. There is a significant preference for cosmological models with zero to five knots, with $\Delta \ln(Z) > 2.5$ for several model cases that contain additional non-standard cosmological parameters. For the combination of data sets Planck15+SZ+H_0, a cosmological model with 3 knots is heavily favored with $\Delta \ln(Z) > 5$. If we can assume that the tension data set SZ is an accurate measurement, as well as the measurement of H_0, then these results represent strong evidence that the PPS contains non-trivial features, not captured by a power-law representation. In particular, for this case, we see a preference for a very sharp cutoff at high k, as shown in Fig. 4.8. More conservatively, this is an indication that there are systematic effects within the data that mimic PPS features, which warrant further investigation.
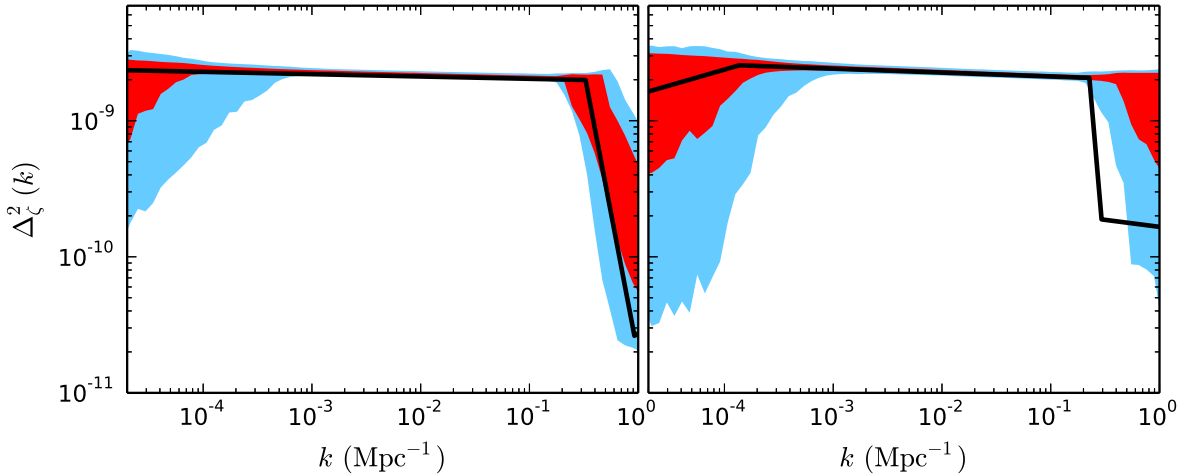
Figure 4.8: Shown *(left)* is the PPS for Planck15+SZ+H_0 with 3 knots, which corresponds to our model with the highest evidence. For comparison, we also show *(right)* the three knot case with only Planck15 data included. The black solid lines show the best-fit PPS, the red lines are PPS in the 68% CI, and the light blue lines are the PPS that fall in the 95% CI (note that it is possible for the PPS belonging to the sample with the maximum likelihood value to lie outside the red or blue regions).

Planck15			Planck15+H$_0$	
Model	$\Delta \ln(Z)$		Model	$\Delta \ln(Z)$
ΛCDM	—		ΛCDM	—
—	—		$+N_{\mathrm{eff}}$	0.49
+1 knot	1.00		+1 knot	1.56
+2 knots	1.18		+2 knots	2.02
+3 knots	1.68		+3 knots	1.72
+4 knots	0.91		+4 knots	2.05
+5 knots	0.60		+5 knots	1.92
$+N_{\mathrm{eff}}$+1 knot	0.40		$+N_{\mathrm{eff}}$+1 knot	2.27
$+N_{\mathrm{eff}}$+2 knots	0.45		$+N_{\mathrm{eff}}$+2 knots	_2.64_
$+N_{\mathrm{eff}}$+3 knots	0.13		$+N_{\mathrm{eff}}$+3 knots	2.43
$+N_{\mathrm{eff}}$+4 knots	0.50		$+N_{\mathrm{eff}}$+4 knots	_3.08_
—	—		$+N_{\mathrm{eff}}$+5 knots	_2.69_

Table 4.7: $\Delta \ln(Z)$ values relative to ΛCDM for various cosmological models for Planck15 and when H$_0$ is added. Only models for which $\Delta \ln(Z)$ is positive relative to ΛCDM are shown.

Planck15+SZ		Planck15+SZ+H$_0$	
Model	$\Delta \ln(Z)$	Model	$\Delta \ln(Z)$
ΛCDM	—	ΛCDM	—
$+\sum m_\nu$	1.41	—	—
+1 knot	2.65	+1 knot	3.09
+2 knots	2.78	+2 knots	3.48
+3 knots	3.06	+3 knots	**5.03**
+4 knots	4.37	+4 knots	4.74
+5 knots	4.33	+5 knots	2.94
$+\sum m_\nu$+1 knot	3.75	—	—
$+\sum m_\nu$+2 knots	3.49	—	—
$+\sum m_\nu$+3 knots	3.33	$+\sum m_\nu$+3 knots	1.60
$+\sum m_\nu$+4 knots	4.39	—	—
$+\sum m_\nu$+5 knots	4.49	$+\sum m_\nu$+5 knots	1.50
$+N_{\rm eff}$+1 knot	2.05	$+N_{\rm eff}$+1 knot	3.46
$+N_{\rm eff}$+2 knots	2.28	$+N_{\rm eff}$+2 knots	3.36
$+N_{\rm eff}$+3 knots	2.00	$+N_{\rm eff}$+3 knots	3.09
$+N_{\rm eff}$+4 knots	1.76	$+N_{\rm eff}$+4 knots	3.21
$+N_{\rm eff}$+5 knots	3.69	$+N_{\rm eff}$+5 knots	3.25
$+N_{\rm eff}+\sum m_\nu$+1 knot	2.49	$+N_{\rm eff}+\sum m_\nu$+1 knot	1.77
$+N_{\rm eff}+\sum m_\nu$+2 knots	2.60	$+N_{\rm eff}+\sum m_\nu$+2 knots	2.17
$+N_{\rm eff}+\sum m_\nu$+3 knots	2.46	$+N_{\rm eff}+\sum m_\nu$+3 knots	3.59
$+N_{\rm eff}+\sum m_\nu$+4 knots	2.81	$+N_{\rm eff}+\sum m_\nu$+4 knots	3.41
$+N_{\rm eff}+\sum m_\nu$+5 knots	3.71	$+N_{\rm eff}+\sum m_\nu$+5 knots	3.39

Table 4.8: $\Delta \ln(Z)$ values relative to 6-parameter ΛCDM for various cosmological models for the combination of data sets Planck15+SZ and when H$_0$ is added. Only models for which $\Delta \ln(Z) > 1.0$ relative to ΛCDM are shown. Significantly, there is no preference for neither extra relativistic degrees of freedom in $N_{\rm eff}$ nor non-zero $\sum m_\nu$.

4.4 Conclusions

Using data from a broad set of the most recent cosmological observations, including CMB, BAO, power spectrum, cluster counts, and Hubble constant measurements, we have examined the dependence on the assumed form of the PPS in measures of neutrino parameters $\sum m_\nu$ and N_{eff}. To do this, we applied the "knot-spline" method for reconstructing the PPS, following [113, 22, 6], and allowing the knot positions to vary in location as well as amplitude. We found that for this method of reconstruction, measures of N_{eff} and $\sum m_\nu$ do not appear to depend strongly on assumptions about the PPS. However, when the knot location is fixed, with CMB data alone, we observe a strong dependency between $\sum m_\nu$ and the prior on the PPS. While including information from LSS mitigates much of this dependency, this work underscores the importance of quantifying the dependence of parameter constraints on model assumptions and demonstrates the sensitivity of neutrino parameter constraints on PPS priors and choice of data sets.

For combinations of data which include Planck15, BAO, LRG, and WZ, we see no evidence for features in the PPS or a non-zero number of knots. In addition, there is no preference for significant non-zero neutrino mass or a value for N_{eff} outside of the standard value expected in ΛCDM. Significantly, when we include recent high-precision measurements of the low-redshift Hubble constant, we find no significant evidence for extra relativistic energy density N_{eff}. However, we do see relatively significant evidence for a non-zero number of knots in concert with a value for N_{eff} that diverges from the standard value. When including the tension data from SZ cluster counts, we see weak evidence for non-zero neutrino mass and more significant evidence for knots or knots with N_{eff} and $\sum m_\nu$. However, when both H_0 and SZ measurements are included, the preference for $\sum m_\nu$ vanishes, and only models which allow for both N_{eff} and knots to vary are favored, with a model containing only 3 knots in addition to the standard ΛCDM cosmological parameters being preferred the most strongly over ΛCDM. The radical difference in the Bayesian evidences obtained for extensions to

the 6-parameter ΛCDM model with combinations of these data most conservatively points to some unmodeled systematic effect, rather than a coherent body of evidence in favor of non-standard cosmology.

As a combination of low, medium and high-redshift probes are complementarily combined to constrain expansion history, cosmological matter, dark energy, neutrino densities, and the primordial power spectrum, robust methods of indications of new model features and measures of new physics should be employed. Our work finds that relaxing *a priori* assumptions of the scales of features in the primordial power spectrum does not significantly alleviate constraints on neutrino mass and relativistic energy density. Significantly, we find the tension in cosmological data from representative cluster data sets do not significantly indicate a non-zero measure of massive neutrinos. Also, we find the tension from Planck 2015 CMB and recent high-precision H_0 measures give no preference for a non-standard N_{eff}. As cosmology enters an increasingly high-precision era with multiple epoch and physical scale probes, robust statistical methods and model tests will continue to be needed in order to make claims for the discovery of new physics.

Chapter Acknowledgements
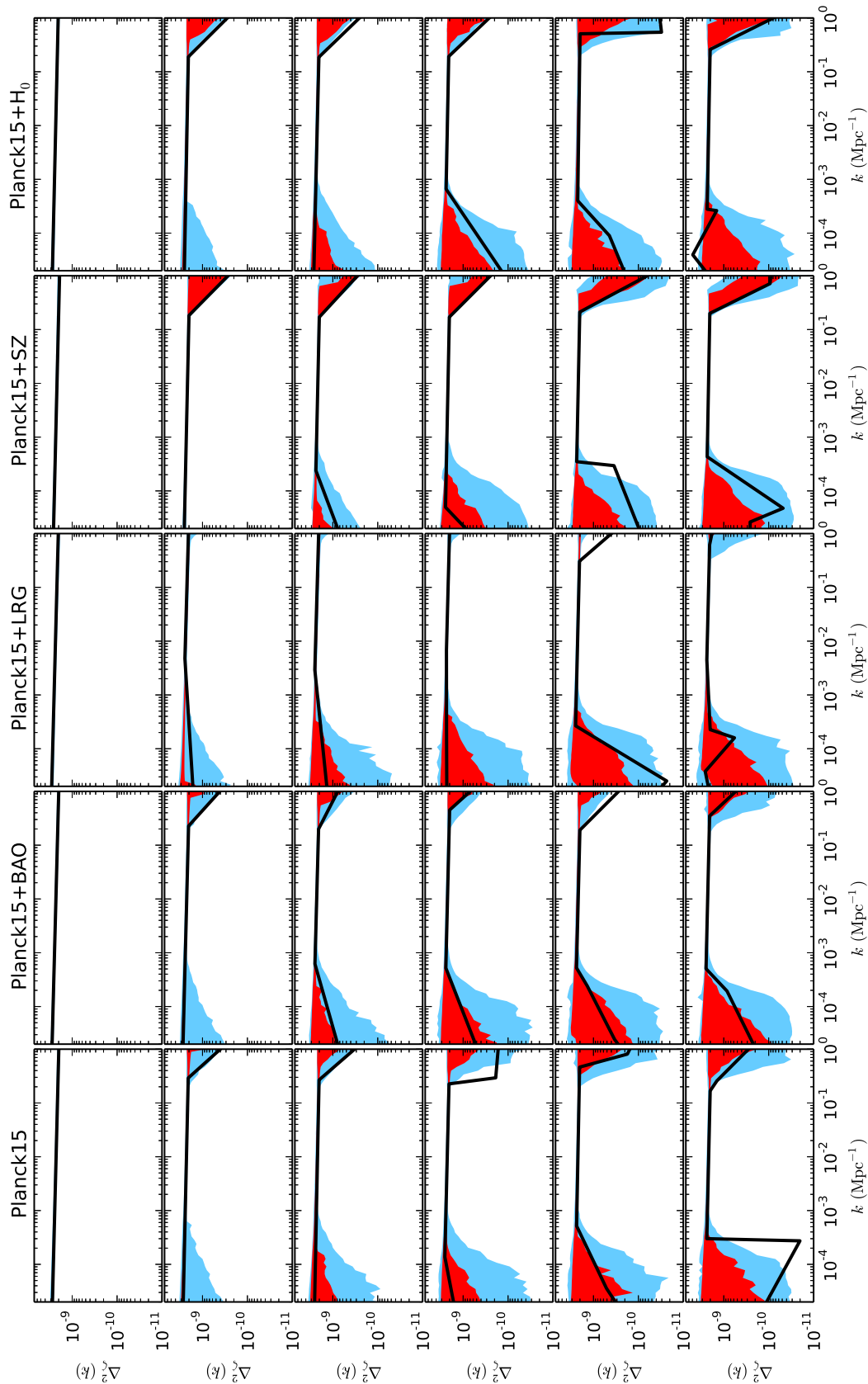
Figure 4.9: The reconstructed primordial power spectrum (PPS) without varying neutrino parameters. The columns correspond to different data sets used, shown at the top of each column. The number of knots increases from 0 to 5 from top to bottom. The black solid lines show the best-fit PPS, the red lines are PPS in the 68% CI, and the light blue lines are the PPS that fall in the 95% CI.

Chapter 5

Summary and Conclusion

This work has centered around using astronomical and cosmological observations to study the derived properties of dark matter and neutrinos and to characterize how these properties are affected by model assumptions. Here, I summarize the main conclusions from each chapter.

In chapter 2, I discussed how modifications to the modeling of the gamma-ray background in the GC affect the inferred parameters of the GCE source. Despite this dependence, the GCE was detected with high significance regardless of the choice of background model, and either an astrophysical or dark matter explanation remained viable, albeit with different derived properties. In particular, I find that the b-quark or τ-lepton channels are roughly equally preferred, although their best fit particle pass differs considerably, and that uncertainties are dominated by systematic uncertainty related to modeling of the gamma-ray background. Alternatively, the GCE could be explained by an unresolved population of MSPs. I find that estimates for the number, distribution, and spectrum of the MSPs could account for the entirety of the GCE. Assuming a purely astrophysical explanation for the GCE, I derived strong limits on the dark matter annihilation cross section, although these too had a large

model depdence.

In chapter 3, I discuss the detection of a new excess of gamma-rays toward the GC with a spatial distribution that traces infrared starlight. This spectrum of this source is consistent with a population of electrons and positrons with energies up to around 10 GeV upscattering photons in the interstellar radiation field. I find that the population of electrons and positrons that could produce this observed IC emission could also account for the emission, interpreted as bremsstrahlung radiation, associated with the 20 cm radio map included in previous works. I show that the GCE source is still detected with high significance and that a dark matter model annihilating to leptons could produce the population of electrons and positrons responsible for the IC and bremsstrahlung components, thus providing a single source to explain all three gamma-ray excesses. Nevertheless, astrophysical explanations for the excess can not be ruled out at this time.

Finally, in chapter 4 I explore how sensitive neutrino parameter constraints are to a relaxation of the assumption that the PPS is a featureless power-law. I find, using a model independent-method for reconstructing the PPS that interpolates between specified knot locations, that constraints on the sum of the neutrino masses along with the number of relativisitic degrees of freedom are robust when using a reconstruction that allows the knots to vary freely in both location and amplitude. Furthermore, I find that certain combinations of data sets place stringent constraints on the sum of the neutrino masses, nearing the level of precision necessary to differentiate between an inverted or normal neutrino mass heirarchy. Perhaps even more interestingly, I find that for some data sets there is evidence for non-standard values of $\sum m_\nu$, N_{eff}, along with features in the PPS. This indicates that there is some tension between the available data sets, which could indicate systematics within the data that are not properly understood.

The work in this thesis highlights the importance of performing detailed analyses of the effect of model assumptions and systematic uncertainties when deriving parameter constraints

using an empirical, model dependent approach. Future advances in gamma-ray astronomy and continued multiwavelength analyses will provide a much more precise understanding of backgrounds in the GC, possiby paving the way to identifing the source of the gamma-ray excesses. In addition, the observed robustness of neutrino parameter constraints to freedom in the PPS will become even more important as the next generation of cosmological measurements continues to push constraints on the sum of neutrino masses closer to the minimum value allowed by laboratory experiments.

Bibliography

[1] Galprop. `http://galprop.stanford.edu/`.

[2] G. Aad et al. Search for dark matter candidates and large extra dimensions in events with a jet and missing transverse momentum with the ATLAS detector. *JHEP*, 1304:075, 2013.

[3] K. Abazajian, E. Calabrese, A. Cooray, F. De Bernardis, S. Dodelson, et al. Cosmological and Astrophysical Neutrino Mass Measurements. *Astropart.Phys.*, 35:177–184, 2011.

[4] K. N. Abazajian. The Consistency of Fermi-LAT Observations of the Galactic Center with a Millisecond Pulsar Population in the Central Stellar Cluster. *JCAP*, 1103:010, 2011.

[5] K. N. Abazajian, P. Agrawal, Z. Chacko, and C. Kilic. Conservative Constraints on Dark Matter from the Fermi-LAT Isotropic Diffuse Gamma-Ray Background Spectrum. *JCAP*, 1011:041, 2010.

[6] K. N. Abazajian, G. Aslanyan, R. Easther, and L. C. Price. The Knotted Sky II: Does BICEP2 require a nontrivial primordial power spectrum? *JCAP*, 1408:053, 2014.

[7] K. N. Abazajian, N. Canac, S. Horiuchi, and M. Kaplinghat. Astrophysical and Dark Matter Interpretations of Extended Gamma-Ray Emission from the Galactic Center. *Phys.Rev.*, D90:023526, 2014.

[8] K. N. Abazajian et al. The Seventh Data Release of the Sloan Digital Sky Survey. *Astrophys. J. Suppl.*, 182:543–558, 2009.

[9] K. N. Abazajian and J. Harding. Constraints on WIMP and Sommerfeld-Enhanced Dark Matter Annihilation from HESS Observations of the Galactic Center. *JCAP*, 1201:041, 2012.

[10] K. N. Abazajian and M. Kaplinghat. Detection of a Gamma-Ray Source in the Galactic Center Consistent with Extended Emission from Dark Matter Annihilation and Concentrated Astrophysical Emission. *Phys.Rev.*, D86:083511, 2012.

[11] K. N. Abazajian and M. Kaplinghat. Neutrino Physics from the Cosmic Microwave Background and Large Scale Structure. *Ann. Rev. Nucl. and Part. Phys.*, 2016. in press.

[12] A. Abramowski et al. Search for a Dark Matter annihilation signal from the Galactic Center halo with H.E.S.S. *Phys.Rev.Lett.*, 106:161301, 2011.

[13] M. Ackermann et al. Dark Matter Constraints from Observations of 25 Milky Way Satellite Galaxies with the Fermi Large Area Telescope. 2013.

[14] R. Adam et al. Planck 2015 results. I. Overview of products and scientific results. 2015.

[15] P. A. R. Ade et al. Planck 2013 results. XX. Cosmology from SunyaevZeldovich cluster counts. *Astron. Astrophys.*, 571:A20, 2014.

[16] P. A. R. Ade et al. Planck 2015 results. XIII. Cosmological parameters. 2015.

[17] P. A. R. Ade et al. Planck 2015 results. XX. Constraints on inflation. 2015.

[18] N. Aghanim et al. Planck 2016 intermediate results. XLVI. Reduction of large-scale systematic effects in HFI polarization maps and estimation of the reionization optical depth. 2016.

[19] F. Aharonian, A. G. Akhperjanian, A. R. Bazer-Bachi, M. Beilicke, W. Benbow, D. Berge, K. Bernlöhr, C. Boisson, O. Bolz, V. Borrel, I. Braun, F. Breitling, A. M. Brown, P. M. Chadwick, L.-M. Chounet, R. Cornils, L. Costamante, B. Degrange, H. J. Dickinson, A. Djannati-Ataï, L. O. Drury, G. Dubus, D. Emmanoulopoulos, P. Espigat, F. Feinstein, G. Fontaine, Y. Fuchs, S. Funk, Y. A. Gallant, B. Giebels, S. Gillessen, J. F. Glicenstein, P. Goret, C. Hadjichristidis, D. Hauser, M. Hauser, G. Heinzelmann, G. Henri, G. Hermann, J. A. Hinton, W. Hofmann, M. Holleran, D. Horns, A. Jacholkowska, O. C. de Jager, B. Khélifi, S. Klages, N. Komin, A. Konopelko, I. J. Latham, R. Le Gallou, A. Lemière, M. Lemoine-Goumard, N. Leroy, T. Lohse, A. Marcowith, J. M. Martin, O. Martineau-Huynh, C. Masterson, T. J. L. McComb, M. de Naurois, S. J. Nolan, A. Noutsos, K. J. Orford, J. L. Osborne, M. Ouchrif, M. Panter, G. Pelletier, S. Pita, G. Pühlhofer, M. Punch, B. C. Raubenheimer, M. Raue, J. Raux, S. M. Rayner, A. Reimer, O. Reimer, J. Ripken, L. Rob, L. Rolland, G. Rowell, V. Sahakian, L. Saugé, S. Schlenker, R. Schlickeiser, C. Schuster, U. Schwanke, M. Siewert, H. Sol, D. Spangler, R. Steenkamp, C. Stegmann, J.-P. Tavernet, R. Terrier, C. G. Théoret, M. Tluczykont, C. van Eldik, G. Vasileiadis, C. Venter, P. Vincent, H. J. Völk, and S. J. Wagner. Discovery of very-high-energy γ-rays from the Galactic Centre ridge. *Nature*, 439:695–698, Feb. 2006.

[20] L. Anderson et al. The clustering of galaxies in the SDSS-III Baryon Oscillation Spectroscopic Survey: baryon acoustic oscillations in the Data Releases 10 and 11 Galaxy samples. *Mon. Not. Roy. Astron. Soc.*, 441(1):24–62, 2014.

[21] G. Aslanyan. Cosmo++: An Object-Oriented C++ Library for Cosmology. *Comput. Phys. Commun.*, 185:3215–3227, 2014.

[22] G. Aslanyan, L. C. Price, K. N. Abazajian, and R. Easther. The Knotted Sky I: Planck constraints on the primordial power spectrum. *JCAP*, 1408:052, 2014.

[23] B. Audren, J. Lesgourgues, K. Benabed, and S. Prunet. Conservative Constraints on Early Cosmology: an illustration of the Monte Python cosmological parameter inference code. *JCAP*, 1302:001, 2013.

[24] E. A. Baltz, J. E. Taylor, and L. L. Wai. Can Astrophysical Gamma Ray Sources Mimic Dark Matter Annihilation in Galactic Satellites? *Astrophys.J.*, 659:L125–L128, 2007.

[25] R. A. Battye, T. Charnock, and A. Moss. Tension between the power spectrum of density perturbations measured on large and small scales. *Phys. Rev.*, D91(10):103508, 2015.

[26] R. A. Battye and A. Moss. Evidence for Massive Neutrinos from Cosmic Microwave Background and Lensing Observations. *Phys. Rev. Lett.*, 112(5):051303, 2014.

[27] G. Belanger, F. Boudjema, A. Pukhov, and A. Semenov. micrOMEGAs_3: A program for calculating dark matter observables. *Comput.Phys.Commun.*, 185:960–985, 2014.

[28] L. Bergstrom, T. Bringmann, I. Cholis, D. Hooper, and C. Weniger. New limits on dark matter annihilation from AMS cosmic ray positron data. *Phys.Rev.Lett.*, 111:171101, 2013.

[29] L. Bergstrom, P. Ullio, and J. H. Buckley. Observability of gamma-rays from dark matter neutralino annihilations in the Milky Way halo. *Astropart.Phys.*, 9:137–162, 1998.

[30] A. Berlin and D. Hooper. Stringent Constraints On The Dark Matter Annihilation Cross Section From Subhalo Searches With The Fermi Gamma-Ray Space Telescope. *Phys.Rev.*, D89:016014, 2014.

[31] F. Beutler, C. Blake, M. Colless, D. H. Jones, L. Staveley-Smith, L. Campbell, Q. Parker, W. Saunders, and F. Watson. The 6dF Galaxy Survey: Baryon Acoustic Oscillations and the Local Hubble Constant. *Mon. Not. Roy. Astron. Soc.*, 416:3017–3032, 2011.

[32] F. Beutler et al. The clustering of galaxies in the SDSS-III Baryon Oscillation Spectroscopic Survey: Signs of neutrino mass in current cosmological datasets. *Mon. Not. Roy. Astron. Soc.*, 444:3501, 2014.

[33] S. Bird, H. V. Peiris, M. Viel, and L. Verde. Minimally Parametric Power Spectrum Reconstruction from the Lyman-alpha Forest. *Mon. Not. Roy. Astron. Soc.*, 413:1717–1728, 2011.

[34] S. Bird, M. Viel, and M. G. Haehnelt. Massive Neutrinos and the Non-linear Matter Power Spectrum. *Mon. Not. Roy. Astron. Soc.*, 420:2551–2561, 2012.

[35] D. Blas, J. Lesgourgues, and T. Tram. The Cosmic Linear Anisotropy Solving System (CLASS) II: Approximation schemes. *JCAP*, 1107:034, 2011.

[36] G. R. Blumenthal, S. M. Faber, R. Flores, and J. R. Primack. Contraction of dark matter galactic halos due to baryonic infall. *Astrophys. J.*, 301:27–34, Feb. 1986.

[37] A. Boyarsky, D. Malyshev, and O. Ruchayskiy. A comment on the emission from the Galactic Center as seen by the Fermi telescope. *Phys.Lett.*, B705:165–169, 2011.

[38] M. Bridges, F. Feroz, M. P. Hobson, and A. N. Lasenby. Bayesian optimal reconstruction of the primordial power spectrum. *Mon. Not. Roy. Astron. Soc.*, 400:1075–1084, 2009.

[39] M. Bridges, A. N. Lasenby, and M. P. Hobson. A bayesian analysis of the primordial power spectrum. *Mon. Not. Roy. Astron. Soc.*, 369:1123–1130, 2006.

[40] M. Bridges, A. N. Lasenby, and M. P. Hobson. WMAP 3-year primordial power spectrum. *Mon. Not. Roy. Astron. Soc.*, 381:68–74, 2007.

[41] F. Calore, I. Cholis, and C. Weniger. Background model systematics for the Fermi GeV excess. 2014.

[42] E. Carlson and S. Profumo. Cosmic Ray Protons in the Inner Galaxy and the Galactic Center Gamma-Ray Excess. *Phys.Rev.*, D90:023015, 2014.

[43] R. Catena and P. Ullio. A novel determination of the local dark matter density. *JCAP*, 1008:004, 2010.

[44] S. Chatrchyan et al. Search for dark matter and large extra dimensions in monojet events in pp collisions at $\sqrt{s} = 7$ TeV. *JHEP*, 1209:094, 2012.

[45] M. Chernyakova, D. Malyshev, F. Aharonian, R. Crocker, and D. Jones. The high-energy, Arcminute-scale galactic center gamma-ray source. *Astrophys.J.*, 726:60, 2011.

[46] M. Cirelli, G. Corcella, A. Hektor, G. Hutsi, M. Kadastik, et al. PPPC 4 DM ID: A Poor Particle Physicist Cookbook for Dark Matter Indirect Detection. *JCAP*, 1103:051, 2011.

[47] M. Cirelli, P. D. Serpico, and G. Zaharijas. Bremsstrahlung gamma rays from light Dark Matter. *JCAP*, 1311:035, 2013.

[48] S. Colafrancesco, S. Profumo, and P. Ullio. Multi-frequency analysis of neutralino dark matter annihilations in the Coma cluster. *Astron.Astrophys.*, 455:21, 2006.

[49] A. J. Cuesta, V. Niro, and L. Verde. Neutrino mass limits: robust information from the power spectrum of galaxy surveys. 2015.

[50] T. Daylan, D. P. Finkbeiner, D. Hooper, T. Linden, S. K. N. Portillo, et al. The Characterization of the Gamma-Ray Signal from the Central Milky Way: A Compelling Case for Annihilating Dark Matter. 2014.

[51] R. de Putter, E. V. Linder, and A. Mishra. Inflationary Freedom and Cosmological Neutrino Constraints. *Phys. Rev.*, D89(10):103502, 2014.

[52] T. Delahaye, R. Lineros, F. Donato, N. Fornengo, and P. Salati. Positrons from dark matter annihilation in the galactic halo: Theoretical uncertainties. *Phys.Rev.*, D77:063527, 2008.

[53] E. Di Valentino, S. Gariazzo, M. Gerbino, E. Giusarma, and O. Mena. Dark Radiation and Inflationary Freedom after Planck 2015. *Phys. Rev.*, D93(8):083523, 2016.

[54] A. Drlica-Wagner. *Searching for Dwarf Spheroidal Galaxies and other Galactic Dark Matter Substructures with the Fermi Large Area Telescope*. PhD thesis, Stanford University, 2013.

[55] G. Efstathiou. H0 Revisited. *Mon. Not. Roy. Astron. Soc.*, 440(2):1138–1152, 2014.

[56] J. L. Feng. Dark Matter Candidates from Particle Physics and Methods of Detection. *Ann.Rev.Astron.Astrophys.*, 48:495, 2010.

[57] F. Feroz and M. P. Hobson. Multimodal nested sampling: an efficient and robust alternative to MCMC methods for astronomical data analysis. *Mon. Not. Roy. Astron. Soc.*, 384:449, 2008.

[58] F. Feroz, M. P. Hobson, and M. Bridges. MultiNest: an efficient and robust Bayesian inference tool for cosmology and particle physics. *Mon. Not. Roy. Astron. Soc.*, 398:1601–1614, 2009.

[59] F. Feroz, M. P. Hobson, E. Cameron, and A. N. Pettitt. Importance Nested Sampling and the MultiNest Algorithm. 2013.

[60] Y. Fukuda et al. Measurement of the flux and zenith angle distribution of upward through going muons by Super-Kamiokande. *Phys. Rev. Lett.*, 82:2644–2648, 1999.

[61] S. Gariazzo, C. Giunti, and M. Laveder. Light Sterile Neutrinos and Inflationary Freedom. *JCAP*, 1504(04):023, 2015.

[62] E. Giusarma, E. Di Valentino, M. Lattanzi, A. Melchiorri, and O. Mena. Relic Neutrinos, thermal axions and cosmology in early 2014. *Phys. Rev.*, D90(4):043507, 2014.

[63] E. Giusarma, M. Gerbino, O. Mena, S. Vagnozzi, S. Ho, and K. Freese. On the improvement of cosmological neutrino mass bounds. 2016.

[64] P. Goldreich and W. H. Julian. Pulsar Electrodynamics. *Astrophys. J.*, 157:869, Aug. 1969.

[65] P. Gondolo, J. Edsjo, P. Ullio, L. Bergstrom, M. Schelke, et al. DarkSUSY: Computing supersymmetric dark matter properties numerically. *JCAP*, 0407:008, 2004.

[66] L. Goodenough and D. Hooper. Possible Evidence For Dark Matter Annihilation In The Inner Milky Way From The Fermi Gamma Ray Space Telescope. 2009.

[67] J. Goodman, M. Ibe, A. Rajaraman, W. Shepherd, T. M. Tait, et al. Constraints on Dark Matter from Colliders. *Phys.Rev.*, D82:116010, 2010.

[68] C. Gordon and O. Macias. Dark Matter and Pulsar Model Constraints from Galactic Center Fermi-LAT Gamma Ray Observations. *Phys.Rev.*, D88:083521, 2013.

[69] A. K. Harding and R. Ramaty. The Pulsar Contribution to Galactic Cosmic Ray Positrons. *International Cosmic Ray Conference*, 2:92, 1987.

[70] C. He, K. Bechtol, A. P. Hearin, and D. Hooper. Prospects for Detecting Gamma Rays from Annihilating Dark Matter in Dwarf Galaxies in the Era of DES and LSST. 2013.

[71] M. P. Hobson, A. H. Jaffe, A. R. Liddle, P. Mukherjee, and D. Parkinson. *Bayesian methods in cosmology*. Cambridge University Press, 2010.

[72] D. Hooper and L. Goodenough. Dark Matter Annihilation in The Galactic Center As Seen by the Fermi Gamma Ray Space Telescope. *Phys.Lett.*, B697:412–428, 2011.

[73] D. Hooper, C. Kelso, and F. S. Queiroz. Stringent and Robust Constraints on the Dark Matter Annihilation Cross Section From the Region of the Galactic Center. *Astropart.Phys.*, 46:55–70, 2013.

[74] D. Hooper and T. Linden. On The Origin Of The Gamma Rays From The Galactic Center. *Phys.Rev.*, D84:123005, 2011.

[75] D. Hooper and T. R. Slatyer. Two Emission Mechanisms in the Fermi Bubbles: A Possible Signal of Annihilating Dark Matter. *Phys.Dark Univ.*, 2:118–138, 2013.

[76] Z. Hou et al. Constraints on Cosmology from the Cosmic Microwave Background Power Spectrum of the 2500 deg^2 SPT-SZ Survey. *Astrophys. J.*, 782:74, 2014.

[77] W. Hu, D. J. Eisenstein, and M. Tegmark. Weighing neutrinos with galaxy surveys. *Phys. Rev. Lett.*, 80:5255–5258, 1998.

[78] H. Jeffreys. *Theory of Probability*. Oxford University Press, 1961.

[79] W. H. Kinney. How to fool cosmic microwave background parameter estimation. *Phys. Rev.*, D63:043001, 2001.

[80] A. Klypin, H. Zhao, and R. S. Somerville. LCDM-based models for the Milky Way and M31 I: Dynamical Models. *Astrophys. J.*, 573:597–613, 2002.

[81] S. M. Koushiappas. Joint dataset analysis and dark matter constraints from dwarf galaxies. Talk presented at the Aspen Winter Workshop, Closing in on Dark Matter, 2013.

[82] T. Lacroix, C. Boehm, and J. Silk. Fitting the Fermi-LAT GeV excess: On the importance of including the propagation of electrons from dark matter. *Phys.Rev.*, D90:043508, 2014.

[83] C. J. Law, F. Yusef-Zadeh, W. D. Cotton, and R. J. Maddalena. Green Bank Telescope Multiwavelength Survey of the Galactic Center Region. *Astrophys. J. Supp.*, 177:255–274, July 2008.

[84] B. Leistedt, H. V. Peiris, and L. Verde. No new cosmological concordance with massive sterile neutrinos. *Phys. Rev. Lett.*, 113:041301, 2014.

[85] J. Lesgourgues. The Cosmic Linear Anisotropy Solving System (CLASS) I: Overview. 2011.

[86] T. Linden, D. Hooper, and F. Yusef-Zadeh. Dark Matter and Synchrotron Emission from Galactic Center Radio Filaments. *Astrophys.J.*, 741:95, 2011.

[87] T. Linden, E. Lovegrove, and S. Profumo. The Morphology of Hadronic Emission Models for the Gamma-Ray Source at the Galactic Center. *Astrophys.J.*, 753:41, 2012.

[88] N. MacCrann, J. Zuntz, S. Bridle, B. Jain, and M. R. Becker. Cosmic Discordance: Are Planck CMB and CFHTLenS weak lensing measurements out of tune? *Mon. Not. Roy. Astron. Soc.*, 451(3):2877–2888, 2015.

[89] O. Macias and C. Gordon. The Contribution of Cosmic Rays Interacting With Molecular Clouds to the Galactic Center Gamma-Ray Excess. *Phys.Rev.*, D89:063515, 2014.

[90] M. Muno, F. Bauer, F. Baganoff, R. Bandyopadhyay, G. Bower, et al. A Catalog of X-ray Point Sources from Two Megaseconds of Chandra Observations of the Galactic Center. *Astrophys.J.Suppl.*, 181:110–128, 2009.

[91] J. F. Navarro, C. S. Frenk, and S. D. M. White. A Universal Density Profile from Hierarchical Clustering. *Astrophys. J.*, 490:493–508, 1997.

[92] K. C. Y. Ng, R. Laha, S. Campbell, S. Horiuchi, B. Dasgupta, et al. Resolving Small-Scale Dark Matter Structures Using Multi-Source Indirect Detection. *Phys.Rev.*, D89:083001, 2014.

[93] P. L. Nolan, A. A. Abdo, M. Ackermann, M. Ajello, A. Allafort, E. Antolini, W. B. Atwood, M. Axelsson, L. Baldini, J. Ballet, and et al. Fermi Large Area Telescope Second Source Catalog. *Astrophys.J.Suppl.*, 199:31, 2012.

[94] K. A. Olive et al. Review of Particle Physics. *Chin. Phys.*, C38:090001, 2014.

[95] D. Parkinson et al. The WiggleZ Dark Energy Survey: Final data release and cosmological results. *Phys. Rev.*, D86:103518, 2012.

[96] H. V. Peiris and L. Verde. The Shape of the Primordial Power Spectrum: A Last Stand Before Planck. *Phys. Rev.*, D81:021302, 2010.

[97] J. Petrovic, P. D. Serpico, and G. Zaharijas. Galactic Center gamma-ray "excess" from an active past of the Galactic Centre? 2014.

[98] T. A. Porter, I. V. Moskalenko, A. W. Strong, E. Orlando, and L. Bouchet. Inverse Compton Origin of the Hard X-Ray and Soft Gamma-Ray Emission from the Galactic Ridge. *Astrophys.J.*, 682:400–407, 2008.

[99] A. Ravenni, L. Verde, and A. J. Cuesta. Red, Straight, no bends: primordial power spectrum reconstruction from CMB and large-scale structure. 2016.

[100] M. Raveri. Are cosmological data sets consistent with each other within the Λ cold dark matter model? *Phys. Rev.*, D93(4):043522, 2016.

[101] B. A. Reid et al. Cosmological Constraints from the Clustering of the Sloan Digital Sky Survey DR7 Luminous Red Galaxies. *Mon. Not. Roy. Astron. Soc.*, 404:60–85, 2010.

[102] A. G. Riess et al. A 2.4% Determination of the Local Value of the Hubble Constant. 2016.

[103] M. Roncarelli, C. Carbone, and L. Moscardini. The effect of massive neutrinos on the SunyaevZel'dovich and X-ray observables of galaxy clusters. *Mon. Not. Roy. Astron. Soc.*, 447(2):1761–1773, 2015.

[104] A. J. Ross, L. Samushia, C. Howlett, W. J. Percival, A. Burden, and M. Manera. The clustering of the SDSS DR7 main Galaxy sample I. A 4 per cent distance measure at $z = 0.15$. *Mon. Not. Roy. Astron. Soc.*, 449(1):835–847, 2015.

[105] S. Roy and A. P. Rao. GMRT observations of four suspected supernova remnants near the Galactic Centre. *Mon. Not. Roy. Astron. Soc.*, 329:775–786, Feb. 2002.

[106] E. Rozo et al. Cosmological Constraints from the SDSS maxBCG Cluster Catalog. *Astrophys. J.*, 708:645–660, 2010.

[107] A. Saro et al. Constraints on the CMB temperature evolution using multiband measurements of the SunyaevZel'dovich effect with the South Pole Telescope. *Mon. Not. Roy. Astron. Soc.*, 440(3):2610–2615, 2014.

[108] D. J. Schlegel, D. P. Finkbeiner, and M. Davis. Maps of dust IR emission for use in estimation of reddening and CMBR foregrounds. *Astrophys.J.*, 500:525, 1998.

[109] C. Sealfon, L. Verde, and R. Jimenez. Smoothing spline primordial power spectrum reconstruction. *Phys. Rev.*, D72:103520, 2005.

[110] M. Skrutskie, R. Cutri, R. Stiening, M. Weinberg, S. Schneider, et al. The Two Micron All Sky Survey (2MASS). *Astron.J.*, 131:1163–1183, 2006.

[111] V. Springel, S. D. M. White, C. S. Frenk, J. F. Navarro, A. Jenkins, M. Vogelsberger, J. Wang, A. Ludlow, and A. Helmi. Prospects for detecting supersymmetric dark matter in the Galactic halo. *Nature*, 456:73–76, Nov. 2008.

[112] R. Takahashi, M. Sato, T. Nishimichi, A. Taruya, and M. Oguri. Revising the Halofit Model for the Nonlinear Matter Power Spectrum. *Astrophys. J.*, 761:152, 2012.

[113] J. A. Vazquez, M. Bridges, M. P. Hobson, and A. N. Lasenby. Model selection applied to reconstruction of the Primordial Power Spectrum. *JCAP*, 1206:006, 2012.

[114] J. A. Vazquez, A. N. Lasenby, M. Bridges, and M. P. Hobson. A Bayesian study of the primordial power spectrum from a novel closed universe model. *Mon. Not. Roy. Astron. Soc.*, 422:1948–1956, 2012.

[115] L. Verde, S. M. Feeney, D. J. Mortlock, and H. V. Peiris. (Lack of) Cosmological evidence for dark radiation after Planck. *JCAP*, 1309:013, 2013.

[116] L. Verde and H. V. Peiris. On Minimally-Parametric Primordial Power Spectrum Reconstruction and the Evidence for a Red Tilt. *JCAP*, 0807:009, 2008.

[117] L. Verde, P. Protopapas, and R. Jimenez. Planck and the local Universe: Quantifying the tension. *Phys. Dark Univ.*, 2:166–175, 2013.

[118] A. Vikhlinin et al. Chandra Cluster Cosmology Project III: Cosmological Parameter Constraints. *Astrophys. J.*, 692:1060–1074, 2009.

[119] E. L. Wright, P. R. M. Eisenhardt, A. K. Mainzer, et al. The Wide-field Infrared Survey Explorer (WISE): Mission Description and Initial On-orbit Performance. *Astron.J.*, 140:1868–1881, Dec. 2010.

[120] M. Wyman, D. H. Rudd, R. A. Vanderveld, and W. Hu. Neutrinos Help Reconcile Planck Measurements with the Local Universe. *Phys. Rev. Lett.*, 112(5):051302, 2014.

[121] F. Yusef-Zadeh, J. Hewitt, M. Wardle, V. Tatischeff, D. Roberts, et al. Interacting Cosmic Rays with Molecular Clouds: A Bremsstrahlung Origin of Diffuse High Energy Emission from the Inner 2deg by 1deg of the Galactic Center. *Astrophys.J.*, 762:33, 2013.

[122] L. Zhang, H.-W. Rix, G. van de Ven, J. Bovy, C. Liu, et al. The Gravitational Potential Near the Sun From SEGUE K-dwarf Kinematics. *Astrophys.J.*, 772:108, 2013.

[123] B. Zhou, Y.-F. Liang, X. Huang, X. Li, Y.-Z. Fan, et al. GeV excess in the Milky Way: Depending on Diffuse Galactic gamma ray Emission template? 2014.

Appendix A

Residual Flux and Error

The plots in this paper show both the residual flux and an alternate estimate of the spectral energy distribution. We summarize the methods to create them both here. The residual flux in some energy bin α is

$$r_\alpha = \sum_\beta \frac{(n_{\alpha\beta} - b_{\alpha\beta})}{\epsilon_{\alpha\beta}} \,, \tag{A.1}$$

where $n_{\alpha\beta}$ and $b_{\alpha\beta}$ are the total counts and the background model count (all sources minus the source of interest), respectively. The sum is over all spatial bins within the ROI or part of ROI, as desired and ϵ is the exposure. The Poisson error on this flux is given by,

$$\delta r_\alpha^2 = \sum_\beta \frac{m_{\alpha\beta}}{\epsilon_{\alpha\beta}^2} \tag{A.2}$$

An alternate way to estimate the SED is to fix the background (b) and maximize the likeli-

hood in each energy bin for the amplitude of the source of interest. We note that this SED estimate does not account for the correlations between GCE and other source parameters but it is the quantity most directly comparable to the residual flux. This likelihood (up to a constant) is

$$\ln \mathscr{L}_\alpha = -\sum_\beta m_{\alpha\beta} + \sum_\beta n_{\alpha\beta} \ln(m_{\alpha\beta}) \tag{A.3}$$

Writing $m_{\alpha\beta} = b_{\alpha\beta} + a_\alpha s_{\alpha\beta}$ where s labels the counts for the source of interest, the maximum likelihood estimate of a_α and the error on a_α are given by

$$\sum_\beta (n_{\alpha\beta}/m_{\alpha\beta} - 1)s_{\alpha\beta} = 0$$
$$\delta a_\alpha^{-2} = \sum_\beta n_{\alpha\beta} s_{\alpha\beta}^2/m_{\alpha\beta}^2$$

The SED estimate is $(a_\alpha \pm \delta a_\alpha) \sum_\beta s_{\alpha\beta}/\epsilon_{\alpha\beta}$. The SED estimate and residual flux values generally agree with each other.

Appendix B

Robustness of results against background model systematics

In order to confirm the robustness of our detection, we wish to characterize the behavior of the newly reported IC excess through a range of systematic uncertainties in our analysis. We use the GALPROP code [1] to generate additional diffuse background models, and repeat our analysis using these diffuse models in place of the Fermi Pass 7 diffuse model.

We use models selected from the collection tested by [41] in their systematic analysis of the GCE signal. For consistency, we will use the same model names as Ref. [41]. If one examines the IC and π^0+bremsstrahlung components of the diffuse models in Ref. [41], it is apparent that their spectral shapes (with a few exceptions, see model "E" below) are similar between models and thus running the full suite of 128 backgrounds would produce many degenerate results. Instead, we test two models chosen for their extreme IC parameters, along with two models with more standard parameters. The extreme models were chosen with the intent of testing backgrounds with IC components that were more likely to absorb the excess we have identified and decrease its detection significance. When performing fits using

these GALPROP-generated models, we allow the π^0+bremsstrahlung and IC components to be scaled separately to allow for the possibility that our claimed IC excess is simply an underfitting of the background IC emission. The following models were tested.

- Model A is the reference model in Ref. [41].

- Model E has a low diffusion coefficient K_0. We chose Model E as an extreme test case because the lower value of K_0 results in a large increase in the diffuse background IC component at energies below a few GeV and also results in a bump in the combined π^0+bremsstrahlung component at $\sim$2 GeV. One would expect that these particular spectral features would give 'E' the best chance to absorb the new lower-energy IC component as well some of the GCE component at $\sim$2 GeV.

- Model F is the best fit background model from Ref. [41].

- We also test a model identical to 'F' but with optical and infrared ISRF normalization factors raised by 50%. For this case, we do not allow the π^0+bremsstrahlung and IC normalizations to float separately.

In all our tests, we detect the GCE, IC, and bremsstrahlung templates with similarly high test statistics as when the Fermi Pass 7 background model was used (see Fig. B.1, Tab. B.1). The spectral shapes of the GCE and IC components are similar for all cases tested. The bremsstrahlung component's spectrum displayed similar features in all background tests with the exception of model E; its spectrum in that case is a power law with no cutoff.

An additional concern could be that the IC excess flux is very small compared to the flux of the expected IC background contained within the galactic diffuse model. If that were the case, then the IC excess might simply be attributable to uncertainties in the background IC modelling. To check whether this is a relevant concern, we plot in Fig. B.2 the IC, GCE, and bremsstrahlung excess component data points from Fig. 2 of the main body of this paper
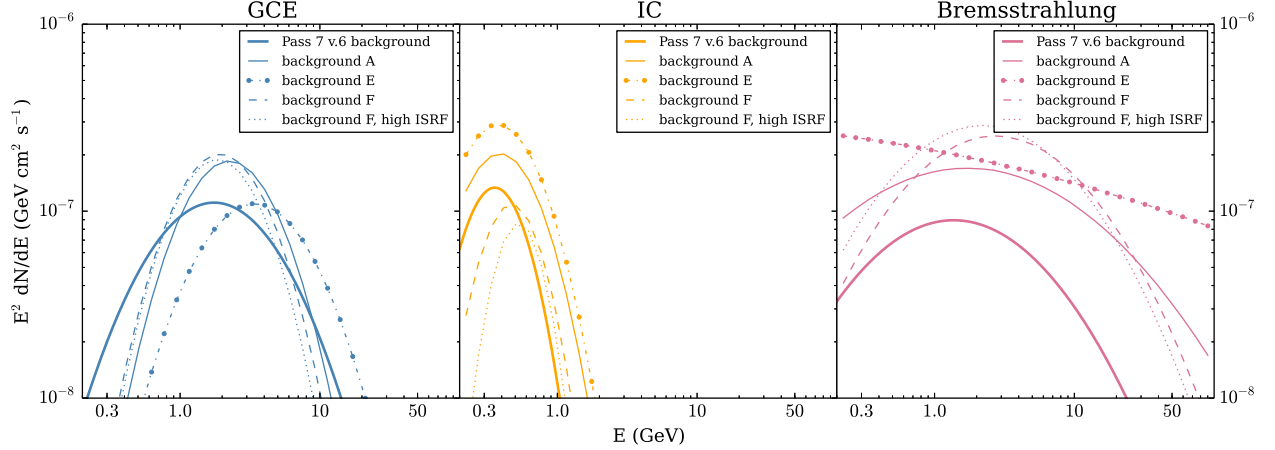
94

Figure B.1: Best-fit parameterized log-parabola model spectra for the GCE, IC, and bremsstrahlung components for tests with varying diffuse background models. $E^2 dN/dE$ is plotted for fluxes *within* the $7° \times 7°$ ROI. `ULTRACLEAN` photons were used for all analyses shown.

alongside the `GALPROP` predictions for the background π^0, bremsstrahlung, and IC emission in model F. We show the seperated components of background model F instead of the Pass 7 diffuse model in Fig. B.2 because the latter is not generated using `GALPROP` making it difficult to extract the individual π^0 and bremsstrahlung components for comparison.

From Fig. B.2 it is evident that the IC excess is not a small fraction of the background IC component, but is of the same order of magnitude at its peak. Under similar inspection, the excess bremsstrahlung and GCE normalizations are of the same order as the `GALPROP` predicted bremsstrahlung background, while being $\sim$2–3 times lower than the π^0 background at their respective peaks. In terms of both spatial and spectral morphology, the three GCE, bremsstrahlung, and IC components differ sufficiently from the diffuse background model such that they can be disentangled through the template likelihood analysis. We conclude that it is unlikely that the IC, GCE and bremsstrahlung excesses might be absorbed within the background model uncertainties.

As the HESS collaboration's Galactic Ridge residuals at TeV energies have also been found to be well-correlated with the morphology at GeV energies [121], we also replaced the 20 cm

95

| | Test statistic values for extended sources | | |
Background model	IC	GCE	Bremsstrahlung
Pass 7	197	207	97
Model A	386	388	807
Model E	336	190	1562
Model F	123	277	1707
Model F, high ISRF	102	242	2992

Table B.1:   Test statistic values for the IC, GCE, and bremsstrahlung extended sources in each of the diffuse background model tests. The bremsstrahlung template TS values are much higher in the four GALPROP-generated background cases than when the Pass 7 background was used. This may be due to the fact that the Pass 7 model constructs the π^0+bremsstrahlung component by fitting to gamma-ray data in concentric regions (as opposed to using output maps from GALPROP), which might lead to the absorption of some of the excess bremsstrahlung into the background fit.

map with a template based on the HESS residuals [19]. We recover a spectrum for the HESS template with similar normalization to the 20 cm template spectrum but with a slightly lower energy cutoff. The IC and GCE components' spectra remain consistent with results obtained with the 20 cm template (Fig. B.3).

The ND component was introduced in Ref. [7] on the GeV galactic center excess as part of a series of checks on how variations in modeling the data might affect the derived properties of the GCE. As the ND component was best fit with a spectrum essentially the same as that of the MG template, we interpreted this finding as the ND template tracing molecular gas that had not been captured by the galactic diffuse model and which lay outside the bounds of the MG template. The fact that the best fit ND spatial template is radially *increasing* is also reassuring as it allows for the ND to 'fill in' for molecular gas not included in either the MG or Pass 7 model templates, while avoiding overproducing model photons in the very central regions.

Ref. [7] also found that the Fermi isotropic background template in the $7° \times 7°$ had too soft of
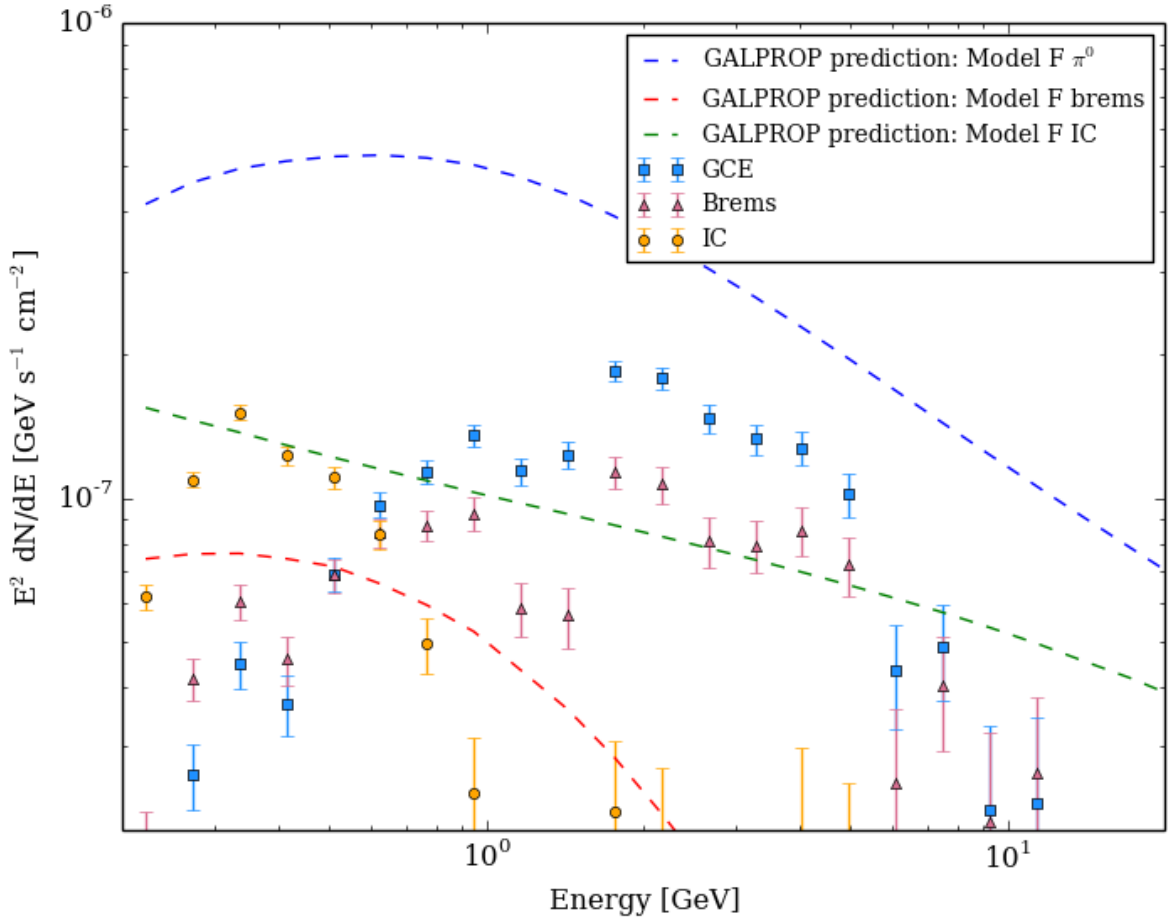
Figure B.2: The three diffuse background model components (π^0/bremsstrahlung/IC) plotted along with the residual spectra for the GCE/IC/bremsstrahlung spectra from the main body of the paper. This plot shows that the excesses are comparable to the relevant backgrounds at their peak energies.

a spectrum and too low of normalization to adequately describe the isotropic component in the region. To account for this, a 'new isotropic' source was included in the analysis (referred to as I in Ref [7]) which was best fit with a hard spectrum dN/dE$\sim E^{-2}$ and detected at high significance. To account for degeneracies between thet new isotropic source I and the Fermi isotropic background, the normalization of the Fermi isotropic source was fixed to unity in Ref. [7]. If the source I was not included in the fit, this excess of isotropic (within the ROI) hard photons was absorbed into the Fermi isotropic background by increasing its overall normalization, with other source components remaining roughly unchanged. This
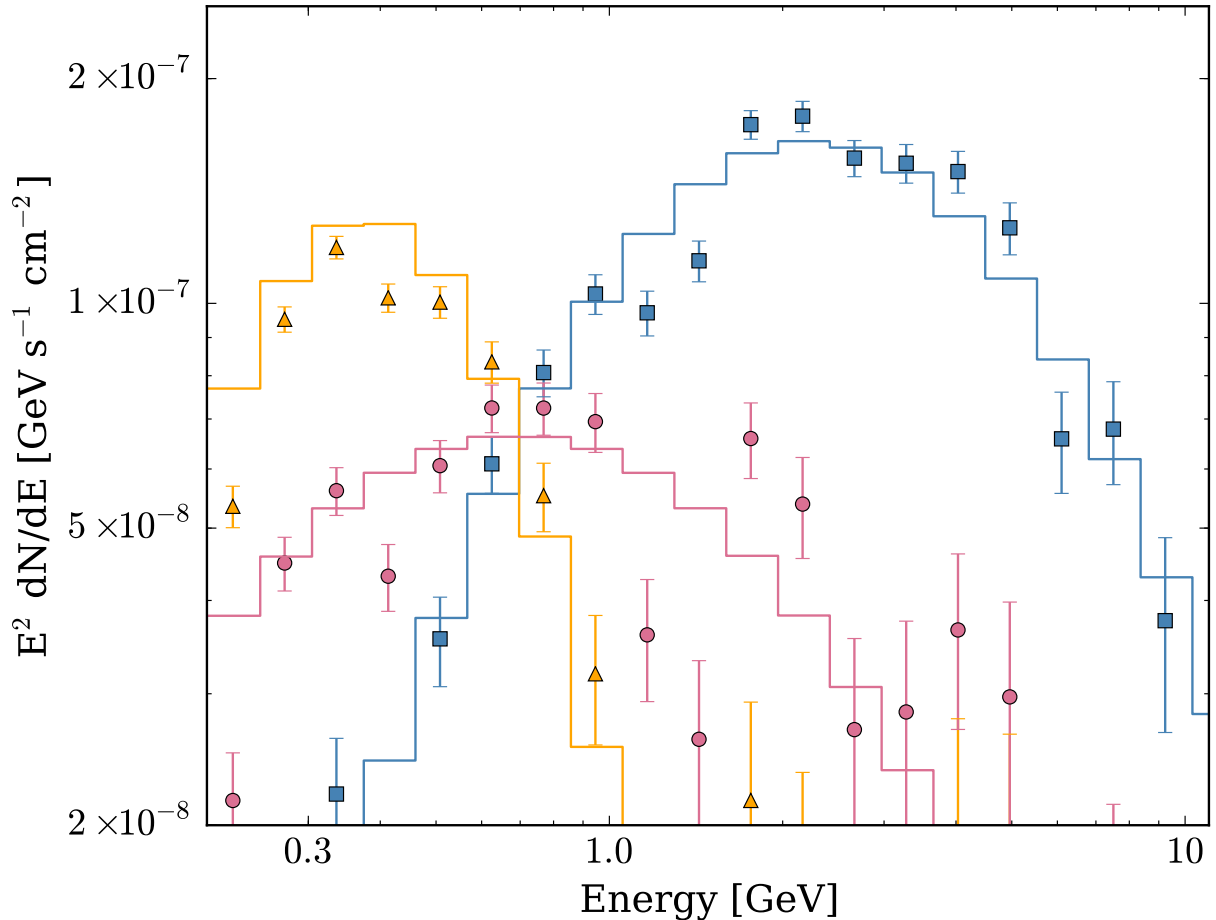
Figure B.3: Same as Fig. 3.2 but with the HESS residual map substituted in place of the 20 cm radio map for use as the bremsstrahlung template. Note the lower energy cutoff in the HESS template spectrum (pink circle).

paper does not include the hard isotropic component I. Our best fit for the ND component is spectrally harder (close to dN/dE$\sim E^{-2}$) and has a shallower spatial profile ($\sim \theta^{0.3}$ as opposed to $\sim \theta^{0.5}$) than that found in Ref. [7]. We thus interpret the ND here as a component which can absorb any isotropic or very smoothly distributed photons which are not accounted for in other parts of the model; in this paper these consist of (1) an isotropic component with a harder spectrum and higher amplitude than the standard Fermi template and (2) smoothly distributed gas which lies outside the boundary of the 20 cm template and is not picked up by the galactic diffuse model. If we include a hard isotropic component

in lieu of the ND template, our main results for the IC, brems, and GCE components still stand.

Because of our interpretation of the ND component as an extension of the MG template, we perform a fit excluding both ND and MG templates from the full model and verify that our results for the IC and GCE spectra remain consistent with the analysis in the body of the paper. The GCE and IC spectral shapes and normalizations are shown in Fig. B.4; the two cases including and excluding the MG and ND components have have best fit spectra consistent within the background model dependent variance demonstrated in Fig. B.1.
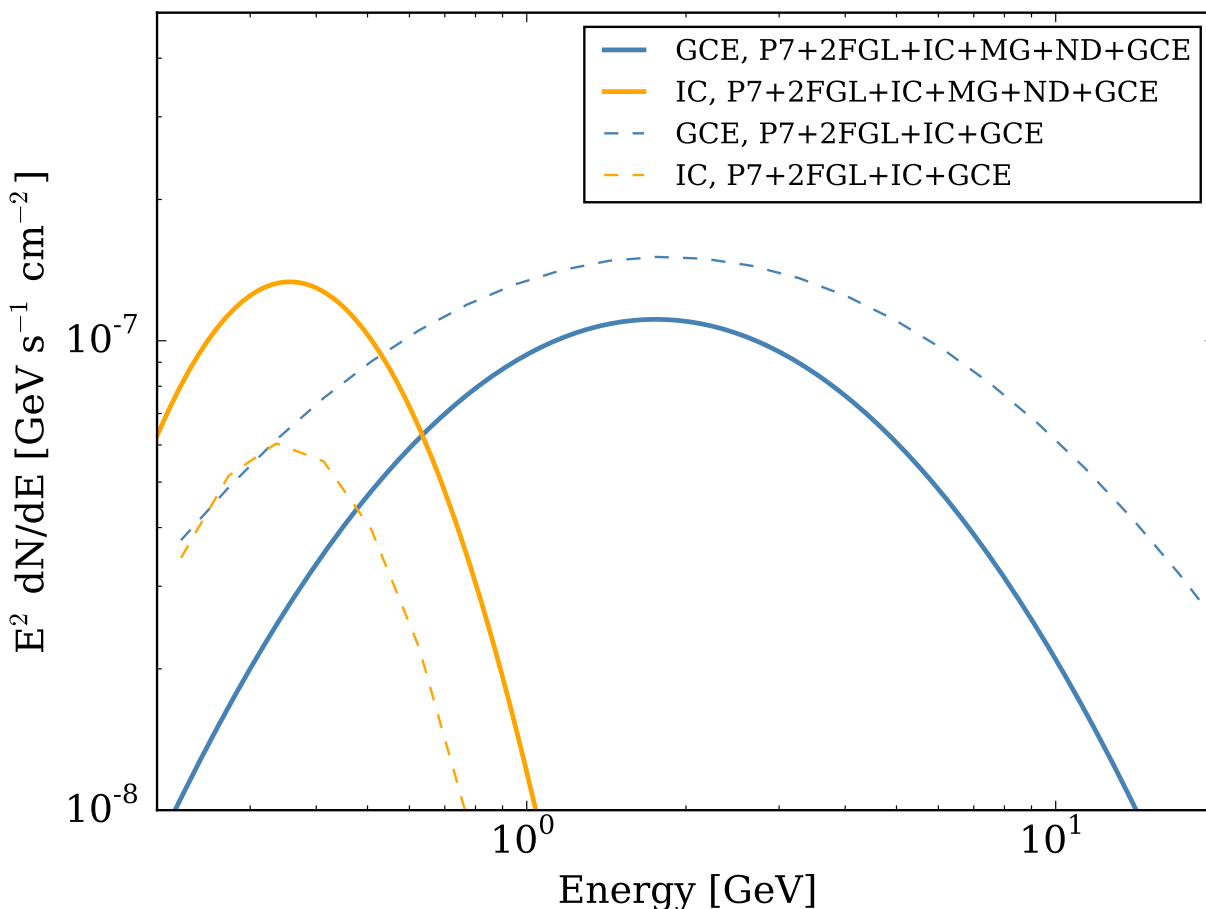

Figure B.4: Spectra for the IC (orange) and GCE (blue) components, for cases with full model as described in the paper (P7+2FGL+IC+MG+ND+GCE, solid lines) and with the full model minus the MG and ND components (P7+2FGL+IC+GCE, dashed line).